



Title	Development of / Transformable FeCrAl Oxide Dispersion Strengthened Alloys by Cobalt and Nickel Addition
Author(s)	張, 聖華
Citation	北海道大学. 博士(工学) 甲第14227号
Issue Date	2020-09-25
DOI	10.14943/doctoral.k14227
Doc URL	http://hdl.handle.net/2115/82721
Type	theses (doctoral)
File Information	Shenghua_Zhang.pdf



[Instructions for use](#)

**Development of γ/α Transformable FeCrAl Oxide Dispersion
Strengthened Alloys by Cobalt and Nickel Addition**

**A Dissertation Submitted to Hokkaido university for the Degree
of Doctor of Philosophy**

Shenghua Zhang

Division of Materials Science and Engineering
Graduate School of Engineering
Hokkaido University
September 2020

Acknowledgements

Firstly, I would like to express my deep gratitude to Dr. Shigeharu Ukai and Dr. Shigenari Hayashi, my research supervisors, for giving me the opportunity to study at Hokkaido University. I greatly appreciate their patient guidance, enthusiastic encouragement and constructive recommendations on my research work. I would like to offer my special thanks to Dr. Seiji Miura and Dr. Naoyuki Hashimoto, who reviewed my dissertation and provided me many useful critiques.

Secondly, I would like to extend my appreciation to Dr. Naoko H. Oono, for her advice and assistance in operation of TEM and FIB. I would also like to thank the entire members of my laboratory for helping me embrace the new environment and getting familiar with all facilities in such a short time. I am particularly grateful for the assistance given by Dr. S.M.S. Aghamiri, Dr. Hao Yu, Dr. Yenlin Kuo, Mr. Tomonori Nishikawa, Mr. Chenlong Zhou, Mr. Shoki Kasai, Mr. Takashi Sowa, Mr. Kenta Umehara, Ms. Azusa Konno and Ms. Mai Yamashita.

Thirdly, I would like to extend my thanks to the “Joint-use Facilities: Laboratory of Nano-Micro Material Analysis” of Hokkaido University for the supply and operation of analysis equipments, particularly, Mr. Nobuyuki Miyazaki and Mr. Endo Takashi for EPMA and FIB, Ms. Yurika Yamanouchi for XRD, and Dr. Yongming Wang for TEM. I also wish to acknowledge the China Scholarship Council (CSC) for the provision of a scholarship during my PhD period.

Finally, I am extremely grateful to my family for their support, especially my girlfriend. I would also like to thank my friends and everybody who helped me during my PhD study at Hokkaido University.

Table of contents

CHAPTER 1 Introduction.....	3
1.1 Materials for high temperature applications	3
1.2 Development of FeCrAl alloys and ODS alloys	4
1.3 Objective and strategy.....	5
1.4 Outline.....	6
CHAPTER 2 Fundamental aspects	8
2.1 Dispersion strengthening by oxide particles	8
2.2 Order strengthening by B2 phase.....	9
2.3 High temperature oxidation	10
2.3.1 General aspect.....	10
2.3.2 Microstructural effects	11
2.3.3 Reactive element effects	12
2.4 Characterization of dislocations.....	13
2.4.1 Contrast from a single dislocation	13
2.4.2 Two-beam conditions	14
CHAPTER 3 Characterization of FeCrAl-ODS Alloys by Cobalt Addition	22
3.1 Introduction.....	22
3.2 Alloy design	22
3.3 Experimental methods	23
3.4 Results.....	23
3.4.1 Phase diagram and microstructure characterization	23
3.4.2 Oxide particle and B2-type CoAl phase characterization.....	24
3.5 Discussion	26
3.6 Conclusion	27
CHAPTER 4 Oxidation behavior of Co-added alloys	39
4.1 Introduction.....	39
4.2 Experimental method	40
4.3 Results of oxidation test at 1000 °C.....	41
4.3.1 Oxidation kinetics	41
4.3.2 Phase composition and morphology of oxide scales	41
4.3.3 Chemical composition and microstructure of oxide scales.....	42
4.3.4 Segregation of reactive element.....	43
4.4 Results of oxidation test at 800 °C and 900 °C.....	44
4.4.1 Oxidation kinetics	44
4.4.2 Phase composition and morphology of oxide scales	44

4.4.3 Chemical composition and microstructure of oxide scales.....	45
4.5 Discussion	46
4.5.1 Internal oxidation and external scale formation at 1000 °C	46
4.5.2 Effect of cobalt addition on reactive element effect at 1000 °C	47
4.5.3 Influence of cobalt addition on solute Y concentration	48
4.5.4 Effect of cobalt addition on oxidation rate at 800 °C and 900 °C	49
4.6 Conclusion	50
CHAPTER 5 Tensile properties of Co-added FeCrAl ODS alloy	69
5.1 Introduction.....	69
5.2 Experimental method	69
5.3 Results	70
5.3.1 Distribution of CoAl precipitates and oxide particles.....	70
5.3.2 Structure of CoAl precipitates and ferrite matrix	71
5.3.3 Tensile properties	72
5.3.4 Anisotropic properties	72
5.4 Discussion	73
5.4.1 Oxide particle strengthening and B2-type order strengthening	73
5.4.2 B2-type order strengthening at 500 °C	76
5.4.3 Superposition consideration.....	77
5.5 Conclusion	78
CHAPTER 6 Development of FeCrAl-ODS alloys by nickel addition.....	87
6.1 Introduction.....	87
6.2 Alloying design and computed phase diagram	88
6.3 Experimental procedure	89
6.4 Results and discussion	90
6.4.1 Stable α/γ phases at high and room temperatures	90
6.4.2 γ/α phase transformation during cooling	92
6.4.3 Oxidation resistance.....	93
6.5 Conclusion	95
CHAPTER 7 Conclusions.....	108
References.....	111

CHAPTER 1 Introduction

1.1 Materials for high temperature applications

The need for materials with high temperature capability in industries such as electric power generation, transportation and materials production processing has increased dramatically since the early 1900s. Generally speaking, process efficiency increases with the operating temperature and sufficient mechanical properties but early attempts to improve efficiency by raising temperatures were not always successful. Many industries are extensively and intensively engaged in the development of new and better materials. Their efforts are crucial to innovations which will render the companies more energy efficient and more capable of meeting international competition in the future. From the mid-1900s accelerating effort has been directed towards increasing the temperature capability of existing material systems and developing new type materials. Currently many materials in high temperature service are working at the limit of their capability. The demand for not only corrosion resistance but also strength and toughness means that materials must now be designed for very specific application needs.

Ferrous alloys with chromium addition are widely used in the high temperature environments because of low cost, high production and also high temperature capability due to excellent strength and corrosion resistance. However, once temperatures in the region of 900 °C are required the oxidation rate and strength combination of these alloys becomes critical. At higher temperatures, nickel and cobalt based alloys, “superalloys”, are required [1,2]. They have been developed primarily for gas turbine applications. These alloys exhibit higher strength at higher temperatures than ferrous alloys, which is achieved by reducing chromium content. The lower chromium content is necessary to guarantee microstructural stability. Additions of alloying elements such as Nb, Ti and Al are required for optimal creep properties [3]. However, as strengthening alloying elements content increases the alloys have to be cast instead of wrought [4]. Refractory metals, possess attractive high temperature strength but are handicapped by their very poor oxidation resistance, mainly due to volatile or molten oxides. Monolithic ceramics and particularly silicon nitride (Si_3N_4) and silicon carbide (SiC) show potential for application as high

temperature structural materials [5]. They are stronger than the nickel superalloys above 1000 °C, and have superior creep strength and oxidation resistance and are potentially cheaper. In addition their density is less than half that of the superalloys (typically 3.2 gm/cms compared to 7.9 gm/cms). The critical shortage of these materials, however, is their intrinsic flaw sensitivity, brittleness and consequent lack of reliability.

1.2 Development of FeCrAl alloys and ODS alloys

A class of Iron-chromium-aluminum (FeCrAl) alloys is typically deployed within industrial applications where high temperature oxidation resistance is needed. FeCrAl alloys have been primarily utilized as heating elements and components in high temperature furnaces because of their superior oxidation resistance over many other common materials. FeCrAl alloys have also been considered for structural applications for varying industrial applications over the past half a century including for the nuclear power industry. The earliest extensive effort within the nuclear industry was completed as part of the High-Temperature Materials and Reactor Component Development Program which is documented in a series of publicly available reports published by General Electric (GE) Corporation [6–14]. The large-scale program was focused on developing fuel elements for elevated temperature nuclear applications which included coolants of steam, air, and carbon-dioxide. A series of different FeCrAl alloys with varying Cr content (typically 5-15 wt.%) and Al content (typically 3-6 wt.%) were developed and evaluated. Evaluations included fuel-clad compatibility, high-temperature exposure in air and steam, aging, welding/formability, and radiation effects, among several other topics. Processing routes included wrought and powder metallurgy techniques with final form factors of both plate and tube. Most alloys were simple systems with only Fe, Cr, Al, and Y used to form the alloy; these alloys are deemed “GE model” alloys herein.

Publicly available program reports on the GE model alloys exist into the late 1960s, although some studies were present later including the swelling study nearly a decade later by Little and Stow [15]. Limited details on the extinction of FeCrAl alloys within the program are given but indications are that the lack of high-temperature mechanical properties [16] and lower temperature embrittlement [17]

were significant reasons for not considering further pursuit past the last available report of the program [9].

Forty years later, since the severe accident of Fukushima Daiichi nuclear power plant on March 11, 2011, the development of oxidation-resistant alloys for accident-tolerant fuel (ATF) cladding has been focused worldwide. Development of nuclear grade, iron-based wrought FeCrAl alloys has been initiated for LWR fuel cladding to serve as a substitute for Zr-based alloys with enhanced accident tolerance. Significant efforts on developing FeCrAl alloys have been conducted by commercial entities, national laboratories, and university, many times with significant cross collaborations between the different research sectors. In the United States, FeCrAl alloys have been studied [18-23] because Al-containing alloys produce stable alumina (Al_2O_3) scale, preventing direct reaction of Fe with steam. In Japan, FeCrAl oxide dispersion strengthened (ODS) alloys with improved high-temperature strength contributed by nano-sized oxide particles have been developed for additional radiation tolerance [23, 24] based on the previous research and development of 9Cr-ODS [25-27], 12Cr-ODS [28-30], and high Cr-ODS [31] for Generation IV fast reactors.

1.3 Objective and strategy

The standard composition of FeCrAl ODS alloys is Fe–12Cr–6Al–0.4Zr–0.5Ti–0.24Ex.O–0.5Y₂O₃ (wt.%), where Ex.O (excess oxygen) means the total oxygen minus oxygen coupled with yttrium as Y₂O₃. This alloy contains a large amount of the ferrite former elements Cr and Al to improve the corrosion and oxidation resistance. This alloy design results in a full ferrite structure until melting. The grain morphology and hardness of FeCrAl ODS alloys can thus be controlled only by recovery and recrystallization during the intermediate heat treatment in cladding manufacturing by pilger mill rolling. However, the recrystallization process is not reliable because the same recrystallized structure could not be potentially repeated and it depends on the cold rolling reduction rate, temperature, structural texture, and so on [32, 33]. In contrast, with the development of transformable FeCrAl ODS alloys, the grain morphology and hardness can be controlled by α/γ phase transformation more easily and precisely during the intermediate heat treatment [34]. Therefore, transformable FeCrAl ODS alloys by introducing the austenite stabilizing elements Co and Ni are

needed to develop for controlling the microstructure of FeCrAl ODS alloys.

The objective of this study is to develop phase transformable FeCrAl ODS alloys which possess good oxidation resistance at high temperature and sufficient mechanical properties. The grain morphology and hardness control using phase transformation will make the manufacture process easier. The equiaxial grains obtained using phase transformation will modify the anisotropic properties of FeCrAl ODS alloys. The formation of protective Al_2O_3 scale is expected on the surface of Co/Ni-added FeCrAl ODS alloys with appropriate Cr and Al contents. The strengthening effect of oxide particles and B2 type order phase will guarantee the mechanical properties.

So far, almost no research on the development of transformable FeCrAl ODS alloys by introducing austenite stabilizing elements has been conducted. Therefore, the findings of the present work are expected to modify the developed FeCrAl ODS alloys and provide new insights into developing desirable materials for various applications, especially at high temperatures.

1.4 Outline

In chapter 1, the materials for high temperature applications and the development of FeCrAl alloys were introduced. Moreover, the background and aims of this study were illustrated.

In chapter 2, theoretical background and technical methods utilized in this study were introduced.

In chapter 3, the microstructure of Co-added alloys was characterized, three phases were identified: matrix with bcc structure, chromium carbide, and dispersed CoAl intermetallic compound. Nanosized oxide particles were also characterized by transmission electron microscopy. The 3Al alloys with 15 and 25 wt.% Co and 5Al alloy with 25 wt.% Co demonstrated α to γ transformation at 1000 °C, whilst α -phase remained in the 5Al-alloy with 15 wt.% Co. Suppression of α to γ transformation in specimen 5Al15Co was successfully explained by the pinning of α/γ interfaces by oxide particles. Continuous cooling transformation curves constructed by in-situ high temperature X-ray diffraction showed that microstructure control using the γ/α phase transformation is feasible.

In chapter 4, the high temperature oxidation behavior of Co-added alloys was studied at 800 °C, 900 °C and 1000 °C in air. Exclusive α -Al₂O₃ scales were formed on the surfaces of 5Al alloys at the temperature range from 800 °C to 1000 °C. The discontinuous aluminum oxide in the internal oxidation zone of austenitic 3Al alloys oxidized at 1000 °C was found. Y segregation at the grain boundaries was confirmed and the Co addition caused the outer layer thickness and the grain size of alumina increase in 5Al alloys oxidized at 1000 °C. The decrease of oxidation kinetics of Co-added 5Al alloys was attributed to the increase of the lateral grain size. On the other hand, protective α -Al₂O₃ scales were also formed on the surfaces of 3Al alloys at the temperature range from 800 °C to 900 °C except for the dual phase 3Al15Co alloy oxidized at 900 °C. The Co addition was detrimental to the oxidation kinetics when 3Al alloys were oxidized at 800 °C and 900 °C.

In chapter 5, the tensile properties of Fe12Cr5Al25Co ODS alloy were evaluated, focusing on the oxide dispersion strengthening and B2-type CoAl ordered strengthening at both ambient and elevated temperatures. The oxide particles and B2-type CoAl precipitate were characterized and strengthening mechanisms for the oxide particles and CoAl-precipitate were evaluated by hardness and tensile tests at room temperature, 300 °C, and 500 °C. The calculated values showed good agreement with the experimental results at RT and 300 °C. However, the order strengthening by CoAl precipitates was significantly reduced at 500 °C, which is attributed to the increase of thermally activated $\langle 001 \rangle$ slip in the body-centered cubic matrix.

In chapter 6, characterization and high temperature oxidation test of Ni-added alloys were introduced. Combination of the high Al and low Ni leads to stabilization of the α -ferrite at 1000 °C. In contrast, low Al and high Ni provides γ -austenite at room temperature. The Fe12Cr5Al12Ni ODS alloy and Fe12Cr7Al22Ni ODS alloy are preferable for γ to α phase transformation during cooling. A_{C1} and A_{C3} temperatures and critical cooling rate for the martensite transformation were also clarified. The oxidation test at 1000 °C in air revealed that 7 wt.% Al is sufficient to form protective Al₂O₃ scale. Even at 5 wt.% Al, the reduced Ni-content induces superior oxidation resistance via Al₂O₃ formation.

In chapter 7, the main conclusions and most relevant findings of this work are presented and summarized.

CHAPTER 2 Fundamental aspects

2.1 Dispersion strengthening by oxide particles

Oxide dispersion strengthening is based on a mechanism that artificially added chemically stable oxide particles are incoherent within the lattice of materials. Generally, these particles are fine and uniformly distributed in the matrix, and hence can decrease movement of dislocations within the material and in turn enhance strength and prevent creep. In addition, they are capable of pinning the grain boundaries to prevent the growth of grains. Therefore, the mechanical properties of alloys are enhanced. Since these secondary phase particles have high melting points and low diffusion rate, their strengthening effect can last to higher temperature. The application temperature of dispersion materials could be up to $0.8\sim 0.9T_m$ [35].

Generally, ODS alloys show following characteristics: (1) A high service temperature. Comparing with conventional alloys, whose strength is maintained to the temperature of $0.7 T_m$ (T_m : melting point), the ODS alloys can reach to the $0.857 T_m$ and result in the improving of service temperature by 100-200 °C; (2) A high yield strength, which is close to the ultimate tensile strength; (3) Superior creep properties at elevated temperature. The microstructure shows high stability even after a long-term service at high temperature, which is attributed to the pinning effect of the secondary phase particles [36].

Y_2O_3 has been primarily adopted as the oxide particles for the fabrication of ODS alloys in the world, because it almost meets all the requirements and without radioactivity [37]. The number density of the particles shows a close relationship with the mechanical properties, i.e., a high volume fraction of the particles could enhance the strength but decrease the plasticity. Therefore the content of the secondary dispersoid is usually controlled in the range of 0.5-2.0(wt. %). Moreover, at a given concentration of oxide particles, the dispersed particle size and the average distance between two particles are other two important factors, which should less than 0.05 μm and 0.1 μm , respectively.

For oxide particles such as Y_2O_3 , they are very strong impenetrable precipitates; therefore the dislocation has to bypass the obstacle. The **Fig. 2.1** schematically illustrates the Orowan mechanism, as shown below [38]. At the first step, the

dislocation bows out between two particles. Then yielding occurs when the bowed-out dislocation becomes semi-circular in shape. After the yielding, the dislocation leaves Orowan loops around the particles. The formation of the Orowan loops makes the dislocation motion more and more difficult.

The dislocation line is pinned behind the obstacles and bows out between them as shown in **Fig. 2.2**. In the figure, F is the pinning force that the obstacle can sustain and φ is the bending angle. T is the line tension of the dislocation. The force balance becomes:

$$F = 2T \cos \varphi \quad (2.1)$$

The bowing of dislocation is under the influence of shear stress τ , which acts to maintain the curvature, while the line tension tends to straighten the line. Therefore, the balance can also be described as [39]:

$$F = \tau b \lambda \quad (2.2)$$

in which, λ is the distance between two particles; the b is Burgers vector.

For strong and impenetrable oxide particles, the force F reaches to maximum F_{\max} when $\varphi = 0$ and shear stress τ was defined to be critical shear stress under the circumstance. Then the equations become:

$$F_{\max} = 2T = \tau_c b \lambda \quad (2.3)$$

$$\tau_o = \frac{2T}{b\lambda} \quad (2.4)$$

For the line tension T , the following formula can be used

$$T = \frac{Gb^2}{4\pi(1-\nu)} (\ln \bar{D} + B) \quad (2.5)$$

where G is shear modulus, ν is Poisson's ratio, \bar{D} is harmonic mean of λ and the diameter of obstacle, and B is a constant taken as 0.65.

Substituting T in Eq. (2.4), the strengthening of dispersed oxide particles σ_o becomes:

$$\sigma_o = M \times \tau_o = \frac{M G b}{2\pi\lambda(1-\nu)} (\ln \bar{D} + B) \quad (2.6)$$

2.2 Order strengthening by B2 phase

Order strengthening mechanism is similar to the Orowan mechanism. Comparing with the impenetrable oxide particles, the ordered precipitates usually are weaker. **Fig. 2.3** [40] shows that the dislocation can partially or completely penetrate the

precipitates. When a dislocation shears an ordered precipitate, an antiphase boundary (APB) may be created with a specific APB energy γ_{APB} . This energy per unit slip plane is equal to the force per unit length opposing the motion of the dislocation entering the precipitate. Therefore, in the simplest analysis this force is equal to:

$$F_{max} = 2\gamma_{APB}r \quad (2.7)$$

in which r is the radius of precipitate. Considering the effective obstacle spacing, Eq. (2.3) can be changed into:

$$F_{max} = 2T \cos \varphi_c = \tau_c b \frac{l_s}{\cos \varphi_c} \quad (2.8)$$

Where φ_c is critical bending angle; l_s is center to center distance between two obstacles and it is related to the precipitate radius r and volume fraction of precipitate f :

$$l_s = \left(\frac{32}{3\pi f} \right)^{1/2} r \quad (2.9)$$

Combining Eq. (2.7) and Eq. (2.8), utilizing Eq. (2.9), the critical shear stress can be expressed:

$$\tau_c = \frac{\gamma_{APB}}{b} \left(\frac{3\pi^2 \gamma_{APB} f r}{32T} \right)^{1/2} \quad (2.10)$$

Dislocations in a material with ordered precipitates are often found to travel in pairs, the second dislocation removing the disorder left behind by the first. If order hardening is a dominant strengthening mechanism, the resistance experienced by the second dislocation when shearing a precipitate can be very low, resulting in a straight dislocation line, as depicted in **Fig. 2.3**. To calculate the total effect of both dislocations, Eq. (2.10) can be modified into:

$$\tau_c = \frac{\gamma_{APB}}{2b} \left[\left(\frac{3\pi^2 \gamma_{APB} f r}{32T} \right)^{1/2} - f \right] \quad (2.11)$$

2.3 High temperature oxidation

2.3.1 General aspect

At high temperatures, most metals will inevitably oxidize over a wide range of conditions. The practical issues of material lifetimes and corrosion protection methods therefore centre around the rate of oxidation, and how to control reaction morphology. Answers to the second question turn out to be rather interesting and involve the need

for a fundamental understanding of the processes involved and ways to modify them [41].

Regarding metals, high temperature oxidation refers to the reaction of the alloys with oxygen from the surrounding air to form an oxide scale on the surface. The metal surfaces oxidize rapidly and produce an oxide layer, which may decelerate further oxidation depending on the density, porosity, chemical composition and adherence of oxide scale. Thus the establishment and maintenance of an alumina scale is essential for successful performance. In general, high temperature oxidation of a metal is controlled by both thermodynamic and kinetic factors.

2.3.2 Microstructural effects

Generally the oxide scale is assumed to be continuous, coherent, perfectly bonded to the substrate metal and capable of diffusion only via lattice defects. These assumptions can be successful, particularly at high temperatures in systems containing large concentrations of lattice defects. At lower temperatures and in oxides with less defective lattices, the assumptions are failed. For slow growing oxides like Cr_2O_3 and Al_2O_3 , these oxides have immeasurably small deviations from stoichiometry, and their diffusion properties are not well understood. These difficulties result from the nature of the oxides. Firstly, the native lattice defect concentrations are so small that even low concentrations of impurities can dominate the oxide. Secondly, and for the same reason, diffusion via pathways other than the oxide lattice are usually important. That mechanism has been shown to be grain boundary diffusion.

Oxide scales are polycrystalline, and grain size can vary considerably. **Fig. 2.4** [42] shows that the NiO grain size in a scale grown at 1100 °C is tens of microns. In oxide grown at 800 °C, the columnar grains seen in **Fig. 2.5** [42] are about 1 µm across. At lower temperatures, the grains are even finer and show evidence of coarsening with time (**Fig. 2.6** [43]).

Grain boundary diffusion is often more important than lattice diffusion at low temperatures. A principal reason for this is the lower activation energy of the boundary process, corresponding to the more disordered structures in the boundaries [44]. A second reason is the usually finer grain size and hence more numerous boundaries encountered at lower temperatures, as illustrated in **Fig. 2.5**. A useful way

of describing diffusion in a polycrystalline material was proposed by Hart [45] and adapted by Smeltzer et al. [46] to the nickel oxidation case. An effective diffusion coefficient D_{eff} is defined as a weighted sum of lattice and boundary contributions

$$D_{\text{eff}} = D_L(1 - f) + D_B f \quad (2.12)$$

where f is the fraction of diffusion sites within the boundaries, and D_L , D_B are the self-diffusion coefficients for the lattice and grain boundary, respectively.

2.3.3 Reactive element effects

An application of the reactive element effect (the addition of Ce to a Ni-Cr alloy) was patented by Pfeil [47] in 1937. Since then, reactive element additions have become a key part of high-temperature alloy design, supported by a very large research effort. Reactive element additions improve greatly the ability of chromia and alumina forming alloys to resist scale spallation. Understanding this phenomenon has been made difficult by the multiplicity of effects reactive elements have on alloy-scale systems. The most obvious of these are the changes in scaling rate and mass transfer mechanisms.

Tracer diffusion studies with $^{18}\text{O}_2$ [48, 49, 50-52] showed that the transport mechanism of alumina-forming alloys with reactive elements addition was changed from mixed oxygen and aluminum transport to principally oxygen transport.

A series of scanning transmission electron microscopy studies has made clear that reactive elements segregate to oxide grain boundaries and have also been found at the scale-alloy interface [53]. The enrichment of reactive elements at oxide grain boundaries alters their transport properties.

Oxide microstructures are altered by the presence of reactive elements. Alumina scales are changed by reactive elements from coarse and equiaxed to fine and columnar [54-56]. The oxide-alloy interface is also altered by the presence of reactive elements. Reactive elements have a strong affinity for sulphur as well as oxygen. They are therefore able to desulphurise the alloy, forming sulphide or oxysulphide particles and preventing sulphur contamination at the scale-alloy interface. An alternative possibility is the preferential segregation of sulphur to surfaces of internal reactive element oxide particles. Sulphur segregation to this interface is found to be suppressed [55-58], wrinkling and scale detachment is decreased [54, 59, 60], oxide

intrusions or ‘pegs’ in some cases grow into the alloy [45] and the interface is strengthened [61] in the case of a desulphurised alloy.

The various reactive elements differ in effectiveness in different alloy systems. An important factor is the limited solubility of these elements, which varies with both the identity of the additive and the nature of the solvent alloy. Excessive additions can lead to the precipitation of intermetallic phases which are susceptible to internal oxidation.

2.4 Characterization of dislocations

2.4.1 Contrast from a single dislocation

For the study on dislocations, It is important know how many dislocations (the density) and whether they are edge, screw, or mixed in character. The displacement field in an isotropic solid for the general, or mixed, case can be written as [62]

$$\mathbf{R} = \frac{1}{2\pi} \left(\mathbf{b}\phi + \frac{1}{4(1-\nu)} \{ \mathbf{b}_e + \mathbf{b} \times \mathbf{u} (2(1-2\nu) \ln r + \cos 2\phi) \} \right) \quad (2.13)$$

For convenience, \mathbf{R} is given here in polar coordinates (r and ϕ) shown in **Fig. 2.7**; \mathbf{b} is the Burgers vector, \mathbf{b}_e is the edge component of the Burgers vector, \mathbf{u} is a unit vector along the dislocation line (the line direction), and ν is Poisson’s ratio.

The amplitude of the diffracted beam, ϕ_g , is directly influenced by the value of \mathbf{R} . We can consider two particular cases, namely, the screw and edge dislocations. For the screw dislocation, $\mathbf{b}_e = 0$ and \mathbf{b} is parallel to \mathbf{u} so that $\mathbf{b} \times \mathbf{u} = 0$. Then the expression for \mathbf{R} in Eq. 2.13 simplifies to

$$\mathbf{R} = \mathbf{b} \frac{\phi}{2\pi} = \frac{b}{2\pi} \tan^{-1} \left(\frac{z-z_d}{x} \right) \quad (2.14)$$

Here, z is the distance traveled down the column and z_d is the distance of the dislocation core below the top surface (again, refer to **Fig. 2.7**). The dependence on $(z - z_d)$ emphasizes that the displacement field is present above and below the dislocation; it affects the whole column. From these two equations it is given that $\mathbf{g} \cdot \mathbf{R}$ is proportional to $\mathbf{g} \cdot \mathbf{b}$. For this reason, images of dislocations can be discussed in terms of $\mathbf{g} \cdot \mathbf{b}$ (g-dot-b) contrast. If $\mathbf{g} \cdot \mathbf{b} = 0$, then no contrast is obtained because the diffracting planes are then parallel to \mathbf{R} .

The second special case arises when the dislocation is pure edge in character.

Then $\mathbf{b} = \mathbf{b}_e$ and $\mathbf{g} \cdot \mathbf{R}$ involves two terms $\mathbf{g} \cdot \mathbf{b}$ and $\mathbf{g} \cdot \mathbf{b} \times \mathbf{u}$. (The latter term is read as ‘g-dot-b-cross-u.’) The displacement field causes the Bragg-diffracting planes associated with \mathbf{g} to bend. Incidentally, the origin of $\mathbf{g} \cdot \mathbf{b} \times \mathbf{u}$ is interesting; it arises because the glide plane is buckled by the presence of an edge dislocation as illustrated in **Fig. 2.8**. This buckling can be important because it complicates the analysis of \mathbf{b} for some dislocations with an edge component, as below.

- 1) Always remember: $\mathbf{g} \cdot \mathbf{R}$ causes the contrast and for a dislocation, \mathbf{R} changes with z .
- 2) If $\mathbf{g} \cdot \mathbf{b} = n$, and \mathbf{g} is known and n can be determined, then \mathbf{b} can be analyzed.

In experimental process, the deviation parameter s is usually set to be greater than 0 for \mathbf{g} when imaging a dislocation in two-beam conditions. Then the dislocation can appear as dark contrast against a bright background in a BF image.

2.4.2 Two-beam conditions

Bragg diffraction is controlled by the crystal structure and orientation of the specimen. Diffraction can be used to create contrast in TEM images. Crystalline specimens usually give a single-crystal DP. Diffraction contrast is simply a special form of amplitude contrast where the scattering occurs at special (Bragg) angles.

To get good strong diffraction contrast in both BF and DF images the specimen is tilted to two-beam conditions, in which only one diffracted beam is strong. Of course, the direct beam is the other strong spot in the pattern. Note that the electrons in the strongly excited hkl beam have been diffracted by a specific set of hkl planes and so the area that appears bright in the DF image is the area where the hkl planes are at the Bragg condition. Hence the DF image contains specific orientation information, not just general scattering information. The specimen can be tilted to set up several different two-beam conditions. **Fig. 2.9** includes a zone axis DP from a single-crystal specimen in which the beam direction is [011]. The surrounding patterns are a series of two-beam conditions in which the specimen has been tilted slightly so that different hkl spots are strongly excited in each pattern. We can form DF images from each strongly diffracted beam after tilting the specimen, and each will give a different image.

While looking at the DP, tilt around until only one diffracted beam is strong, as in **Fig. 2.9**. The other diffracted beams don’t disappear because of the relaxation of the

Bragg conditions, but they can be made relatively faint. To get the best contrast from defects, the specimen shouldn't be exactly at the Bragg condition ($s=0$) as in **Fig. 2.10A**. Tilt the specimen close to the Bragg condition but makes small and positive. (The excess hkl Kikuchi line, just outside the hkl spot) This will give the best possible strong-beam image contrast as in **Fig. 2.10B**. If the specimen is tilted slightly, so s increases further as shown in **Fig. 2.10C**, the defect images become narrower but the contrast is reduced.

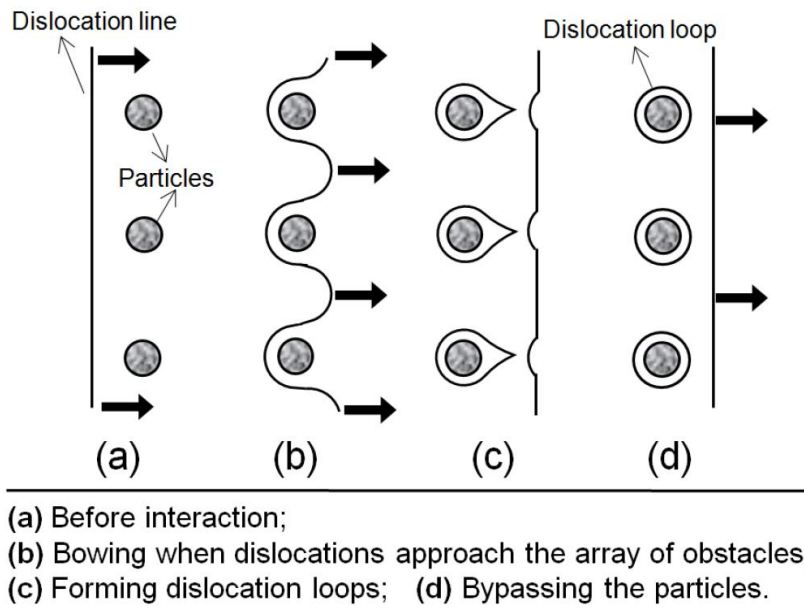


Fig. 2.1 Schematic of Orowan mechanism

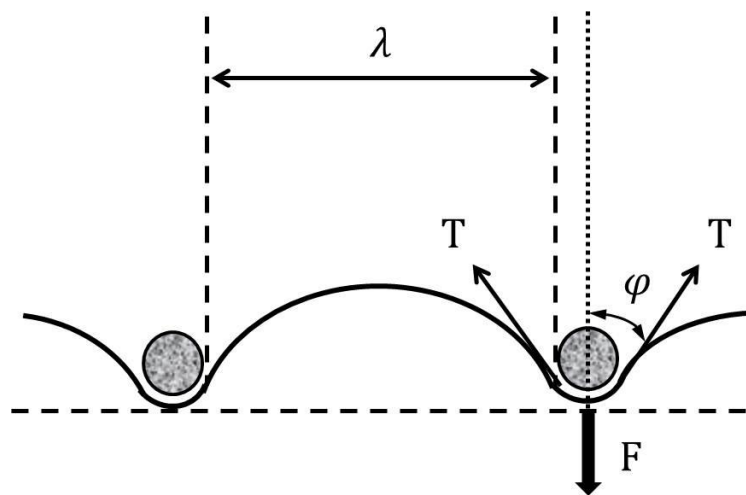


Fig. 2.2 Equilibrium model between the dislocation and particles

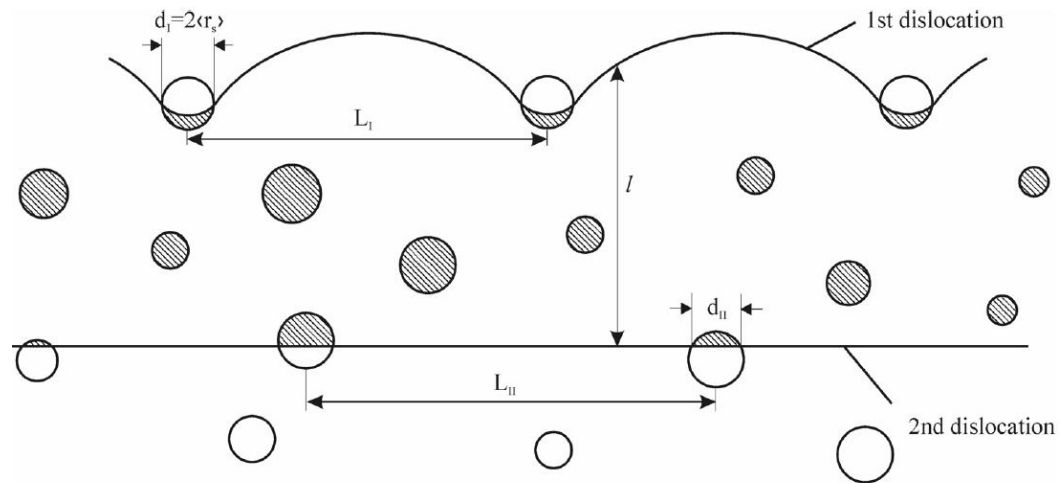


Fig. 2.3 A coupled pair of dislocation cutting through ordered precipitates. The first dislocation creates an anti-phase boundary within the precipitates. Perfect order is restored by the second dislocation. The colored precipitates contain an APB [40].

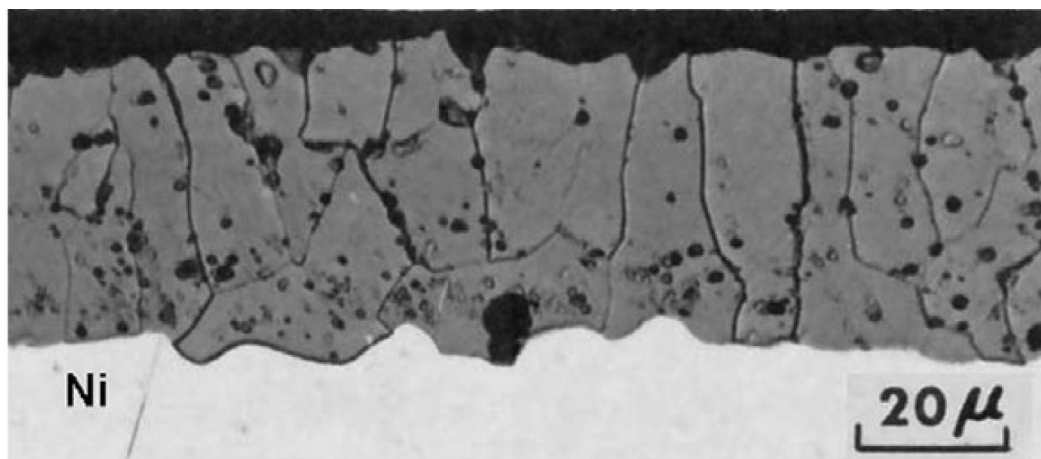


Fig.2.4 Cross-sections of oxide scales on Ni.[41]

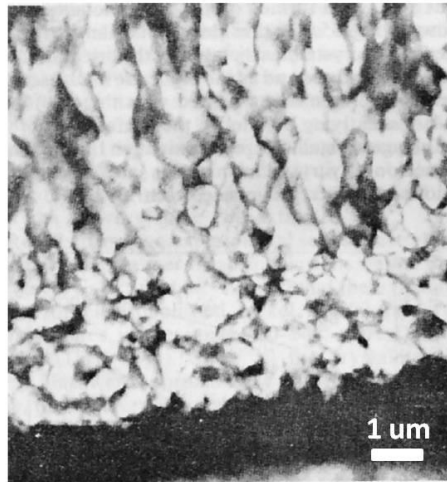


Fig.2.5 SEM view of cross-section through NiO scale. [41]

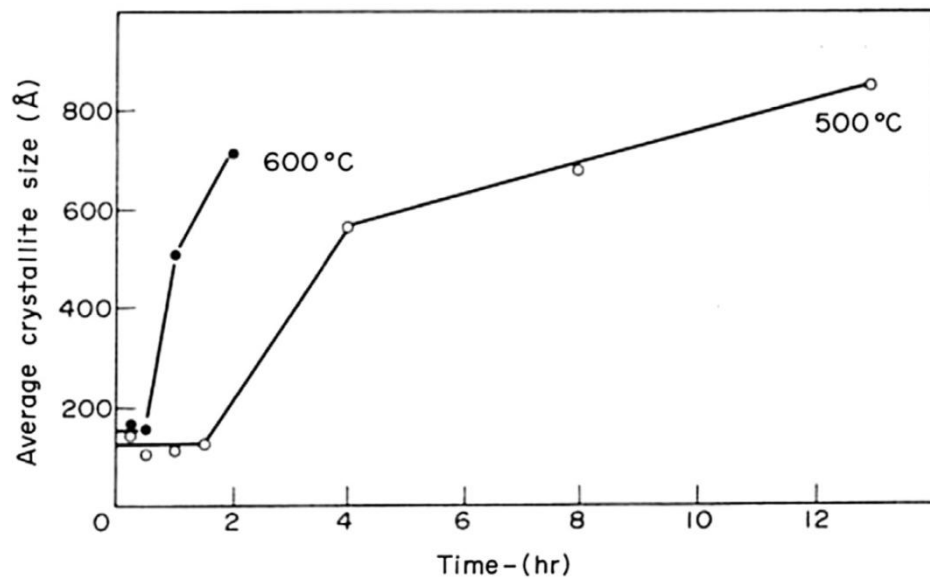


Fig.2.6 Average grain size in NiO scales as a function of oxidation time. [42]

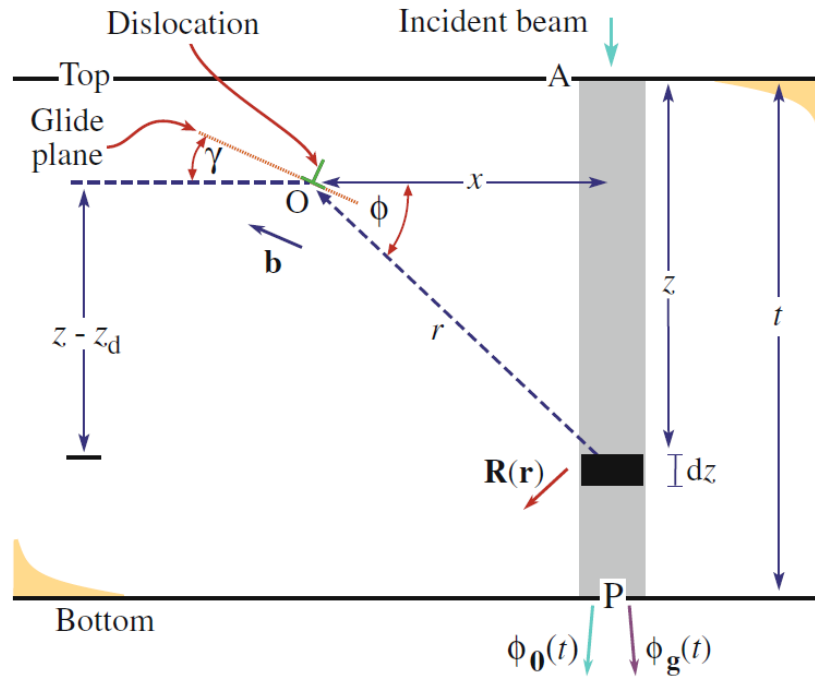


Fig. 2.7 The effect of a dislocation with Burgers vector, \mathbf{b} , at O on a column, distance x away. The effect of the strain field on the electron waves in the column is integrated in increments dz over its total length t , giving amplitude $\phi_0(t)$ and $\phi_g(t)$ at P.

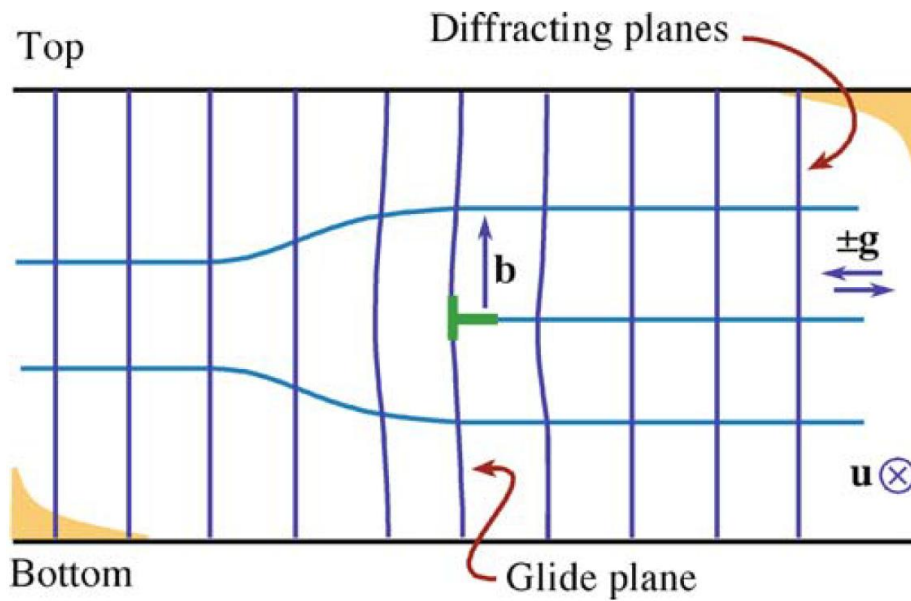


Fig. 2.8 Buckling of the glide planes arises because of the term $\mathbf{g} \cdot \mathbf{b} \times \mathbf{u}$ and is important because it complicates the analysis of \mathbf{b} .

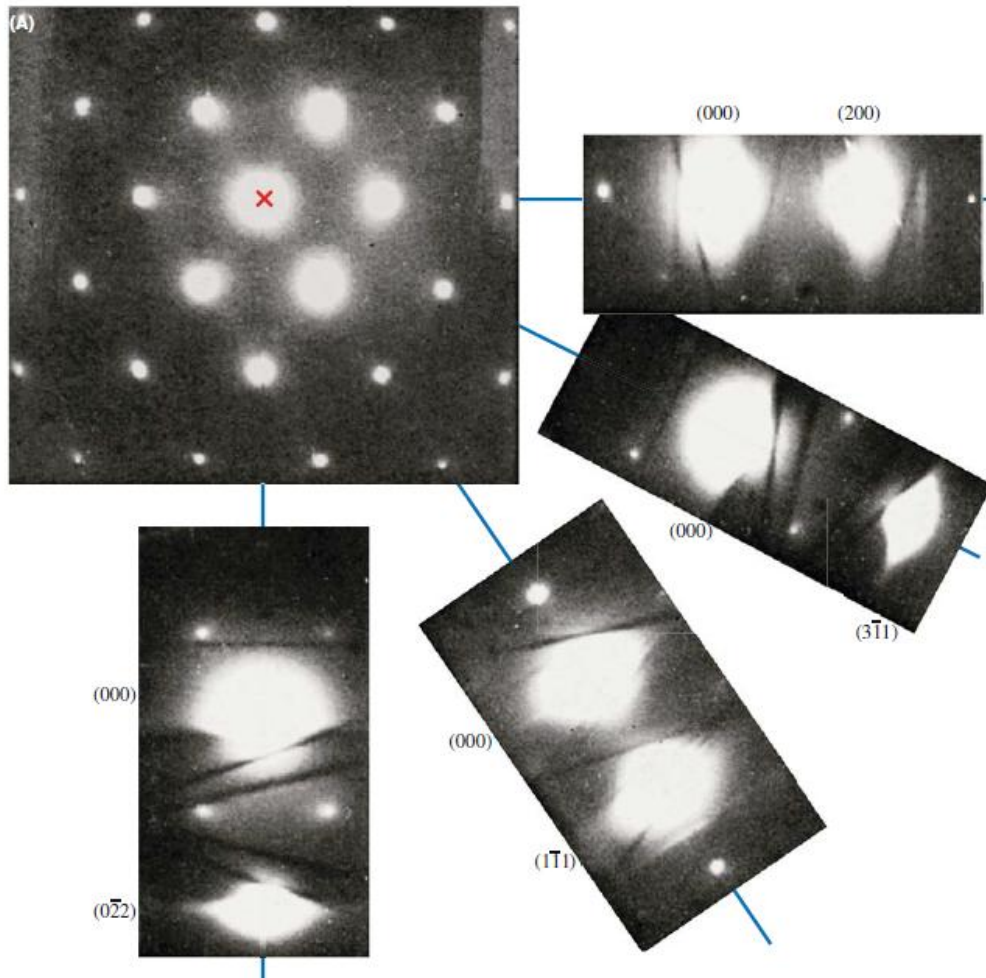


Fig. 2.9 The [011] zone-axis diffraction pattern has many planes diffracting with equal strength. In the smaller patterns, the specimen is tilted so there are only two strong beams, the direct 000 on-axis beam and a different one of the hkl off-axis diffracted beams.

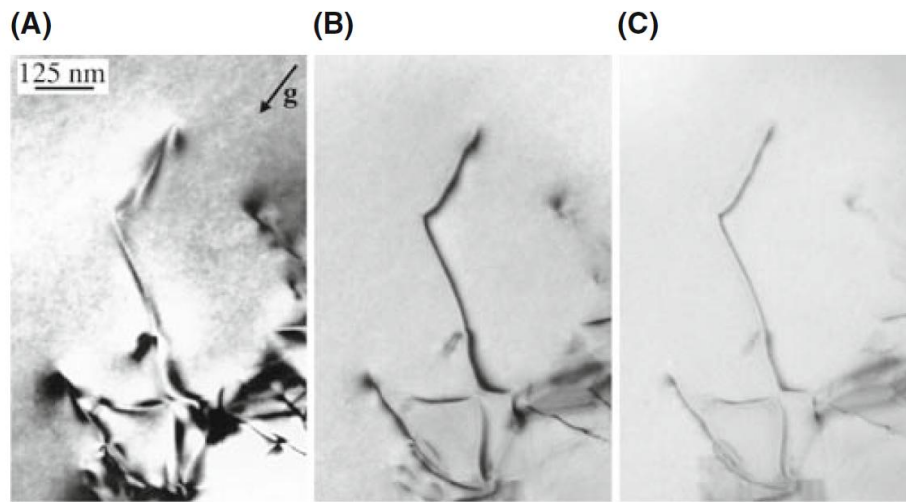


Fig. 2.10 Variation in the diffraction contrast when s is varied from (A) zero to (B) small and positive and (C) larger and positive.

CHAPTER 3 Characterization of FeCrAl-ODS Alloys by Cobalt Addition

3.1 Introduction

In this chapter, we explore the possibility of γ/α transformation by adding Co-element as an austenite former into Al_2O_3 -forming FeCrAl-ODS alloys. The appropriate Co content for γ/α transformation was predicted by constructing a phase diagram using the thermodynamic software FactSage. Then, structural control via γ/α transformation is experimentally verified. Since Co is a radioactive element and high concentration of Co is needed for phase transformation, Co-added FeCrAl-ODS alloys are considered to serve high temperature environment, such as thermal power plant instead of nuclear reactors.

3.2 Alloy design

A certain Al content is essential for Al_2O_3 scale formation. Based on the Fe-Cr-Al oxide map at 1100 °C [63], the critical Al content for Al_2O_3 formation decreases with Cr content increase. However, excessive Cr content induces α' -embrittlement [64, 65]; therefore, 12 wt.% Cr content was selected. The corresponding Al content for possible Al_2O_3 formation could be between 3 and 5 wt.% according to the Fe-Cr-Al oxide map [63]. **Fig. 3.1** shows the pseudo binary phase diagrams for both composition of Fe-12Cr-3Al-xCo and Fe-12Cr-5Al-xCo as a parameter of Co content (wt.%), which were analyzed using the thermodynamic software FactSage with SGTE database. In these figures, BCC_A2 is α -ferrite, B2_BCC is a CoAl intermetallic compound, BCC_A2#2 is pure Cr, and FCC_A1 is γ -austenite. Judging the single α -ferrite, dual phase of α -ferrite and γ -austenite, and single γ -austenite by their pale blue, pale green and pale yellow colors, respectively. These pseudo binary phase diagrams suggest that appropriate amount of Co addition makes it possible to induce the γ/α transformation during cooling after solid solution heat treatment. In this study, 15 wt.% and 25 wt.% Co addition was selected in both alloy systems, as shown by the dotted lines. Four types of specimens were prepared as described in the following section.

3.3 Experimental methods

High purity powders of iron, chromium, cobalt, yttria and 50Al-50Fe alloy were mixed in a sealed stainless steel pot with a ball:powder weight ratio of 10:1. Then, they were mechanically alloyed (MAed) for 72 h (with 23 repetitions of 2 hours of rotation and 1 hour pause for cooling) at 300 rpm under argon gas atmosphere using a planetary type ball mill (Fritsch P-5). The MAed powders were then consolidated at 1150 °C for 1 h using a spark plasma sintering (SPS) under high vacuum (<0.1 Pa) in a 15-mm-diameter and 40-mm-tall hollow-cylinder carbon die with the pressure 45 MPa. The sintered specimens were then homogenized at 1150 °C for 1 h and furnace cooled to room temperature. **Table 3.1** shows the chemical composition of fabricated specimens measured using X-ray fluorescence. The weight percentage of Y_2O_3 was converted from Y content.

The morphology and element distribution were observed using an electron probe micro-analyzer (EPMA, JEOL JXA-8530F) to identify different phases in furnace-cooled specimens. X-ray diffraction (XRD, Rigaku) analysis was also performed at room temperature and 1000 °C to confirm phases with the 2θ scan ranging from 30 to 90 deg at a speed of 2 deg/min. The radiation condition was set at 40 kV and 200 mA with a copper target. High temperature in-situ XRD measurement using a 2D single image shot mode was performed when specimens were cooling from 1000 °C to room temperature at different cooling rates (5 °C/min, 10 °C/min, 30 °C/min, and 50 °C/min) to obtain continuous cooling transformation (CCT) curves. The exposure time and interval time were set at 15 s and 5 s, respectively. B2 phase and oxide particle distributions were analyzed using transmission electron microscopy (TEM, JEOL JEM-2010) and scanning transmission electron microscopy (STEM, FEI Titan G2 80-200). TEM observation specimens were thinned to approximately 100 nm using a focused ion beam (FIB, JEOL JIB-4601F).

3.4 Results

3.4.1 Phase diagram and microstructure characterization

From the computed pseudo binary phase diagram shown in **Fig. 3.1**, three phases are stable at room temperature for four designed alloys; the computed weight

percentages are shown in **Fig. 3.2**. The main phase of the matrix is α -ferrite (BCC_A2) with more than 70 wt.%. The weight percentage of CoAl intermetallic compound (B2_BCC) slightly increases with increasing Al and Co contents at around 10 wt.%, whilst the pure Cr (BCC_A2#2) remains at 12 wt.% for four specimens. The computed atomic percentage comprising the matrix α -ferrite (BCC_A2) is shown in **Fig. 3.3**. The matrix composition has a Fe-Co basis; Cr is completely excluded from the matrix as the pure Cr (BCC_A2#2), and Al is also partly excluded from the matrix because of consumption as the CoAl intermetallic compound (B2_BCC).

Fig. 3.4 shows the elemental mapping of the specimen 5Al25Co, which was analyzed using EPMA. The other three specimens had similar distributions of Fe, Co, Al, Cr and C. There are two types of precipitates. The strong signal of spots dispersed in the matrix of the respective Al and Co mapping indicates that the CoAl intermetallic compounds (B2_BCC) are fine particles. The other precipitate is Cr-carbide phase rather than pure Cr (BCC_A2#2), because carbon is slightly enhanced in the Cr-enriched region. Back scattered electron images at 3000 magnification were taken to measure volume fraction of Cr-carbide. The result shows that 1.03 % Cr-carbides were distributed at the grain boundaries. C-ingress was attributed to the grinding media and attritor parts during the mechanical alloying (MA) process [66, 67]. The diffusion of carbon from the carbon die during the SPS process at high temperature could be also a non-negligible circumstance. The matrix composition analyzed using EPMA for the four specimens is listed in **Table 3.2**. These data are deviated from the computed matrix for Cr and Al contents shown in **Fig. 3.3**, but adequately similar to the average composition in the whole area measured using X-ray fluorescence (**Table 3.1**). The Al and Co matrix compositions measured using EPMA (**Table 3.2**) result not only from the matrix but also the nanosized particles of CoAl intermetallic compound because the electron beam size covers the large amounts of nanosized particles. Cr content up to approximately 10 wt.% in matrix also differs from the computed matrix with almost zero Cr, which is because the solubility limit of Cr in Fe is much larger in Fe-Cr alloys up to 700 K [68-70].

3.4.2 Oxide particle and B2-type CoAl phase characterization

Oxide particles distributed in alloys were observed using TEM, as shown in **Fig.**

3.5. Obviously, there are massive fine and uniformly dispersed Y_2O_3 particles. Few bigger particles which are considered to be Y-Al-O ($YAlO_3$ and $Y_3Al_5O_{12}$) complex oxides [71] are also apparent in the figure; their size is consistent with the characterization using STEM, as identified by arrows in **Fig. 3.8**. The TEM image was also analyzed using image analysis software to obtain the distribution of oxide particles; the results are plotted in **Fig. 3.6** with diameter vs. number density. The bar chart shows that the diameters of most oxide particles are 3-9 nm; the average diameter is 6.2 nm which is of the essence for pinning force calculation.

The B2_BCC phase was furthermore analyzed using TEM and STEM, as shown in **Fig. 3.7**. By selecting the diffraction spot of the B2_BCC intermetallic compound, the CoAl intermetallic compound can be easily revealed with a radius of ~15 nm using dark field imaging, although it is hard to find it using bright field imaging. At lower magnifications of the elemental mapping observed using STEM (**Fig. 3.8**), the dispersed B2_BCC particles correspond to the areas where Al and Co are enriched as highlights. With higher magnification images, as shown in **Fig. 3.8**, the Al-enriched circle overlaps the Co-enriched circle in high-angle annular dark field (HAADF) imaging, which corresponds light gray in contrast with white matrix and darker oxide particles (as identified by arrows), because HAADF imaging is highly sensitive to variations in the atomic number of atoms. For clearer characterization, Fe-Co, Fe-Al, and Co-Al dual elemental mappings are shown in **Fig. 3.9**. The regions where Al and Co are broadly noticed overlap as shown in the circled areas, as shown in **Fig. 3.9(c)**. This overlapped area is identical to that shown in HAADF imaging.

Fig. 3.10 shows the results of XRD analysis at room temperature; only the matrix BCC_A2 ferrite (α) peaks are found. Cr-carbide phase and CoAl intermetallic compound B2_BCC are not identified by XRD because of their small fractions. **Fig. 3.11** shows the XRD results at 1000 °C; specimens 3Al15Co, 3Al25Co and 5Al25Co give almost single austenite (γ), while specimen 5Al15Co remains single ferrite (α). The computed phase diagram shown in **Fig. 3.1** indicates that 3Al15Co, 3Al25Co, 5Al15Co and 5Al25Co contain 96% γ -phase + 4% α -phase, single γ -phase, 72% γ -phase + 28% α -phase and single γ -phase respectively at 1000 °C. The XRD result obviously deviates from the computed phase diagram for specimen 5Al15Co. This specimen does not transform from the α -phase to γ -phase during heating up to

1000 °C. The reason will be discussed in the next section.

3.5 Discussion

In ODS alloys, α to γ phase transformation during heating is dominated by the chemical driving force against pinning force by oxide particles. The chemical driving force can be evaluated by estimating the Gibbs free energy difference between the α and γ phases. Their Gibbs free energies at 1000 °C, calculated using FactSage software and chemical driving force F_{cd} equals $G_\alpha - G_\gamma$, are shown in **Table 3.3**. The 5Al15Co alloy with higher Al content and lower Co content has the lowest chemical driving force because Al is a ferrite-stabilizing element while Co is an austenite-stabilizing element.

The pinning force by the oxide particles can be evaluated using following equation, which was proposed by Zener-Smith [72] and Nishizawa [73].

$$F_{pin} = \frac{3\sigma_{int} \cdot f_v^{2/3}}{4r} \quad (3.1)$$

where F_{pin} is pinning force and σ_{int} is interfacial energy between austenite (γ) and ferrite (α), which was selected as 0.56 J/m² [74]. r is the average radius of oxide particles based on the TEM image analysis. f_v is the volume fraction of oxide particles, which was evaluated by weight and density of raw materials. The results of calculation using Eq. (3.1) are shown along with the chemical driving forces in **Fig. 3.12**. The pinning forces by oxide particles are almost the same among the alloys, while chemical driving forces decrease with decreasing Co concentration and increasing Al concentration. For specimen 5Al15Co, the pinning force caused by oxide particles is greater than the chemical driving force, which suggests that α to γ transformation should be retarded so that the α -phase can remain stable during heating to 1000 °C.

From the XRD results at room temperature (**Fig. 3.10**) and 1000 °C (**Fig. 3.11**), γ to α transformation was observed in specimens 3Al15Co, 3Al25Co and 5Al25Co during cooling. Although the phase transformation in 5Al25Co did not complete at 1000 °C, it was deemed that the Ac3 was around 1000 °C considering such low intensity of α phase. Thus, CCT curves, as shown in **Fig. 3.13**, were constructed using a high temperature in-situ XRD technique with cooling rates of 5 °C/min, 10 °C/min,

30 °C/min and 50 °C/min. From the intensity variation of γ and α , the phase transformation process is clearly displayed. Here for each specimen, three XRD patterns with different phases, i.e. before, during and after transformation, were selected from the data to display the gradual transformation process from the γ to α phase. The phase transformation temperatures A_{r3} and A_{r1} were both decreased with Co content increase in 3Al alloys. When the Al content increased to 5 wt.% for 25Co alloys, the A_{r3} temperature showed small deviation, whereas the A_{r1} temperature presented sharp decrease with cooling rate increase. These CCT curves indicate that by adding Co to FeCrAl-ODS alloys, the γ to α transformation could be achieved.

Phase transformation temperatures (A_{c1} and A_{c3}) of alloys were also measured when they were heated to 1000 °C at 5 °C/min, as shown in **Table 3.4**. For comparison, α/γ transformation temperatures calculated using FactSage (A_{e1} and A_{e3}) and measured during cooling (A_{r1} and A_{r3}) are also shown in **Table 3.4**. The table shows that phase transformation temperatures during heating are much higher than those in equilibrium state predicted using FactSage, while the deviation between A_e and A_r decreases with decreasing cooling rate. Hence phase transformation will not occur during their application period, which can largely guarantee security.

3.6 Conclusion

To develop phase transformable FeCrAl ODS alloys, four Co-added FeCrAl-ODS alloys with chemical composition of Fe-12Cr-(3,5)Al-(15,25) were designed based on computed phase diagram, and four types of alloys were fabricated using MA and SPS and finally annealed at 1150 °C to obtain γ/α transformation. Three phases were confirmed in fabricated alloys at room temperature: a matrix with bcc structure, chromium carbide and a several-tens-nanometer-sized dispersing CoAl B2 phase. These are basically consistent with the computed pseudo binary phase diagram. Nanosized oxide particles are also uniformly dispersed. The γ to α phase transformation was confirmed during cooling for 3Al15/25Co and 5Al25Co alloys by high temperature in-situ XRD, which indicates that the microstructure control of FeCrAl-ODS alloys is feasible with an appropriate amount of Co-addition. Retarding the phase transformation in the 5Al15Co specimen can be explained by the pinning force by oxide particles. Phase transformation temperatures during heating are much

higher than those in the equilibrium state predicted by FactSage. This is also attributed to the oxide particle pinning.

Table 3.1 Chemical composition of samples measured by X-ray fluorescence (wt.%)

Sample ID	Fe	Cr	Al	Co	Y ₂ O ₃
3Al15Co	71.32	11.36	2.79	14.16	0.46
3Al25Co	61.42	11.73	3.00	23.48	0.47
5Al15Co	69.76	11.36	4.69	13.83	0.46
5Al25Co	60.54	11.38	4.74	22.97	0.47

Table 3.2 Chemical composition of matrices measured using electron probe micro-analyzer (wt.%)

Sample ID	Fe	Cr	Al	Co	C
3Al15Co	72.86	10.26	2.59	14.26	0.14
3Al25Co	63.28	10.64	2.46	23.50	0.21
5Al15Co	70.05	10.87	4.12	13.83	0.18
5Al25Co	62.69	9.68	4.35	23.52	0.15

Table 3.3 Gibbs free energies and chemical driving forces at 1000 °C calculated using FactSage (MJ/m³)

Sample ID	3Al15Co	3Al25Co	5Al15Co	5Al25Co
G_{α}	-794.7	0	-590.5	0
G_{γ}	-852.3	-924.1	-595.0	-662.1
F_{cd}	57.6	924.1	4.5	662.1

Table 3.4 Phase transformation temperatures calculated using FactSage and measured using high temperature in-situ XRD (°C)

Phase transformation temperature	A _{e1}	A _{c1}	A _{r1}	A _{e3}	A _{c3}	A _{r3}
3Al15Co	658	838	406~640	-	928	670~726
3Al25Co	652	705	350~520	686	802	550~636
5Al15Co	665	-	-	-	-	-
5Al25Co	652	880	215~600	665	1000	585~640

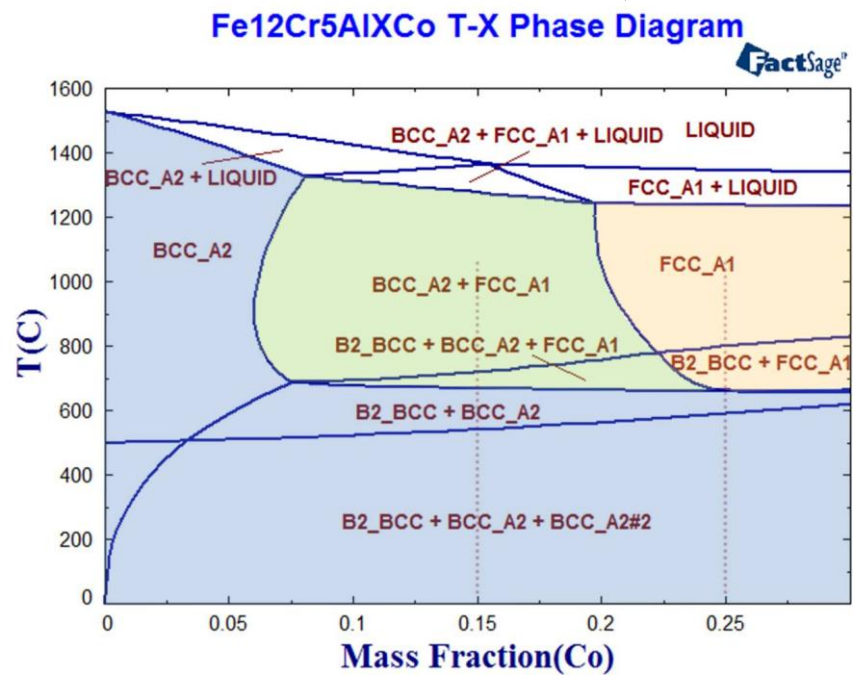
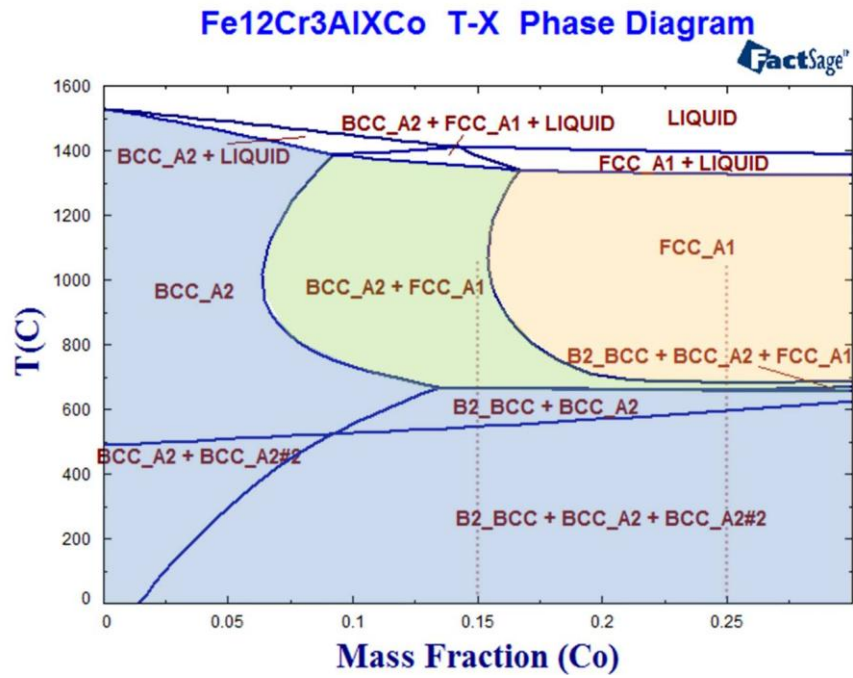


Fig. 3.1 3Al-xCo and 5Al-xCo phase diagrams computed using FactSage

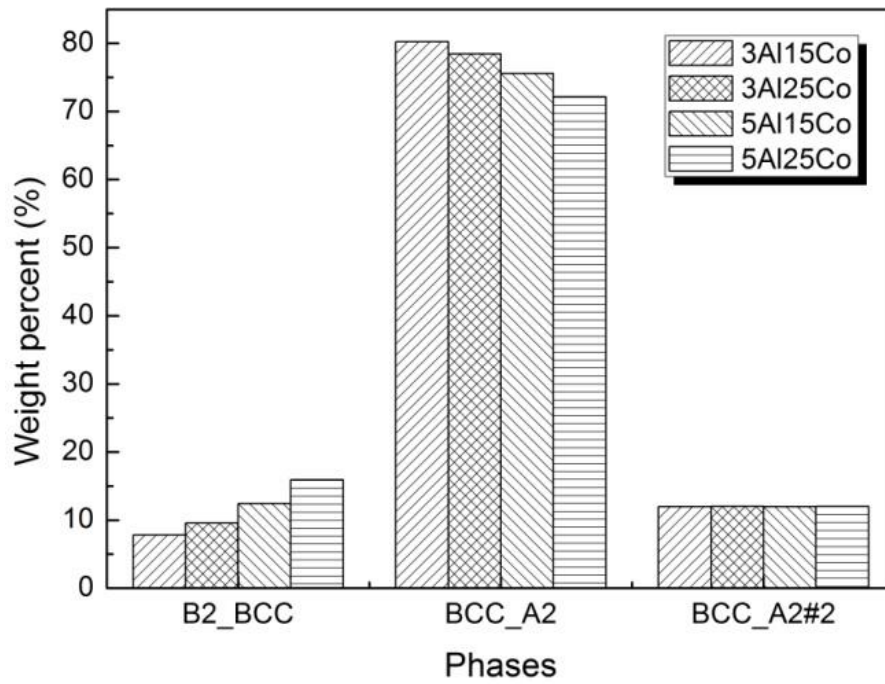


Fig. 3.2 Phase weight percentages at room temperature computed using FactSage

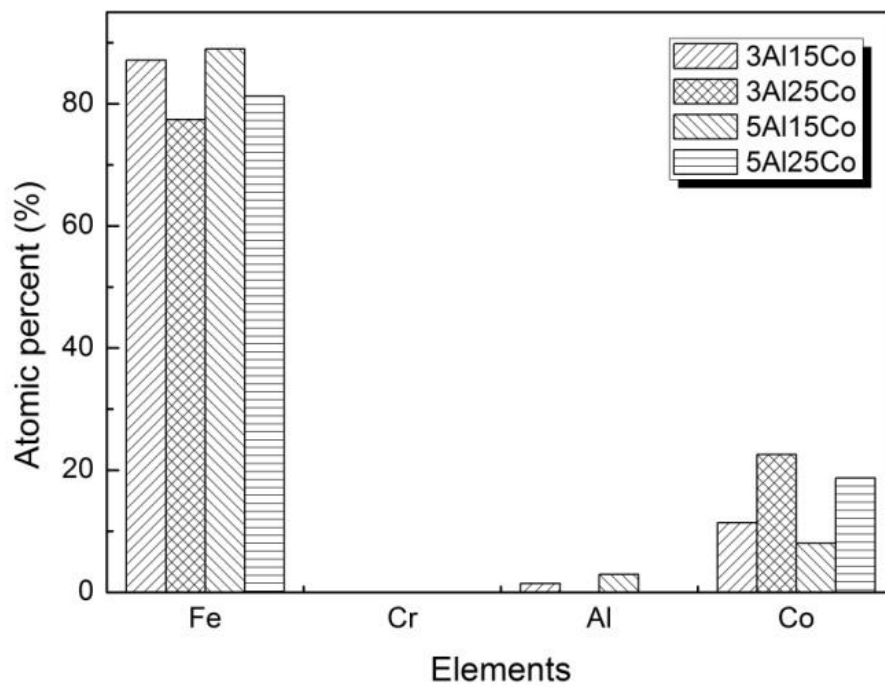


Fig. 3.3 Chemical composition of BCC_A2 phase computed using FactSage

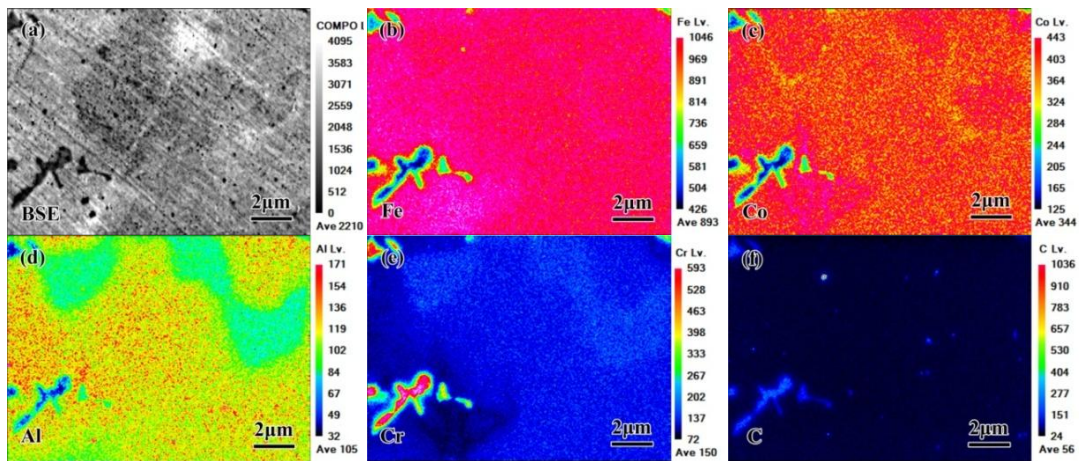


Fig. 3.4 Electron probe micro-analyzer backscattered electron (BES) image (a) and elemental mapping (b)-(f) of 12Cr5Al25Co

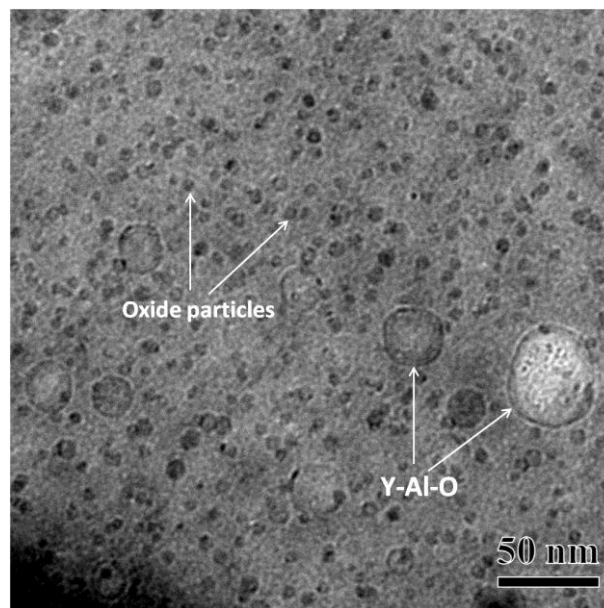


Fig. 3.5 Bright field imaging of oxide particles observed using TEM

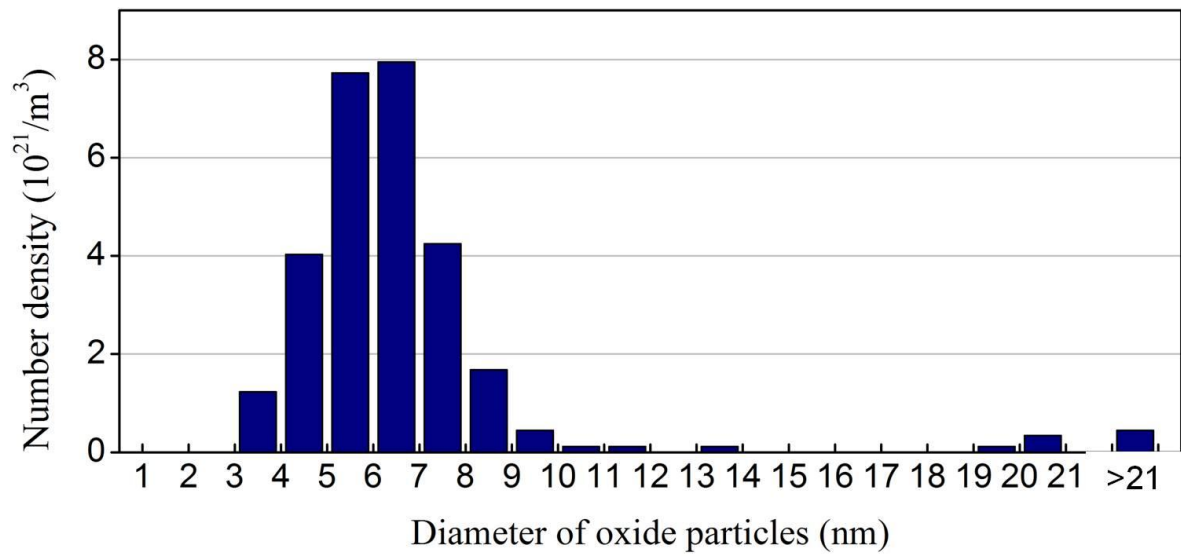


Fig. 3.6 Size distribution of oxide particles

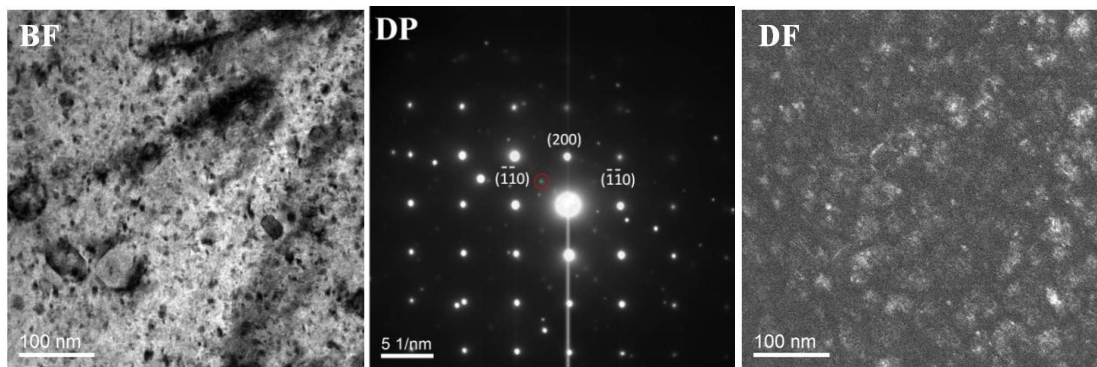


Fig. 3.7 Bright field (BF), diffraction pattern (DP) and dark field (DF) imaging of B2_BCC phase observed using TEM

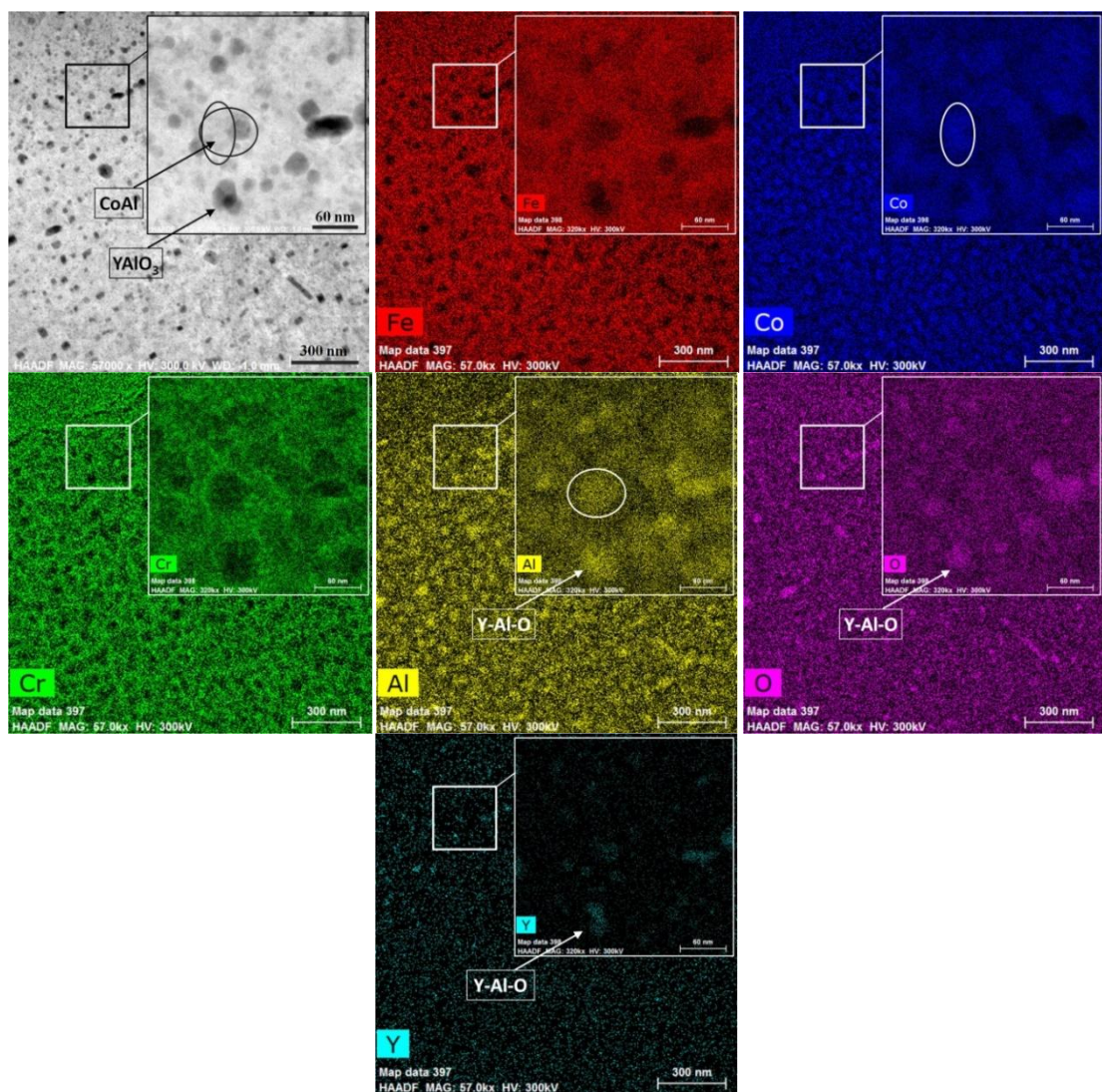


Fig. 3.8 High-angle annular dark field image and corresponding elemental mapping at different magnifications by STEM

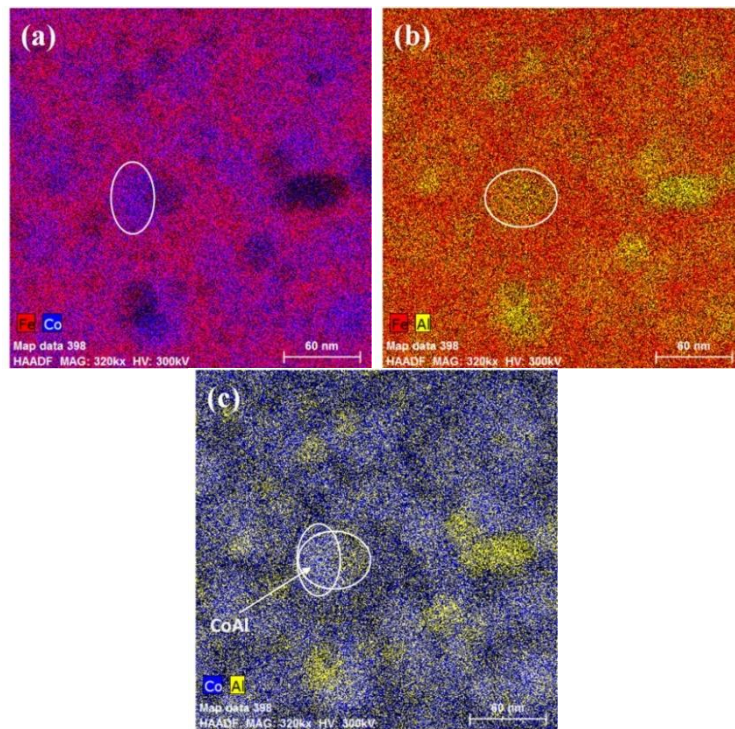


Fig. 3.9 Dual elemental mapping using STEM for (a) Fe-Co, (b) Fe-Al, (c) Co-Al

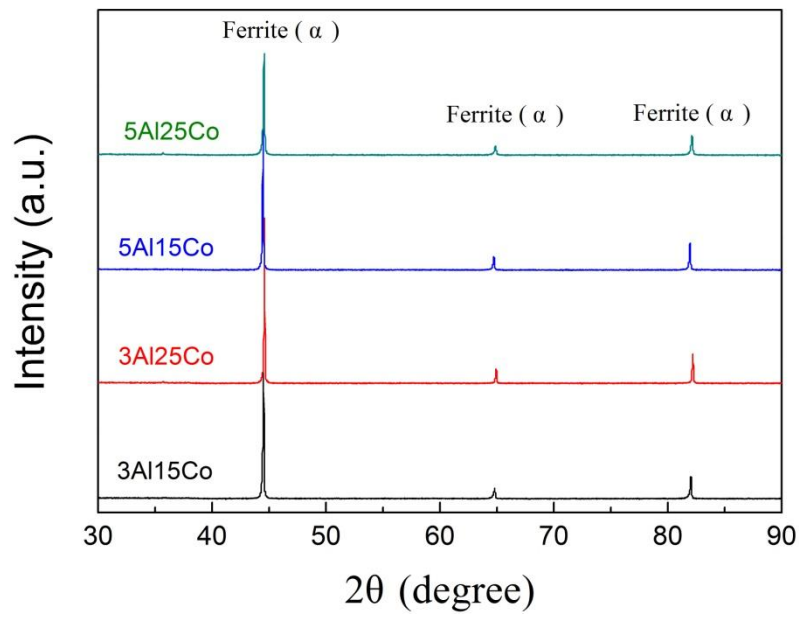


Fig. 3.10 X-ray diffraction patterns of specimens at room temperature

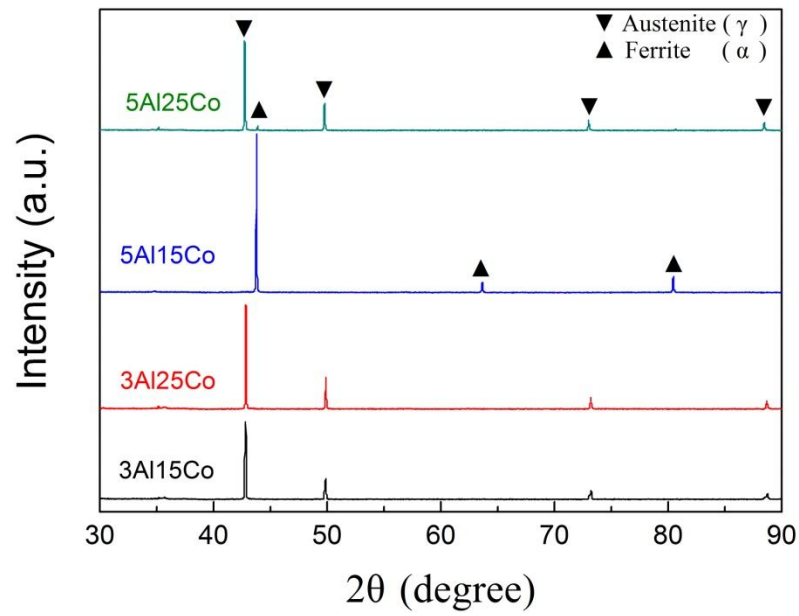


Fig. 3.11 X-ray diffraction patterns of specimens at 1000 °C

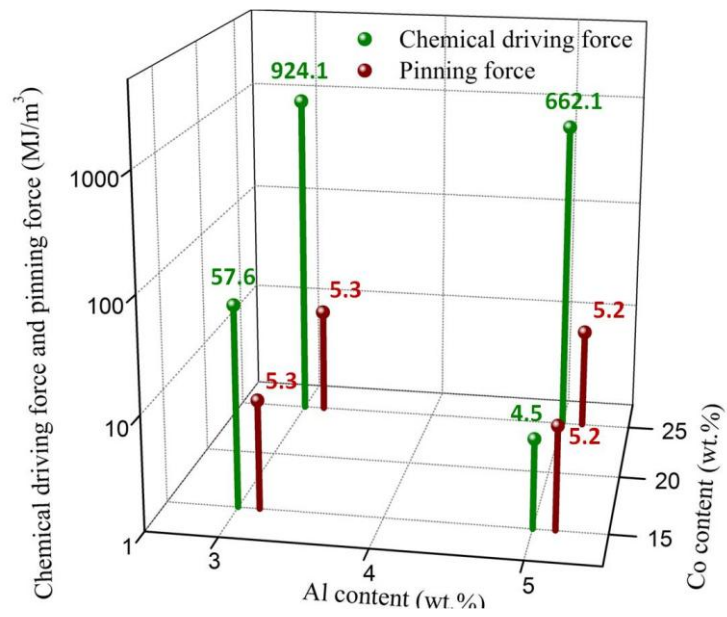


Fig. 3.12 Relationship among Co and Al content, chemical driving force and pinning force (using a logarithmic scale)

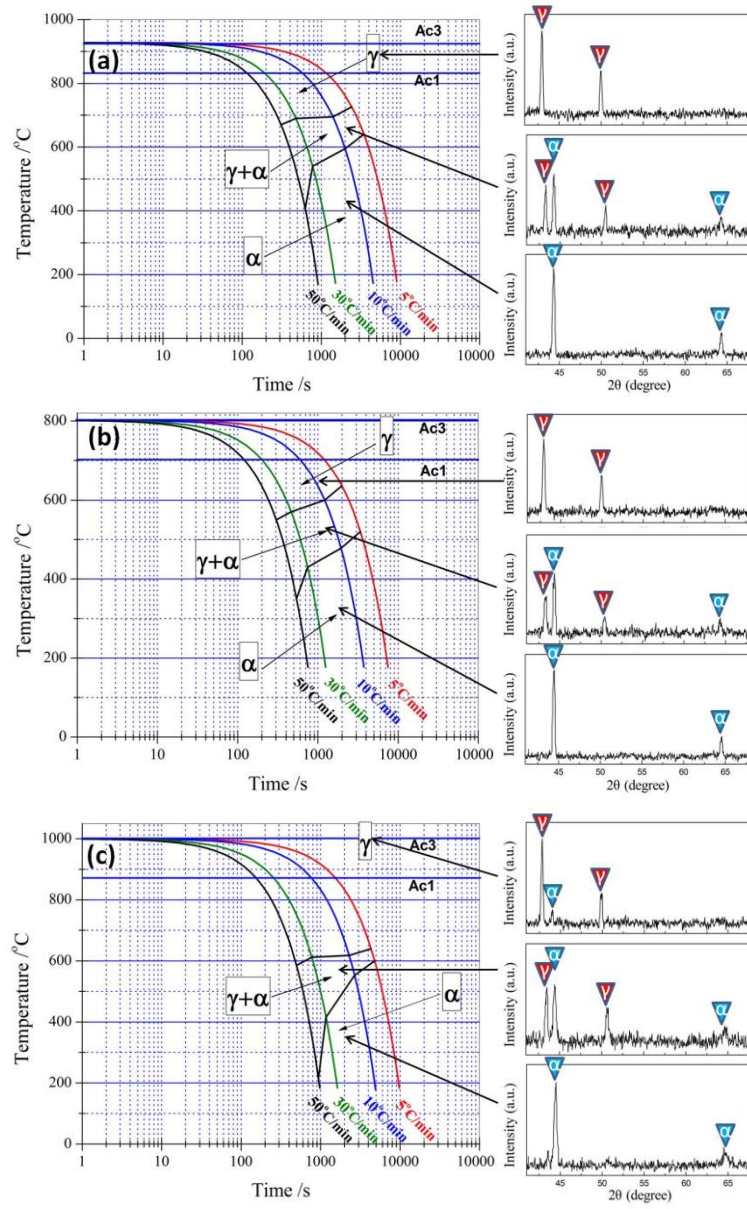


Fig. 3.13 Continuous cooling transformation curves constructed using high temperature in-situ X-ray diffraction, (a) 3Al15Co, (b) 3Al25Co, (c) 5Al25Co

CHAPTER 4 Oxidation behavior of Co-added alloys

4.1 Introduction

FeCrAl alloys are utilized in a number of high-temperature applications such as heating elements, car catalyst substrates, gas burner mats, and industrial furnace furniture. The superior oxidation resistance at elevated temperature of FeCrAl-alloys is due to the formation of a protective alumina scale. FeCrAl ferritic ODS alloys also exhibit good creep resistance, low thermal expansion coefficient, superior irradiation resistance, and low susceptibility to stress corrosion cracking. Thus they have been considered as candidate structural materials for the applications in space industry, chemical industry and next generation fission and fusion nuclear power plants [75–78]. Y_2O_3 nanoparticles are often added in the ODS alloys by using mechanical alloying (MA) approach. The minor additions of reactive elements (RE) Y not only improves the oxidation resistance [79-81] but also the mechanical properties [82-84], in particular creep strength.

The effects of RE addition on oxidation behavior of Al_2O_3 -scale forming alloys have been extensively reviewed [85, 86]. The RE addition such as Y, Zr and Hf are generally known to improve the scale adhesion and slow the scale growth rate. It has often been observed that RE addition induced relatively rapid oxidation rate during the initial stage, followed by significantly slow oxide scale growth in FeCrAl alloys and Ni-based alloys [87-90]. The mechanism of RE addition decreasing growth rate of Al_2O_3 scale was reported due to their segregation at oxide grain boundaries and suppression of outward Al diffusion [90-94]. W. J. Quadakkers [93] and Z. Liu et al [94] studied the sub-parabolic oxidation kinetics of FeCrAlY alloys and explained with the assumption that oxygen grain boundary diffusion is the dominant mass transfer process, and that oxide grain size increases with time. The phenomenon that oxide grain size became finer with RE addition also presented in previous studies [90, 95], which may counteract the positive effect of RE segregation to a certain extent.

In this study, more than 15 wt.% Co was introduced in FeCrAl ODS alloys to modify the alloy substrate to be γ/α phase transformable for better microstructure control as reported in previous study [96]. The modified FeCrAl ODS alloys were developed also for high-temperature service so that the high temperature oxidation

resistance is needed. The effects of Cr and Al contents and RE on the oxidation performance of FeCrAl alloys were extensively studied [95, 97-99], whereas the work on the effect of Co addition was rarely done, let alone such high ratio Co addition was introduced in FeCrAl ODS alloys. Therefore, the high-temperature oxidation behaviors of Co-added FeCrAl ODS alloys were investigated with focusing on the effects of Co addition on the oxidation behavior.

4.2 Experimental method

All Co added alloys were prepared by following processes. High purity powders of iron, chromium, cobalt, yttria and 50Al-50Fe alloy were mixed in a sealed stainless steel pot and they were mechanically alloyed (MAed) under argon gas atmosphere. Then the MAed powders were consolidated by spark plasma sintering [96]. The Co free alloy, 12Cr5Al was manufactured by mechanical alloying and hot extrusion [100]. **Table 4.1** gives the compositions of all the alloys studied in this work, which was measured using X-ray fluorescence analysis. The sintered alloys were then subjected to hot rolling at 1150 °C with a total thickness reduction of 85%. The final homogenization was done at 1150 °C for 1 hour and air cooled to room temperature. Coupons (10 mm × 10 mm × 1 mm) with 1.5 mm diameter holes were cut and polished to a 1 µm finish.

Oxidation experiments were conducted at 1000 °C in a muffle furnace where the specimens were hung using alumina rods in alumina crucibles. Mass gains at different exposure durations (0, 4, 9, 16, 25, 49, 100, 225 h) were measured using a microbalance (Model MC 5, Sartorius) to determine oxidation kinetics.

After oxidation, the specimens were analyzed using X-ray diffraction (XRD, Rigaku Smartlab) to identify phases qualitatively with the 2θ scan ranging from 20 to 90 deg at a speed of 2 deg/min. In order to eliminate the effect of rough uneven surfaces and highlight the intensity of oxide scale peaks, general parallel beam / parallel slit analyzer (PB/PSA) package was selected to conduct XRD measurement. The radiation condition was set at 40 kV and 200 mA with a copper Kα1. The surface morphologies were observed by field emission type scanning electron microscope (FE-SEM, JEOL JSM-6500F) and the polished cross sections were characterized by electron probe micro-analyzer (EPMA, JEOL JXA-8530F). Oxidized 5Al specimens

were further analyzed by scanning transmission electron microscopy (STEM, Hitachi HD-200) and transmission electron microscopy (TEM, 300kV-FEI Titan G2). The TEM samples with ~100 nm in thickness were prepared by focused ion beam milling and FE-SEM imaging (FIB-SEM, JEOL JIB-4601F).

4.3 Results of oxidation test at 1000 °C

4.3.1 Oxidation kinetics

Fig. 4.1 shows mass gains of all alloys oxidized at 1000 °C. Although scale spallation was observed on the 3Al alloys, the mass gains of them are much higher than those of 5Al alloys, which indicate 5Al alloys possess superior oxidation performance comparing with 3Al alloys. The 5Al alloys exhibited similar oxidation rate at the first 25 h, but thereafter, two Co-added 5Al alloys show similar lower growth rate of mass gain than that of 12Cr5Al alloy.

The measured mass gains (Δm) of 5Al alloys as a function of square root of time ($t^{1/2}$) were plotted to assess the oxidation mechanism, as shown in **Fig. 4.2**. The Δm apparently increased linearly with $t^{1/2}$ in the figure, which implies that the oxidation kinetics of 5Al alloys corresponds to a parabolic law defined as Eq. (4.1) up to 225 h. The calculated values of k_p were presented in **Table 4.2**. As expected, the k_p values of Co-added 5Al alloys were very close, whereas that of 12Cr5Al alloy was higher demonstrating a higher oxidation rate of 12Cr5Al alloy.

$$\Delta m = k_p \cdot t^{1/2} + C \quad (4.1)$$

where Δm is measured mass gain and t is corresponding exposure time, C is a constant [101].

4.3.2 Phase composition and morphology of oxide scales

The oxide scale phase composition is an important consideration for alumina formers. **Fig. 4.3** and **Fig. 4.4** show the XRD patterns taken from the oxide scales formed on alloys oxidized at 1000 °C after the exposure time of 225 h. In **Fig. 4.3**, the similar XRD patterns of two 3Al alloys suggest that the oxidation mechanisms of them are similar and the oxide scales consists of mainly Cr_2O_3 , Fe_2O_3 and/or Fe_3O_4 . In addition, it is worth to note that there is no Al_2O_3 detected. The diffraction peaks of

Co-added 5Al alloys in **Fig. 4.4** show that α -Al₂O₃ dominates the oxide scales with a small amount of Cr₂O₃, Fe₂O₃ and/or Fe₃O₄. Based on the analysis of Cr effect on a protective Al₂O₃ scale forming Fe-Cr-Al alloys [98], the formation of Cr₂O₃ is understood to be beneficial for promoting Al₂O₃ scale formation and this Cr effect is called as the third element effect. On the contrary, the Cr₂O₃ diffraction peak at 33.3 ° was barely detected for 12Cr5Al, although the dominant oxide was α -Al₂O₃ as the Co-added 5Al alloys possessed.

There is a marked difference in scale morphology on oxidized 3Al and 5Al samples. **Fig. 4.5 (a)** and **Fig. 4.5 (b)** show the relatively adherent, rough surface on 3Al15Co and the partially spalled scale on 3Al25Co, respectively. In fact, an amount of fine spalls occurred during the oxidation test of 3Al15Co despite the morphology seems adherent. The severe scale spallation on 3Al25Co may lead to lower increase of weight gain for the later 150 h comparing with that of 3Al15Co. The scales formed on 5Al alloys shown in **Fig. 5 (c)-(e)** are much more uniform and adherent than those on 3Al alloys. What appear to be pores on the scale surfaces formed on the alloys with Co are actually the centers of a close-packed ridge structure, where oxide grain boundaries appear to be associated with each ridge [80].

4.3.3 Chemical composition and microstructure of oxide scales

The EPMA elemental mapping analysis was carried out for the cross-section of all tested samples to clarify the element distribution in the oxide scales. **Fig 4.6** displays the cross-sectional secondary electron images (SEI) and elemental mappings of 3Al alloys after 225 h oxidation at 1000 °C. Both of the oxide scales possessed external layer and internal oxidation zone; the external layer was mainly composed of iron, chromium and oxygen together with a certain amount of cobalt; the internal oxidation zone was formed by the reaction between the penetrated oxygen and aluminum in the substrate. The size of alumina particles in the internal oxidation zone became larger with the distance away from the interface between the oxide scale and substrate. However, a continuous alumina layer was not formed on the surfaces of both 3Al alloys. Strong signals are presented at the bottom of Al elemental mapping in **Fig 4.6 (a)** but not at the corresponding oxygen elemental mapping. These Al enriched particles are considered to be Al nitride, which is a common phenomenon for FeCrAl

alloys with low Al content oxidized at high temperature in air.

The cross-sectional SEI and elemental mappings of 5Al alloys after 225 h oxidation at 1000 °C are shown in **Fig. 4.7**. These images revealed that compact and uniform scales were formed on the surfaces of all 5Al alloys. The scales formed on 5Al alloys were mainly consisted of aluminum and oxygen, and there was a thin layer composed of Cr, Fe and O at the top of oxide scale, which was in good agreement with the XRD results. Meanwhile, a small amount of cobalt presented at the top thin layer of scales on the 5Al Co-added alloys.

For further analysis of scales on the 5Al alloys, the TEM samples were observed using STEM to display scale microstructures. In **Fig. 4.8**, it is obvious that the total scale thickness of 12Cr5Al is greater than those of Co-added 5Al samples, which is in accordance with the tendency of mass gain shown in **Fig. 4.1**. On the other hand, the outer layer of oxide scale can be noted on both 5Al15Co and 5Al25Co. In fact, there was also an outer layer on the oxide scale of 12Cr5Al, which was confirmed using STEM elemental mapping, as shown in **Fig. 4.9**. Based on the statistical measurement, the detailed results of scale thickness and grain size measured around middle area are shown in **Table 4.3**. The thickness of outer layer increased and that of inner layer decreased with cobalt addition. The outer layer on the oxide scale of 12Cr5Al was thinnest and the inner layer was thickest, which accounted for the relatively weak intensity of Cr_2O_3 diffraction peak in XRD result. In addition, **Fig. 4.8** shows that the lateral grain size within the scale increases with depth beneath the oxide/gas interface and this phenomenon becomes more apparent with cobalt addition, which can also be determined by the statistical results.

4.3.4 Segregation of reactive element

Reactive elements have great impact on the high temperature oxidation behavior of FeCrAl alloys. Previous studies stated that reactive elements were more favorable to react with oxygen than other elements and segregation of them was observed at oxide grain boundary. The segregation of yttrium in this study was also confirmed as shown in **Fig. 4.10**. The segregation of Y at the grain boundaries was detected for all 5Al alloys.

4.4 Results of oxidation test at 800 °C and 900 °C

Considering the effect of matrix structure on the oxidation behavior and the effect of Co content on the oxidation behavior of 3Al alloys, 12Cr3Al5Co alloy was additionally designed to subject oxidation test at 800 °C and 900 °C.

4.4.1 Oxidation kinetics

Fig. 4.11 shows the mass gains of all alloys oxidized at 800 °C. For the 5Al alloys, the mass gain after 225 h oxidation decreased as Co content increased, which implied the Co addition was beneficial for the oxidation behavior of Fe12Cr5Al alloy and the results were in good agreement with the results of 1000 °C oxidation test. It is also noted that the mass gain of Co-added 5Al alloys were higher than that of 12Cr5Al alloy at the early stage of oxidation test. This may illustrate that Co was preferentially oxidized in the transient oxidation stage. On the contrast, the mass gain of 3Al alloys after 225 h oxidation increased as Co content increased, which suggested the effect of Co addition on oxidation behavior of 3Al alloys at 800 °C was different with 5Al alloys.

Fig. 4.12 shows the mass gains of all alloys oxidized at 900 °C. At the early stage of oxidation test, Co-added 5Al alloys showed higher mass gains than that of 12Cr5Al alloy and this trend was similar to the oxidation results at 800 °C. The mass gains of 5Al alloys after 225 h oxidation were nearly same and it was expected that the mass gain of 12Cr5Al alloy was over those of Co-added 5Al alloys if the oxidation test continued. For 3Al alloys, the Co addition was also detrimental for the oxidation performance at 900 °C. The 3Al 15Co alloy even displayed a severe oxidation with a high mass gain of 3.5 mg/cm².

4.4.2 Phase composition and morphology of oxide scales

Phase compositions of oxide scale on all alloys oxidized at 800 °C and 900 °C were shown in **Fig. 4.13**. The Cr₂O₃ peaks were apparently detected in all Co-added alloys, which is consistent with the XRD results of oxidation test at 1000 °C. Based on the analysis of **Fig. 4.13**, it is believed that 12Cr5Al alloy oxidized at 800 °C and 900 °C may also possess a thin chromia scale. Alpha-Alumina scale was detected in all alloys oxidized at 800 °C and 900 °C except for the 3Al15Co alloy oxidized at

900 °C. The main phase of oxide scale on the surface of 3Al15Co alloy oxidized at 900 °C was Cr_2O_3 from the XRD result.

Fig. 4.15 shows surface morphologies of alloys after 225 h oxidation at 800 °C. All of them displayed even and uniform surfaces and “pores” can be noted as those on the surfaces of alloys oxidized at 1000 °C. 3Al15Co alloy shows much different surface morphology comparing with those of other 5 images in **Fig. 4.15**, which displays the surface morphologies of alloys oxidized at 900 °C. The surface was rough but did not show obvious spalls. The others showed similar surface morphologies as those on the alloys oxidized at 900 °C.

4.4.3 Chemical composition and microstructure of oxide scales

Fig. 4.16 displays the cross-sectional secondary electron images (SEI), backscattered electron images (BSE) and elemental mappings of alloys after 225 h oxidation at 800 °C. All alloys possessed scales mainly composed of Al and O and a certain amount of Fe, Cr and Co could be also detected, which confirmed the XRD results. The thickness of scales increased with increase of Co content for the 3Al alloys and those of the 5Al alloys displayed opposite results, which is consistent with the mass gain measurement results.

Fig. 4.17 displays the cross-sectional secondary electron images (SEI), backscattered electron images (BSE) and elemental mappings of alloys after 225 h oxidation at 900 °C. There are two layers in the oxide scale of 3Al15Co alloy as shown in **Fig. 4.17(b)**; the external layer was predominated by Cr and O; the internal oxidation zone contained discontinuous particles composed of Al and O. The oxide scales of other 5 alloys were predominated by Al and O as the results obtained at 800 °C and 1000 °C.

In order to clarify the opposite effect of Co addition on 3Al alloys and 5Al alloys, the cross-sections of 3Al5Co and 3Al25Co alloys after 16 h and 225 h oxidation at 800 °C were observed using STEM as shown in **Fig. 4.18**. The thicknesses of scales on the surfaces of 3Al25Co alloy are thicker than those on the surface of 3Al5Co alloy.

4.5 Discussion

4.5.1 Internal oxidation and external scale formation at 1000 °C

If an alloy contains a sufficient concentration of Al, then the alloy can form a protective external Al_2O_3 scale. Conversely, if the component is dilute, then internal oxidation results, destroying the alloy. The critical Al content $N_{\text{Al}}^{\text{O}*}$ can be estimated using following equation [102]

$$N_{\text{Al}}^{\text{O}*} = \left(g_{\text{Al}_2\text{O}_3}^* \frac{\pi}{2\nu} \frac{V_{\text{A}}}{V_{\text{OX}}} \frac{N_{\text{O}}^{(\text{s})} D_{\text{O}}}{D_{\text{Al}}} \right)^{1/2} \quad (4.2)$$

where $g_{\text{Al}_2\text{O}_3}^*$ is the critical volume fraction of internal oxide needed for the transition to external scale and ν is the stoichiometric number, which is 1.5 for Al_2O_3 ; V_{A} and V_{OX} are the molar volumes of the alloy and the oxide; D_{O} and D_{Al} denote the diffusion coefficient of oxygen and of aluminum in the alloy, while the $N_{\text{O}}^{(\text{s})}$ means the mole fraction of oxygen dissolved in the substrate.

The critical Al content was estimated to be 6 wt.% ~ 7 wt.% for Fe-xAl-0.5Y₂O₃ alloys (wt.%) at 1000 °C in air using practical oxidation tests and it increased with temperature above 1000 °C [103]. Since the third element effect of Cr could reduce the experimental level of $N_{\text{Al}}^{\text{O}*}$ [98], Z. G. Zhang et al. [97] reported that 5 wt.% of Al was sufficient to form an exclusive Al_2O_3 scale on Fe-xAl-xCr alloys by 10 wt.% of Cr addition at 1000 °C in 1 atm oxygen. A more recent investigation that the oxidation behavior of Fe-xAl-14Cr-0.6Y₂Ti₂O₇ (wt.%) at 1100 °C in air revealed that the critical Al content should be greater than 3 wt.% [99]. Therefore, it can be concluded that the value of $N_{\text{Al}}^{\text{O}*}$ ranges between 3 wt.% ~ 5 wt.% for ferritic Fe-xAl ODS alloys with more than 10 wt.% of Cr addition at 1000 °C.

In present study, the 3Al alloys transformed to austenite at 1000 °C as shown in **Table 4.4**. The value of $N_{\text{O}}^{(\text{s})} D_{\text{O}}$ in ferritic Fe was several times higher than that in austenitic Fe [28], whereas the value of D_{Al} in ferritic Fe was two orders of magnitude higher than that in austenitic Fe [97]. The other parameters in Eq. (2) can be assumed same. Then, the $N_{\text{Al}}^{\text{O}*}$ of austenitic alloys was believed higher than that in ferritic alloys, which could be the main reason for sever internal oxidation in the 3Al alloys. The other key point was that Y₂O₃ was used for dispersion strengthening particles in this

work and it may consume a certain amount of Al to form Y-Al-O complex oxide so that the concentration of solute Al in 3Al alloys could be lower than the value shown in **Table 4.1**. Consequently, the slow diffusivity of Al in austenitic substrate and the low solute concentration of Al led to the discontinuous aluminum oxide in the internal oxidation zone of 3Al alloys at 1000 °C.

4.5.2 Effect of cobalt addition on reactive element effect at 1000 °C

At 1000 °C, the mass gain results showed that with more than 15 wt. % cobalt addition the rate of oxidation 5Al alloys became slower. Meanwhile, the total thickness of oxide scales decreased, while the thickness of outer layer increased and the grain size increased as cobalt was added as shown in **Fig. 4.8**. Y segregation at Al₂O₃ grain boundaries was observed for all 5Al alloys, which implied the blocking effect on Al outward diffusion from Y segregation worked on all of them [104]. However, thickness of the outer layer increased with addition of Co, which suggested that the Y blocking effect for outward Al diffusion was reduced by Co addition. Moreover, larger grain size of Al₂O₃ scale formed on the Co-added 5Al alloys also suggesting that the Y segregation was weakened with Co addition. In contrast, the enhancement of oxygen inward diffusion was verified by the thickest inner layer on 12Cr5Al.

It is widely accepted that oxide grain boundary diffusion dominates the mass transfer process for α -Al₂O₃ growth [93, 94]. Therefore, a concept of the effective diffusion can be used to explain the results. A useful way of describing diffusion in a polycrystalline material was proposed by Hart [105] and adapted by Smeltzer et al. [106] to the nickel oxidation case. An effective diffusion coefficient is defined as a weighted sum of lattice and boundary contributions

$$D_{\text{eff}} = D_L(1 - f) + D_{\text{GB}}f \quad (4.3)$$

where f is the fraction of diffusion sites within the boundary, and D_L and D_{GB} are the diffusion coefficients for the lattice and boundaries, respectively [102]. The grains can be assumed to be columnar and are square in the top view with a grain size r_G as the schematic shown in **Fig. 4.19**. The black lines in the top view are grain boundaries, and the number of them per unit area is $2/r_G$. Then f can be expressed to be

$$f = \frac{2\delta_{\text{GB}}}{r_G} \quad (4.4)$$

where δ_{GB} denotes the grain boundary width. Since the diffusion of Al and O in the lattice is known to be much lower than D_{GB} [107, 108], the fraction of diffusion sites within the boundary f becomes of importance. Eq. (4.3) can be rewritten to be

$$D_{eff} = \frac{2D_{GB}\delta_{GB}}{r_G} \quad (4.5)$$

Based on the definition of D_{eff} and k_p , the following relation can be derived

$$\frac{D_{eff}^{Ca}}{D_{eff}^{Cf}} \propto \frac{k_p^{Ca}}{k_p^{Cf}} \quad (4.6)$$

Here, D_{eff}^{Ca} and k_p^{Ca} are the effective diffusion coefficient and parabolic oxidation rate constant of Co-added alloys; D_{eff}^{Cf} and k_p^{Cf} are those of Co free alloy. For the oxidation test at 1000 °C in air, the δ_{GB} and D_{GB} can be assumed to be same for all 5Al alloys, then the ratios of D_{eff} and k_p were calculated to be 0.86 and 0.65 respectively (average values of r_G and k_p of two Co-added alloys were used). It seems that the ratio of experimental k_p was lower than that of theoretical D_{eff} . In consideration of the grain expansion with depth, the critical diffusion should occur at the interface between scale and substrate. Thus, the interfacial grain size was measured and the results were showed in **Table 4.3**. The D_{eff} ratio was recalculated using the interfacial grain size and the result was 0.71, which was close to the k_p ratio. Therefore, the slow oxidation kinetics of Co-added alloys can be attributed to the grain coarsening, which suggests that Co addition weakened the effect of Y segregation.

4.5.3 Influence of cobalt addition on solute Y concentration

According to the above analysis of Al_2O_3 scale, the Y segregation at grain boundaries was weakened by Co addition, which might be due to the amount of Y incorporated in the Al_2O_3 was reduced. **Fig. 4.20** shows the oxide particles in 5Al alloys prior to oxidation test characterized by TEM. Two fields of view were observed for each 5Al alloy and statistical results showed that the volume fraction of oxide particles in 12Cr5Al, 5Al15Co and 5Al25Co were 0.41 %, 0.56 % and 0.53 %, respectively. The theoretical volume fraction of oxide particles calculated using weight and density of raw materials was approximately 0.75 %. Thus, it can be deduced that the Co addition might decrease the solubility of Y in bcc matrix resulting in the suppression of Y segregation in the Al_2O_3 scale.

4.5.4 Effect of cobalt addition on oxidation rate at 800 °C and 900 °C

The oxidation behavior of 5Al alloys oxidized at 800 °C and 900 °C are similar to those of them oxidized at 1000 °C, hence the oxidation mechanism can be considered the same. However, the oxidation behavior of 3Al alloys were opposite, which suggested that the oxidation mechanisms of 3Al alloys and 5Al alloys were different. At 800 °C, the mass gains of 3Al alloys were higher than those of 5Al alloys, and it is apparent that the oxidation behaviors of 3Al alloys oxidized at 800 °C became worse with Co content increase, as shown in **Fig. 4.11**. All the alloys formed an Al₂O₃ scale after 225 h oxidation, thus the growth rate of Al₂O₃ increased with Co content increase. Under relatively lower temperature of oxidation such as 800 °C and 900 °C, metastable Al₂O₃ is expected to form initially and remained longer oxidation time. Ni oxide scale formation in the transient oxidation stage was reported retarding the phase transformation from metastable Al₂O₃ to α -Al₂O₃ [109]. On the surfaces of Co-added alloys, cobalt oxide was confirmed so that higher amount cobalt oxide formation on the 3Al alloys with higher Co addition might prevent the transformation to the α -Al₂O₃ since Co oxide has similar properties with NiO. Therefore, the fast growing oxide of metastable Al₂O₃ remained longer, which caused the faster oxidation kinetics. Yoneda et al. [110] studied the initial transient oxidation of Fe-xCr-3Al alloys up to 900 °C and they stated that the internal Al₂O₃ precipitates were formed at the initial stage of oxidation and they connected to form a continuous Al₂O₃ scale in the following oxidation stage. Comparison of **Fig. 4.18 (c)** and **Fig. 4.18 (d)** implied that the grain size of Al₂O₃ scale decreased with Co content increase, which meant that Co addition may decrease the size of Al₂O₃ precipitates at the initial stage so that the grain size decreased. As discussed above, the small grain size led to higher oxidation kinetics.

When the oxidation temperature increased to 900 °C, the 3Al15Co alloy became dual phase. Since the Al concentrations in α and γ were different, the preferential concentration of Al may lead to inferior oxidation performance. Insufficient Al content and/or slow diffusivity of Al in austenitic matrix resulted in a less protective Fe-rich oxide scale formation on the dual phase alloy.

4.6 Conclusion

The oxidation behavior of 3Al and 5Al alloys was studied at 800 °C, 900 °C and 1000 °C in air. Protective alpha-alumina scales were formed on the surfaces of all 5Al alloys at the temperature range from 800 °C to 1000 °C. The low solute concentration and slow diffusivity of Al led to the discontinuous aluminum oxide in the internal oxidation zone of austenitic 3Al alloys at 1000 °C. Y segregation at the grain boundaries was confirmed in all 5Al alloys. Meanwhile, the outer layer thickness and the grain size of alumina increase with increase in Co content of 5Al alloys oxidized at 1000 °C were attributed to the suppression the effect of Y by Co addition. Moreover, the decrease of oxidation kinetics of Co-added 5Al alloys was attributed to the increase of the lateral grain size of alumina which led to the fraction of diffusion sites within the boundary decrease. On the other hand, protective alpha-alumina scales were also formed on the surfaces of 3Al alloys at the temperature range from 800 °C to 900 °C except for the dual phase 3Al15Co alloy oxidized at 900 °C. The Co addition was detrimental to the oxidation kinetics when 3Al alloys were oxidized at 800 °C and 900 °C. The severe oxidation of 3Al15Co alloy at 900 °C may be due to the phase transformation process.

Table 4.1 Chemical composition of samples measured by X-ray fluorescence (wt.%).

Sample ID	Fe	Cr	Al	Co	Y ₂ O ₃
3Al5Co	80.70	11.45	2.67	4.83	0.46
3Al15Co	71.32	11.36	2.79	14.16	0.46
3Al25Co	61.42	11.73	3.00	23.48	0.47
12Cr5Al	83.20	11.72	4.71	-	0.47
5Al15Co	69.76	11.36	4.69	13.83	0.46
5Al25Co	60.54	11.38	4.74	22.97	0.47

Table 4.2 Parabolic rate constants of 5Al alloys oxidized at 1000 °C in air for 225 h.

Sample ID	Parabolic rate constant, $k_p \times 10^{-2}$ (mg cm ⁻² h ^{-1/2})
12Cr5Al	2.42
5Al15Co	1.63
5Al25Co	1.53

Table 4.3 Statistical results of scale thickness and grain size (nm).

Sample ID	Total thickness	Thickness of outer layer	Grain size	Grain size near the scale/alloy interface
12Cr5Al	2180	100	513	545
5Al15Co	1750	128	619	804
5Al25Co	1800	172	581	739

Table 4.4 Matrix structures of all alloys.

Sample ID	800 °C	900 °C	1000 °C
3Al5Co	α	α	α
3Al15Co	α	$\alpha + \gamma$	γ
3Al25Co	γ	γ	γ
12Cr5Al	α	α	α
5Al15Co	α	α	α
5Al25Co	α	α	γ

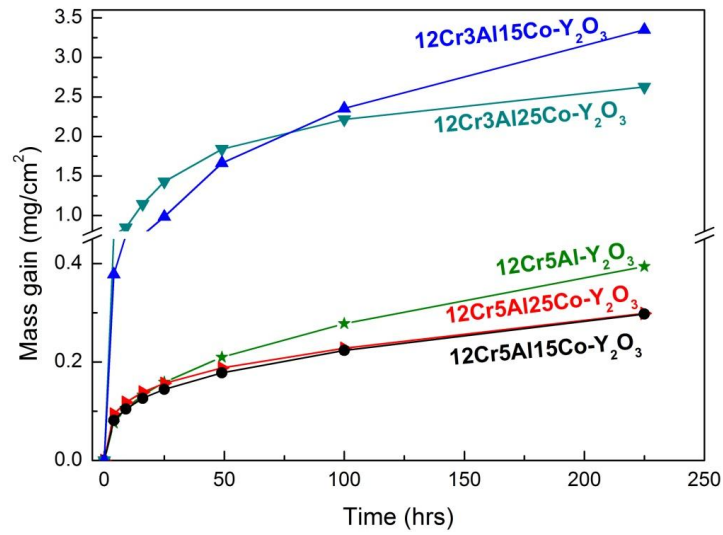


Fig. 4.1 Mass gain of alloys oxidized at 1000 °C in air as a function of time

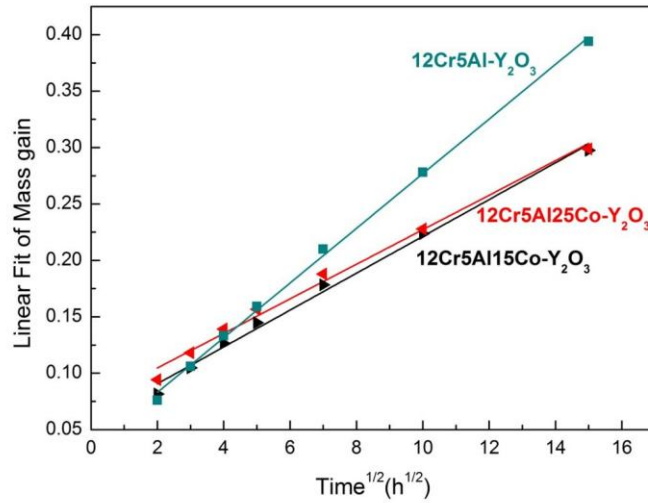


Fig. 4.2 Parabolic plot of mass gain versus square root of time for alloys oxidized at 1000 °C in air

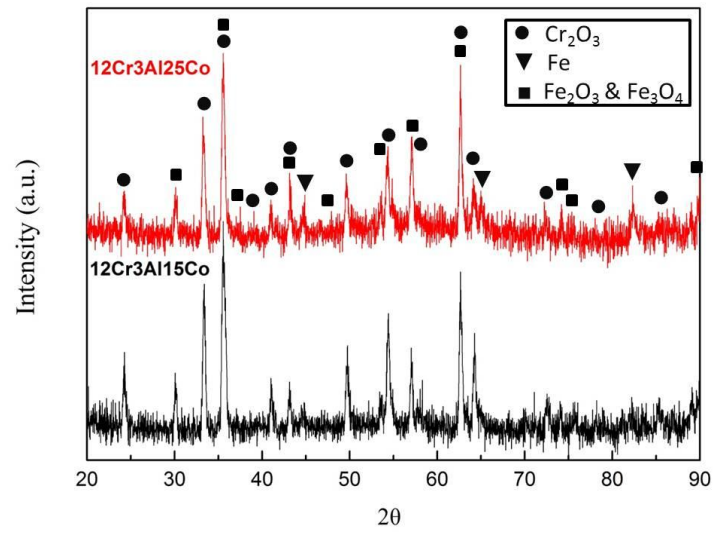


Fig. 4.3 XRD patterns for 3Al alloys after 225 h oxidation at 1000 °C in air

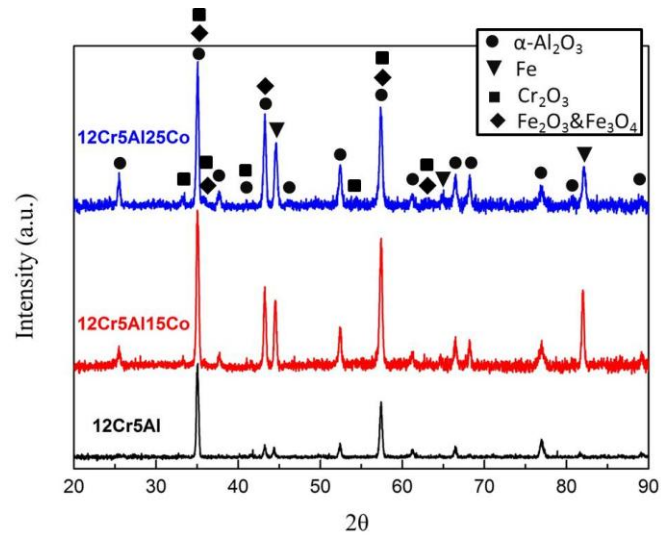


Fig. 4.4 XRD patterns for 5Al alloys after 225 h oxidation at 1000 °C in air

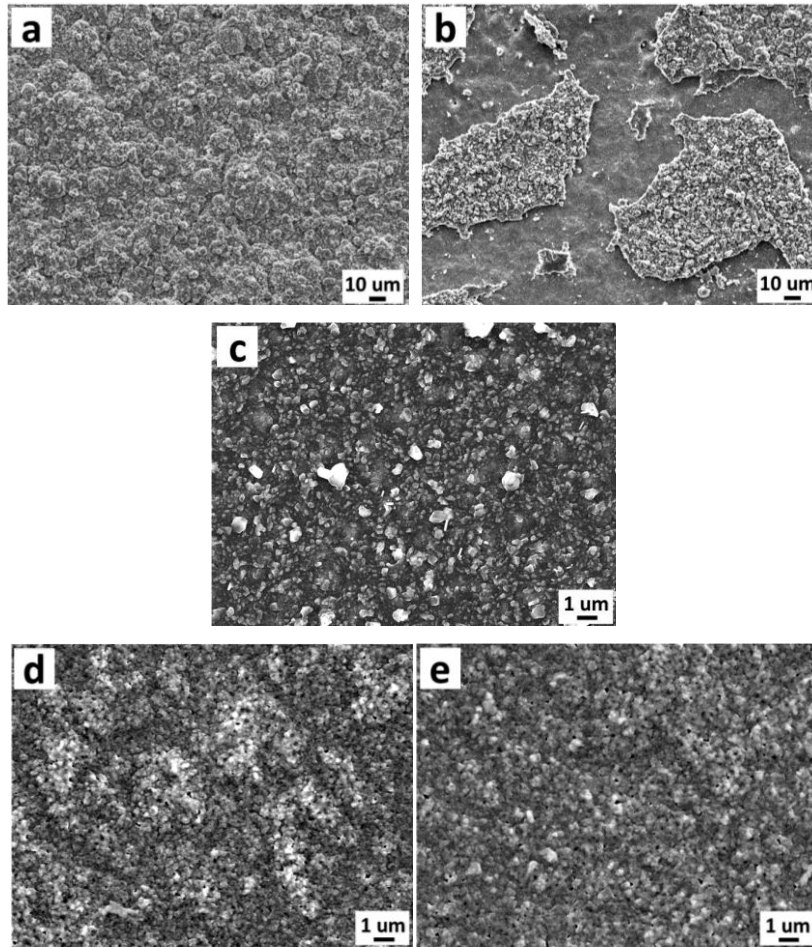


Fig. 4.5 Surface morphologies of alloys after 225 h oxidation at 1000 °C in air: a) 3Al15Co alloy, b) 3Al25Co alloy, c) 12Cr5Al alloy, d) 5Al15Co alloy, e) 5Al25Co alloy

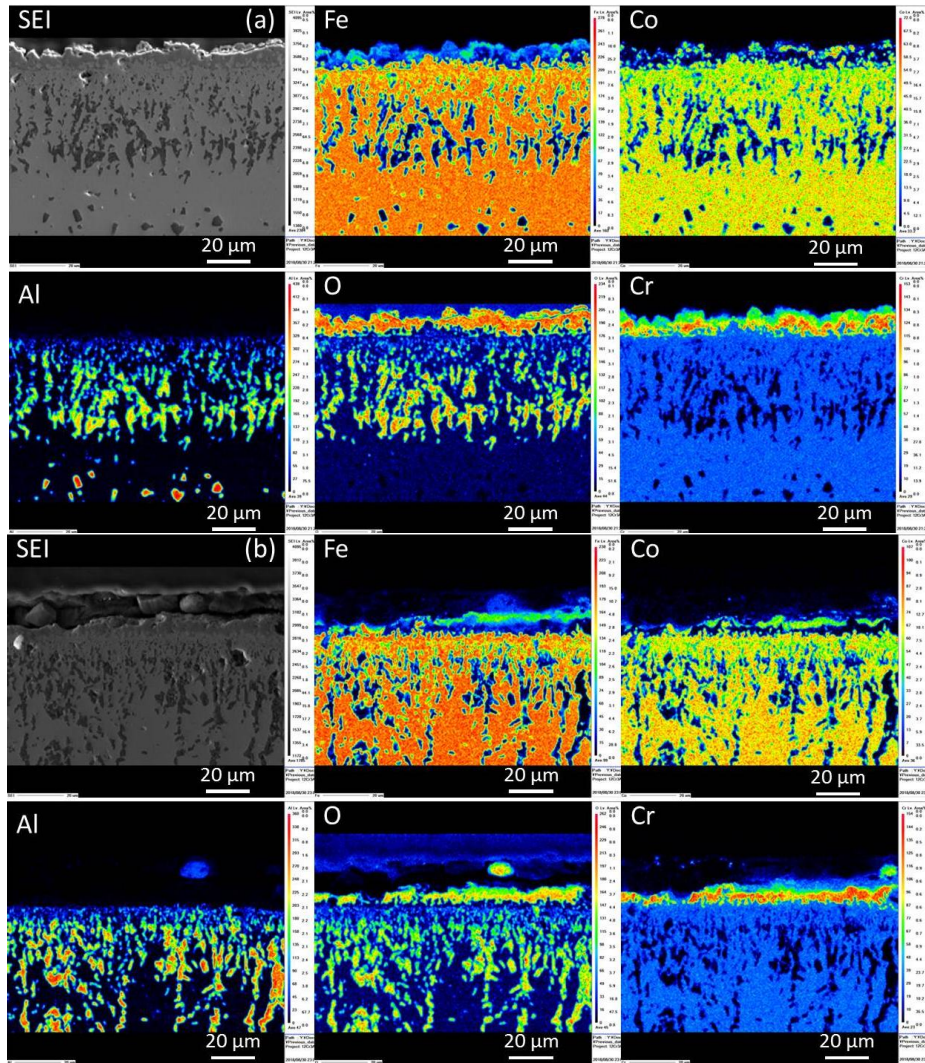


Fig. 4.6 SEI and corresponding EPMA elemental mappings of alloys oxidized at 1000 °C in air for 225 h: a) 3Al15Co alloy, b) 3Al25Co alloy

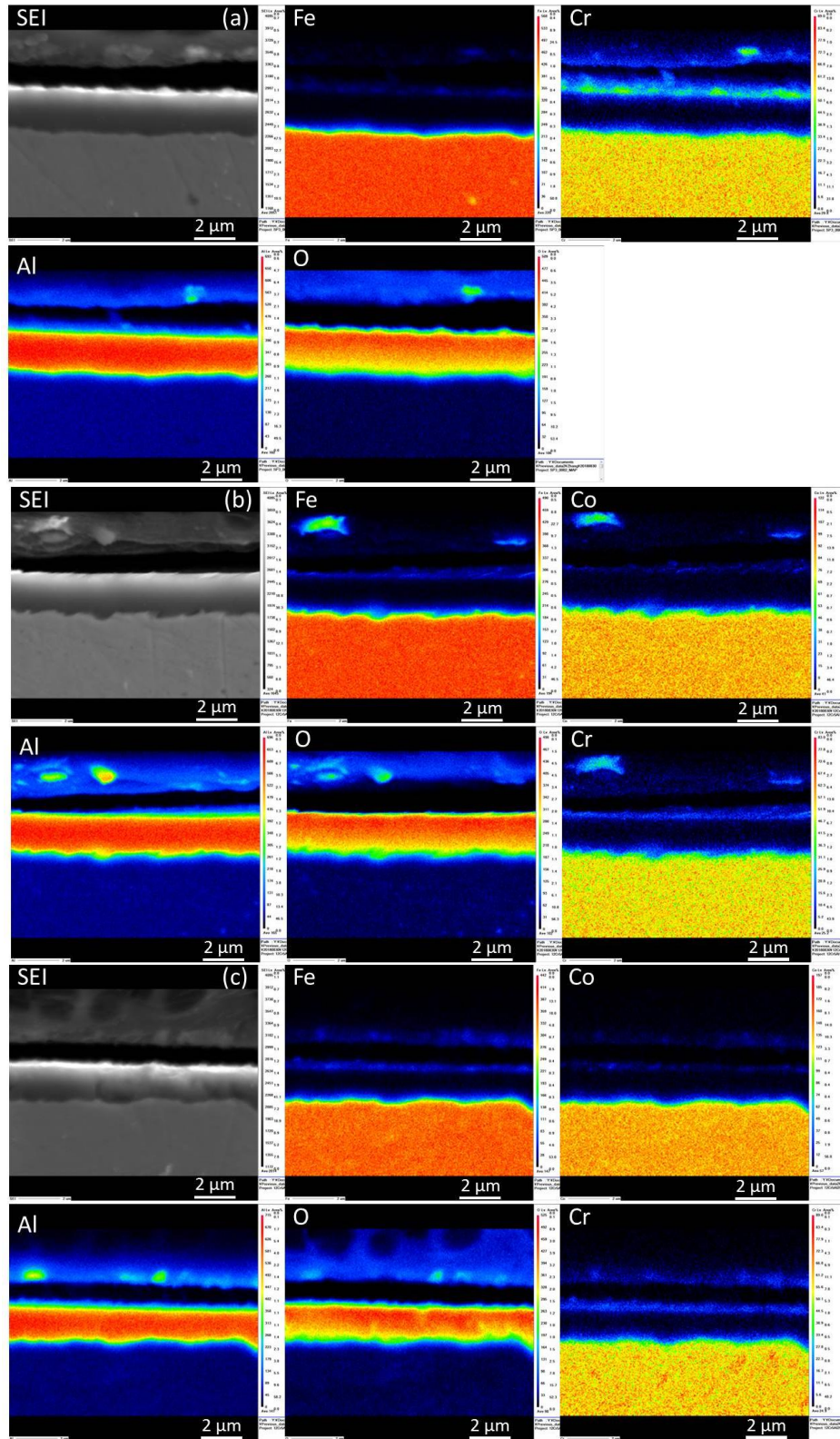


Fig. 4.7 SEI and corresponding EPMA elemental mappings of alloys oxidized at 1000 °C in air for 225 h: a) 12Cr5Al alloy, b) 5Al15Co alloy, c) 5Al25Co alloy

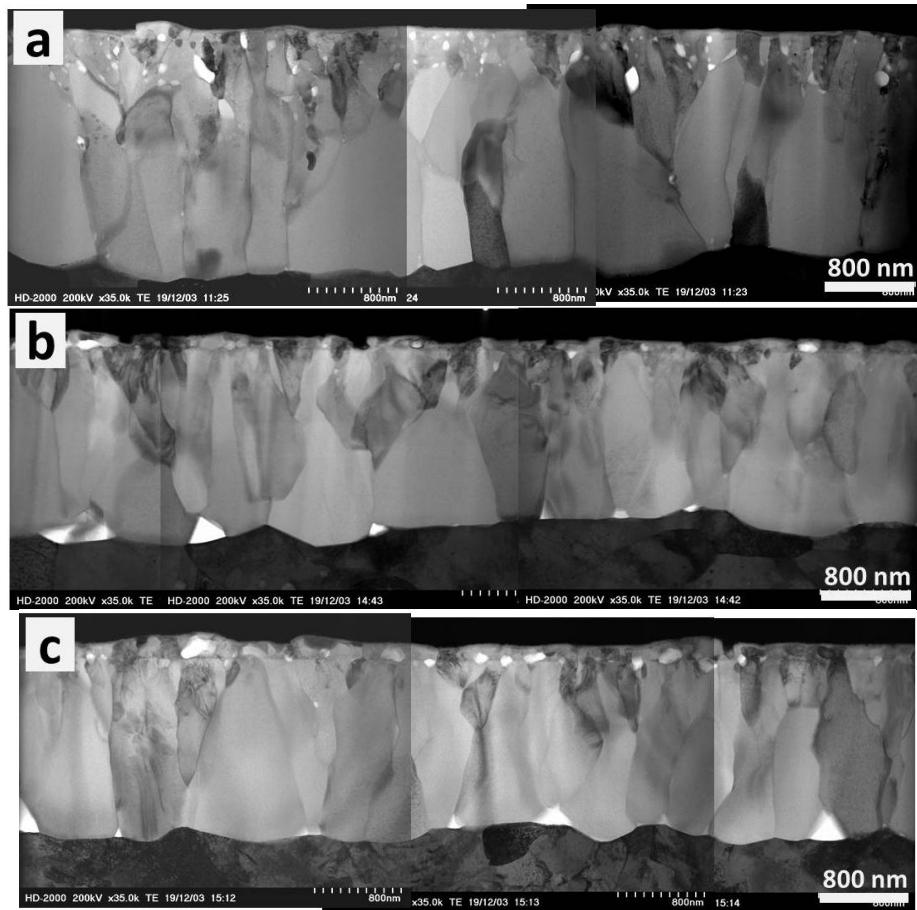


Fig. 4.8 STEM images of scale cross-sections after 225 h oxidation at 1000 °C in air:
a) 12Cr5Al alloy, b) 5Al15Co alloy, c) 5Al25Co alloy

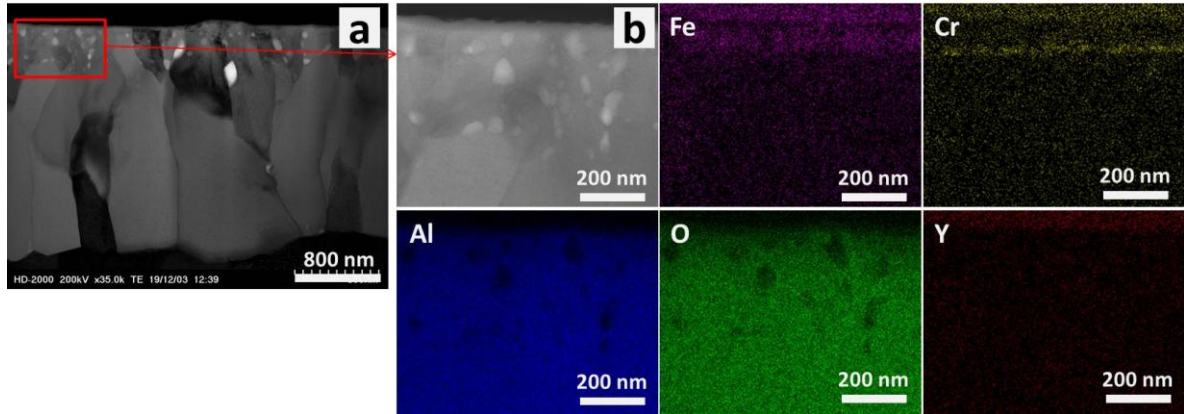


Fig. 4.9 STEM images (a and b) and corresponding STEM elemental mappings of 12Cr5Al alloy oxidized at 1000 °C in air for 225 h

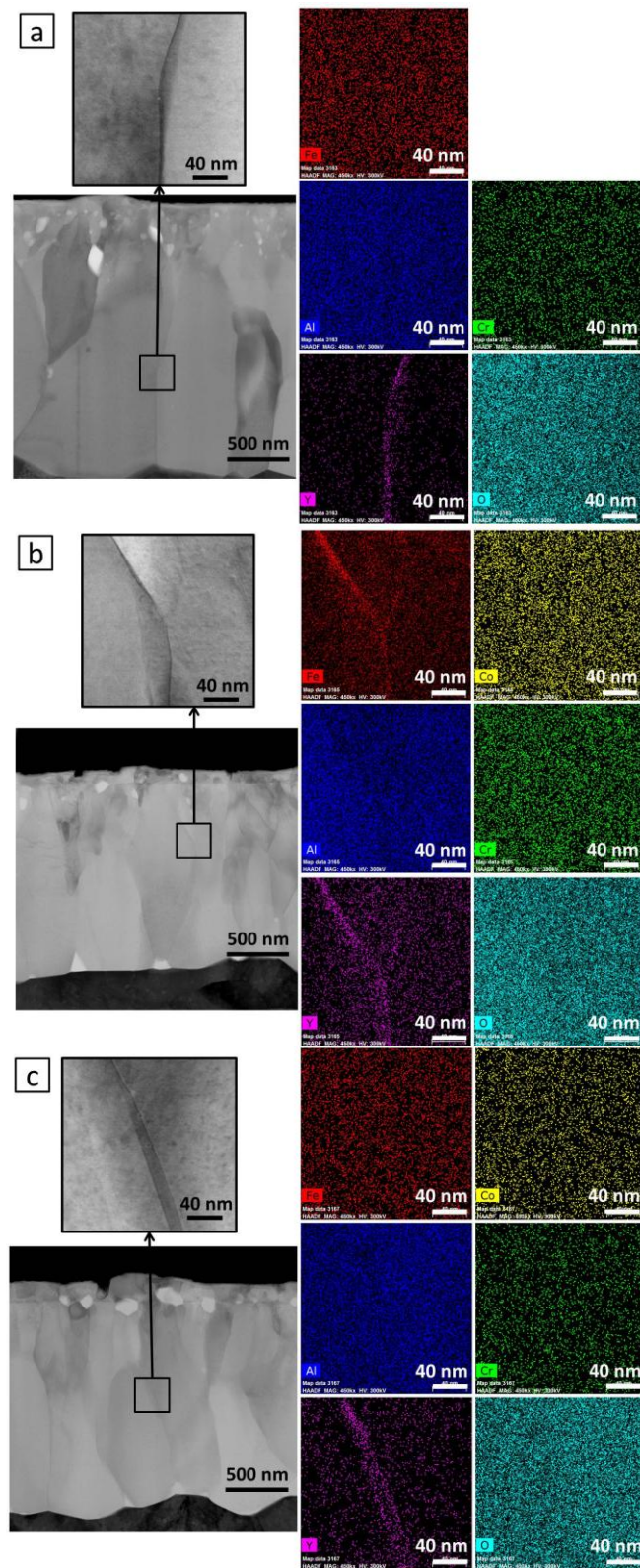


Fig. 4.10 TEM images and corresponding TEM elemental mappings of alloys oxidized at 1000 °C in air for 225 h: a) 12Cr5Al alloy, b) 5Al15Co alloy, c) 5Al25Co alloy

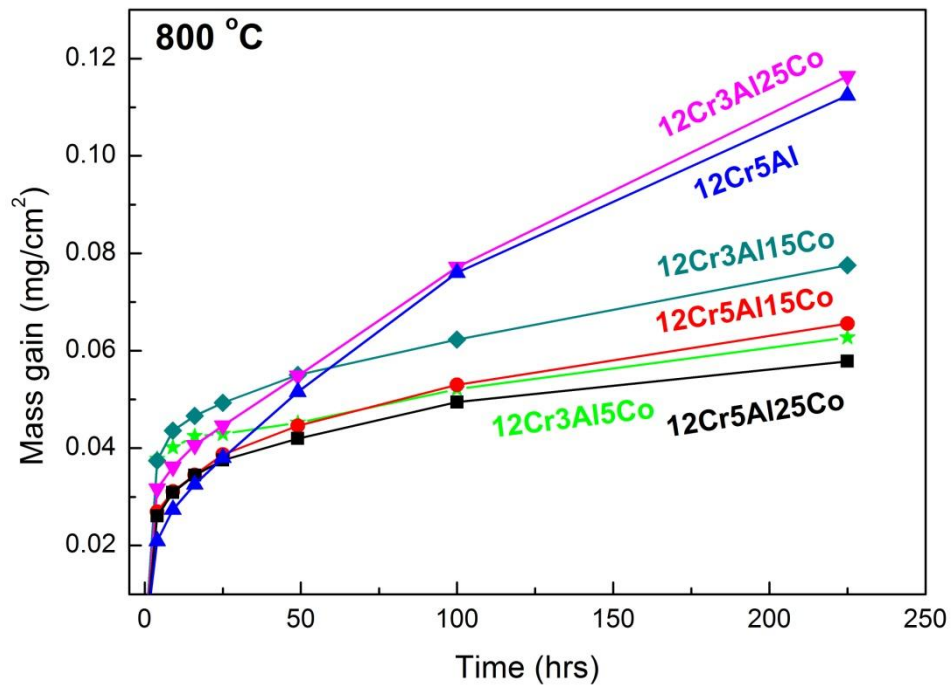


Fig. 4.11 Mass gain of alloys oxidized at 800 °C in air as a function of time

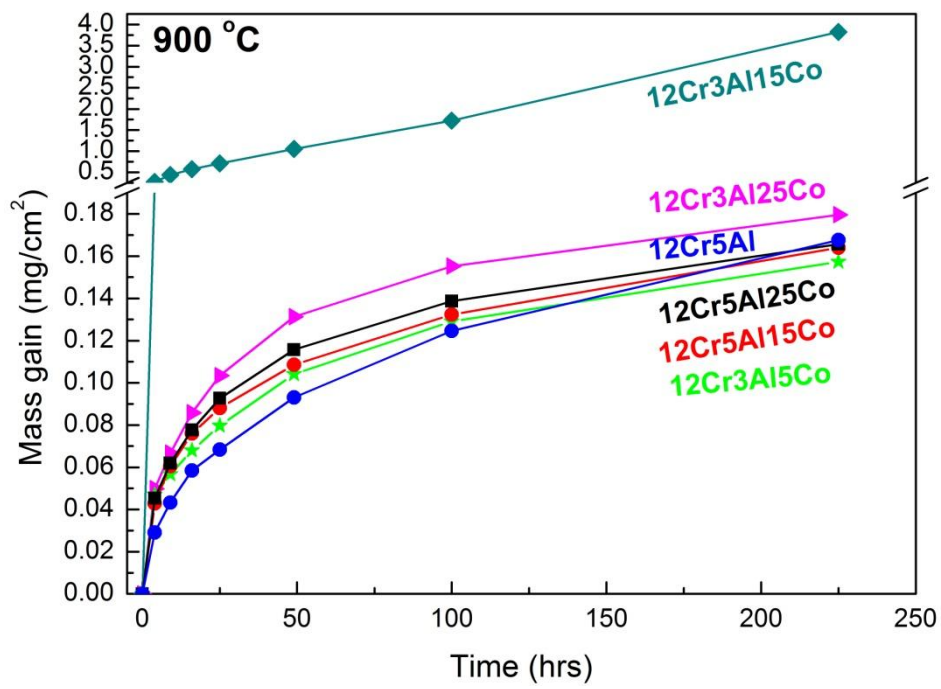


Fig. 4.12 Mass gain of alloys oxidized at 900 °C in air as a function of time

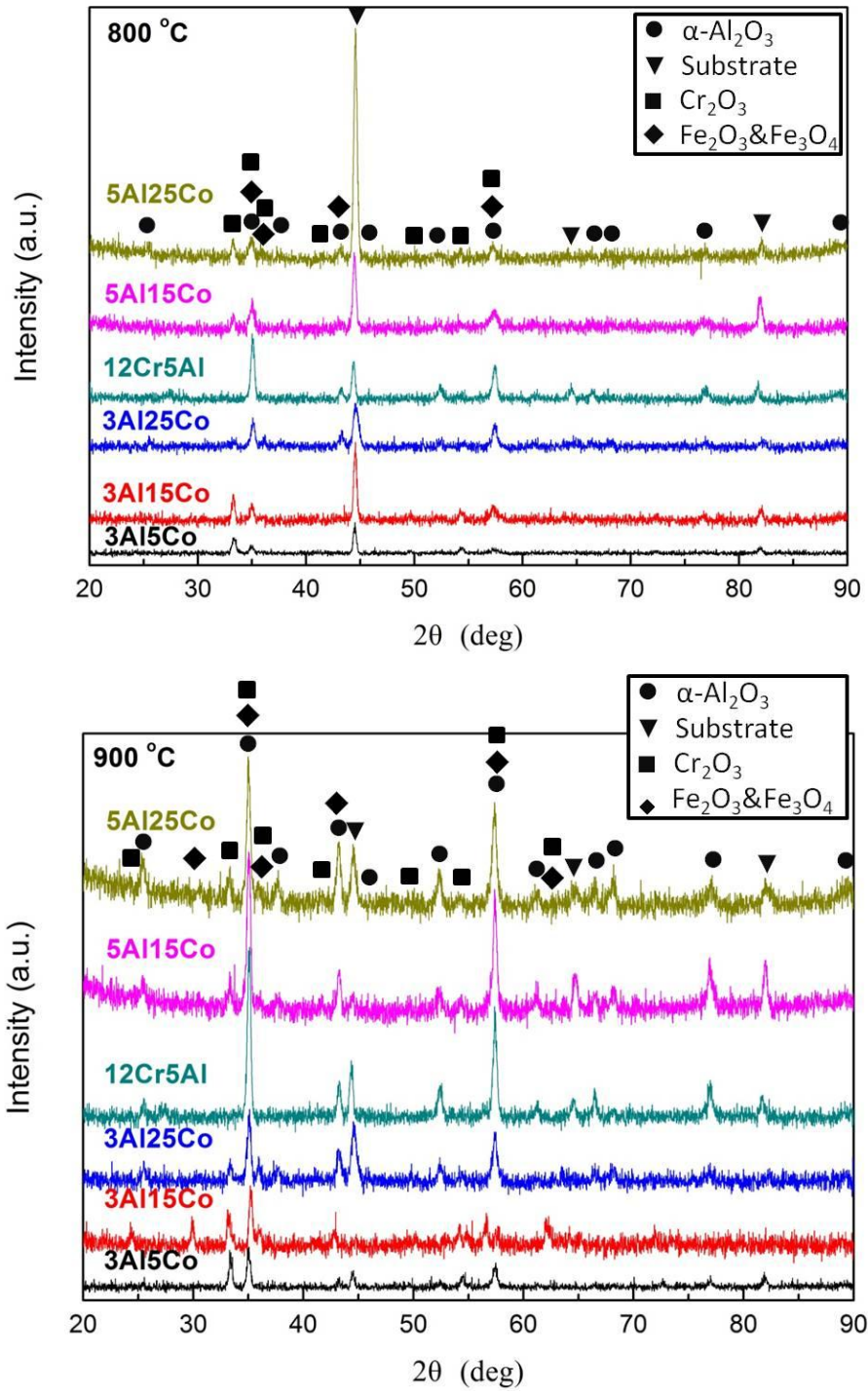


Fig. 4.13 XRD patterns for alloys after 225 h oxidation at 800 °C and 900 °C in air

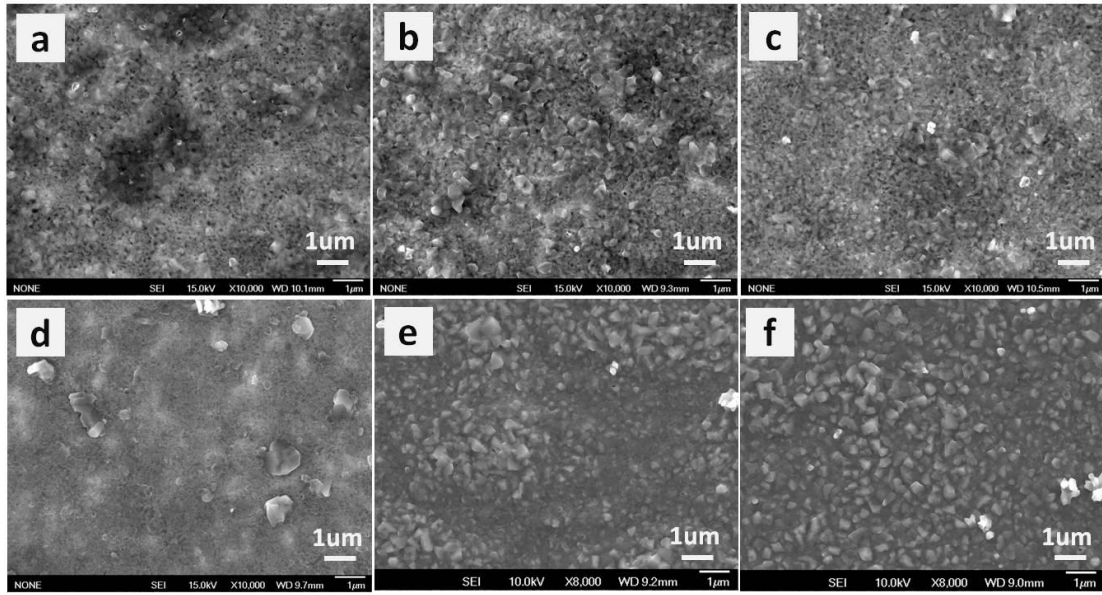


Fig. 4.14 Surface morphologies of alloys after 225 h oxidation at 800 °C in air: a) 3Al5Co alloy, b) 3Al15Co alloy, c) 3Al25Co alloy, d) 12Cr5Al alloy, e) 5Al15Co alloy, f) 5Al25Co alloy

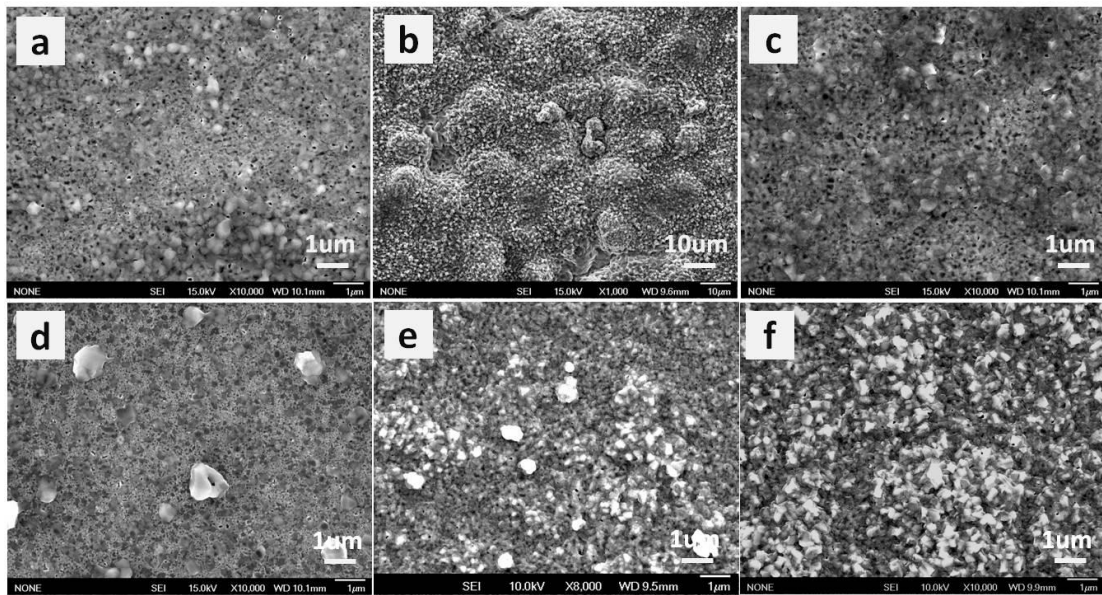
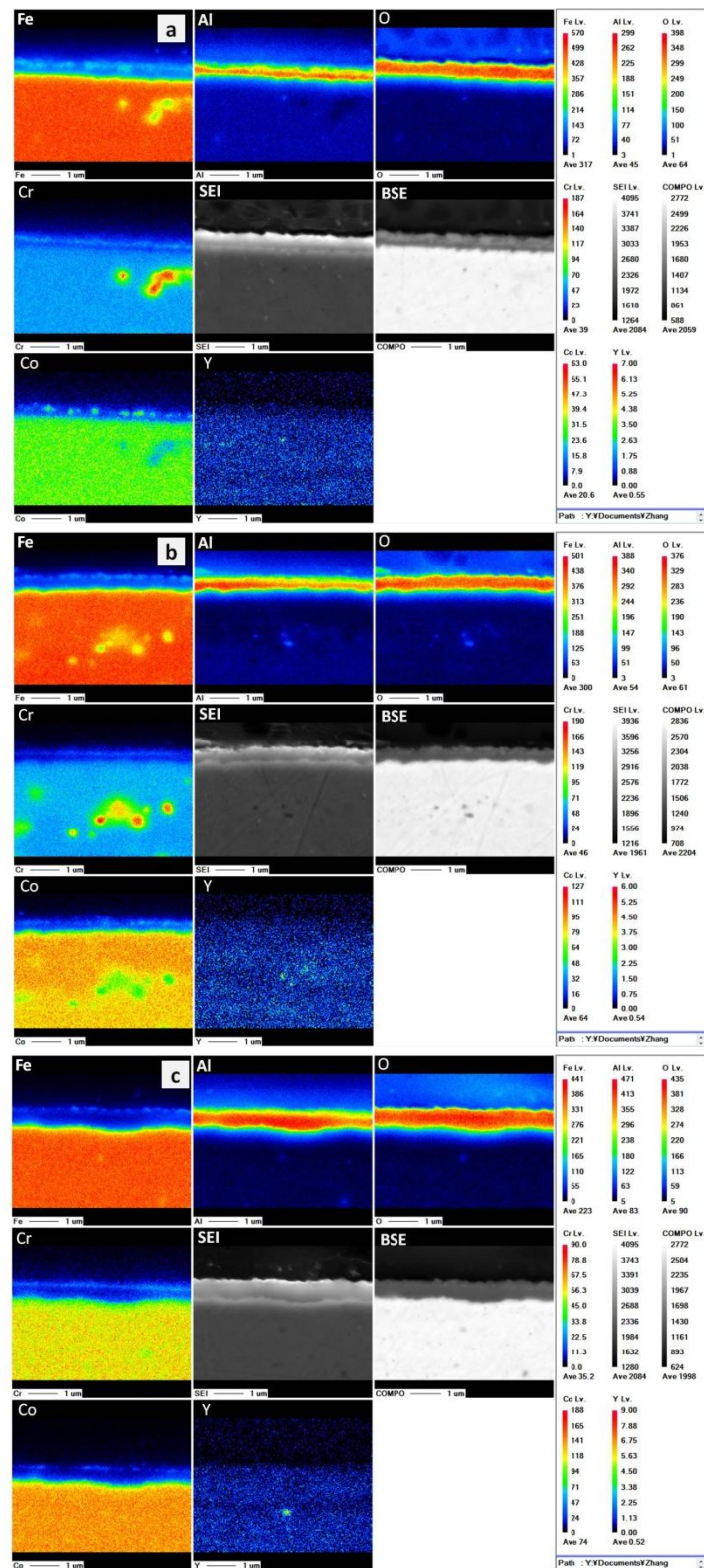


Fig. 4.15 Surface morphologies of alloys after 225 h oxidation at 900 °C in air: a) 3Al5Co alloy, b) 3Al15Co alloy, c) 3Al25Co alloy, d) 12Cr5Al alloy, e) 5Al15Co alloy, f) 5Al25Co alloy



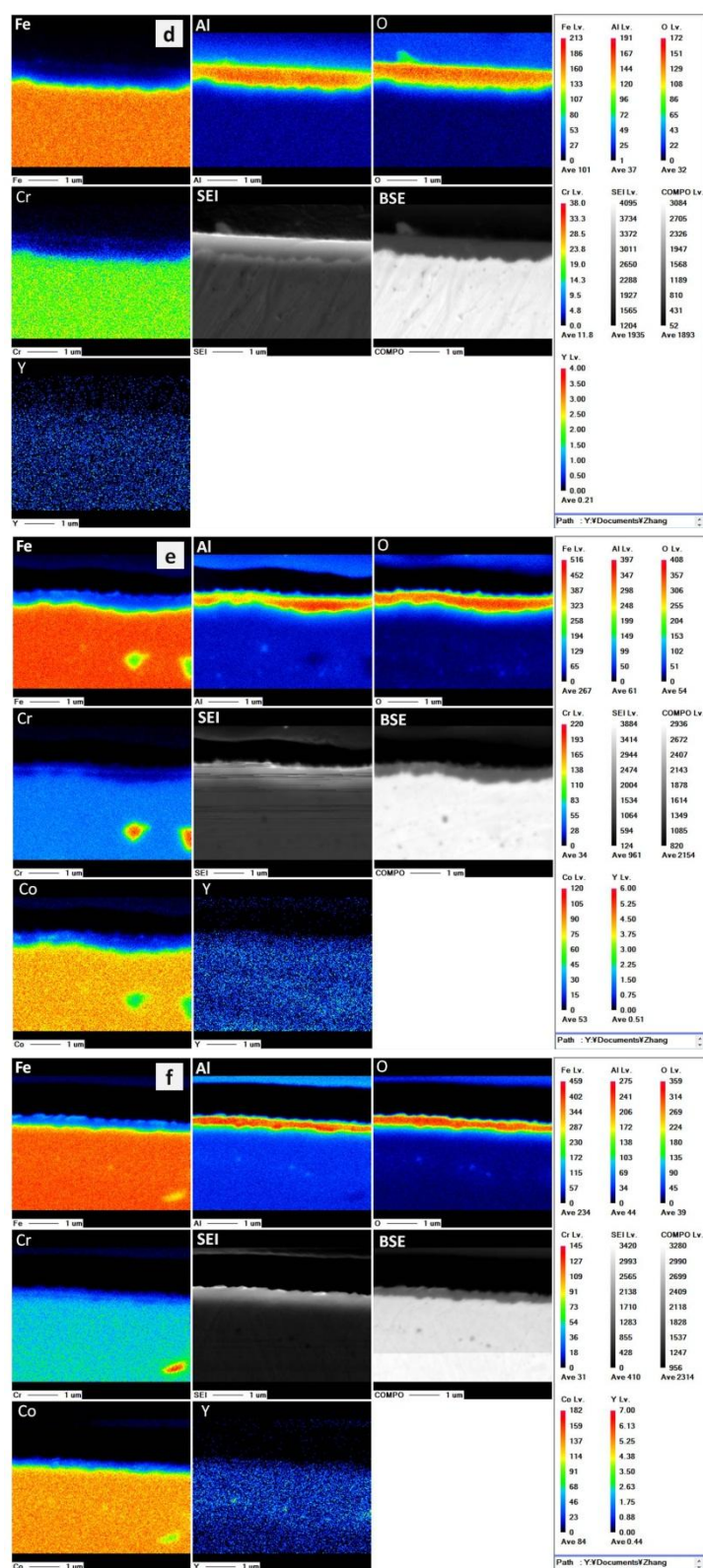
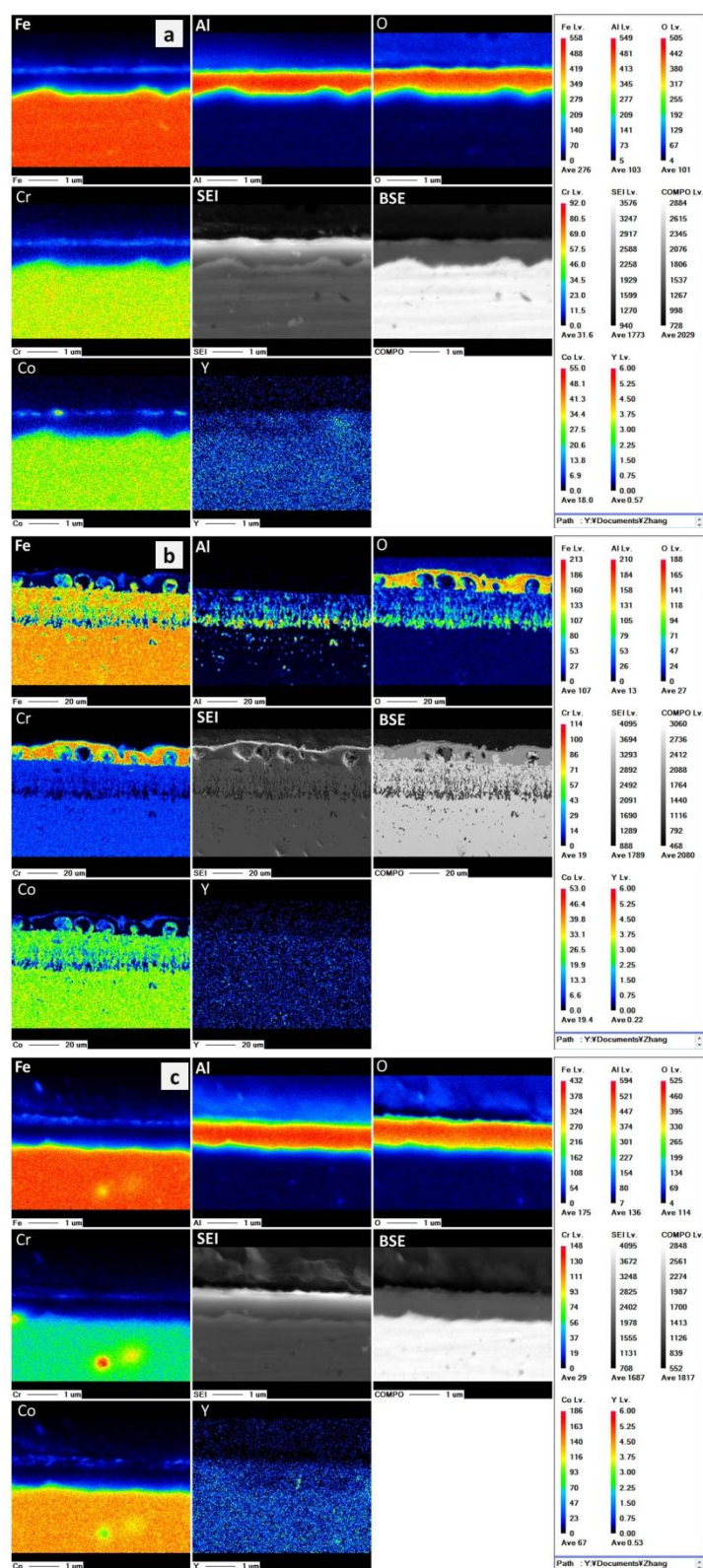


Fig. 4.16 SEI and corresponding EPMA elemental mappings of alloys oxidized at 800 °C in air for 225 h: a) 3Al5Co alloy, b) 3Al15Co alloy, c) 3Al25Co alloy, d) 12Cr5Al alloy, e) 5Al15Co alloy, f) 5Al25Co alloy



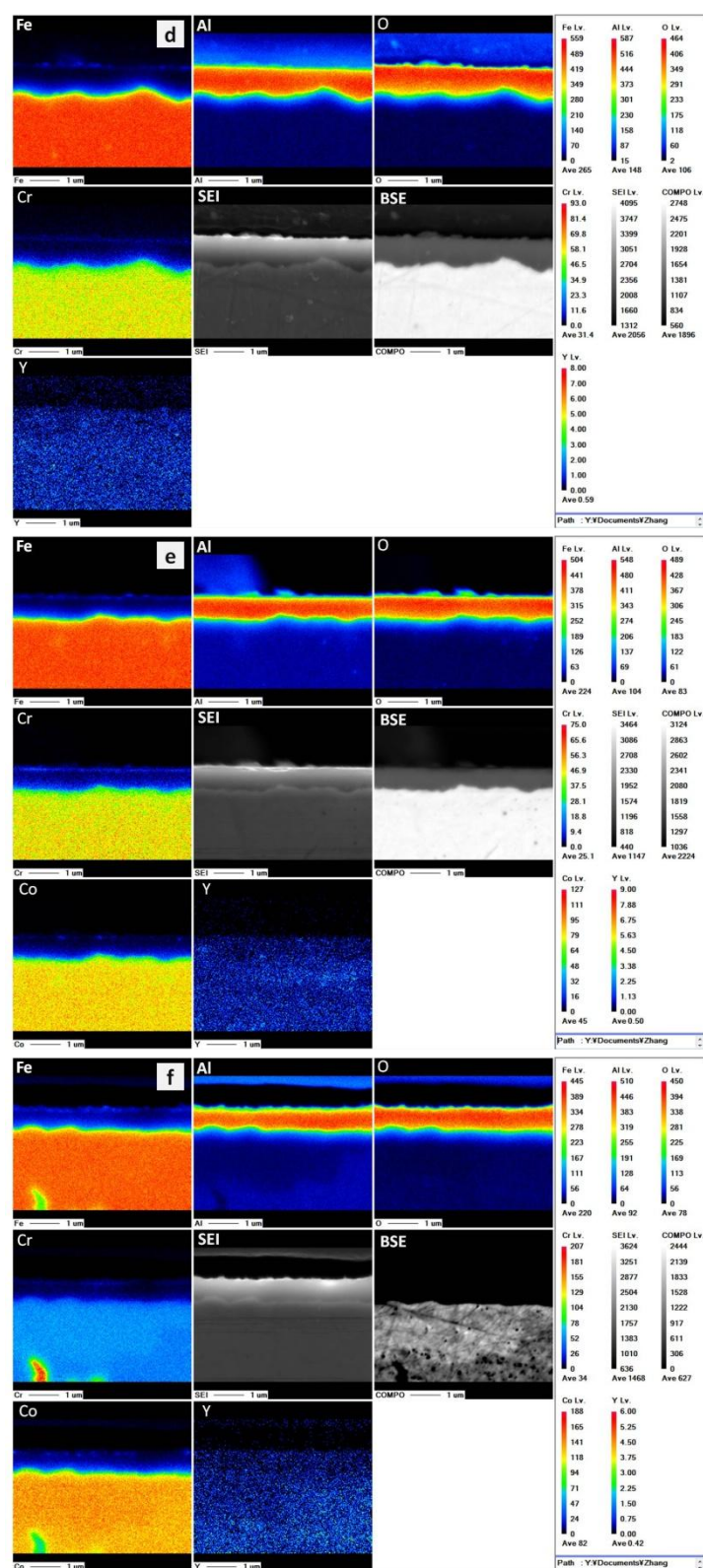


Fig. 4.17 SEI and corresponding EPMA elemental mappings of alloys oxidized at 900 °C in air for 225 h: a) 3Al5Co alloy, b) 3Al15Co alloy, c) 3Al25Co alloy, d) 12Cr5Al alloy, e) 5Al15Co alloy, f) 5Al25Co alloy

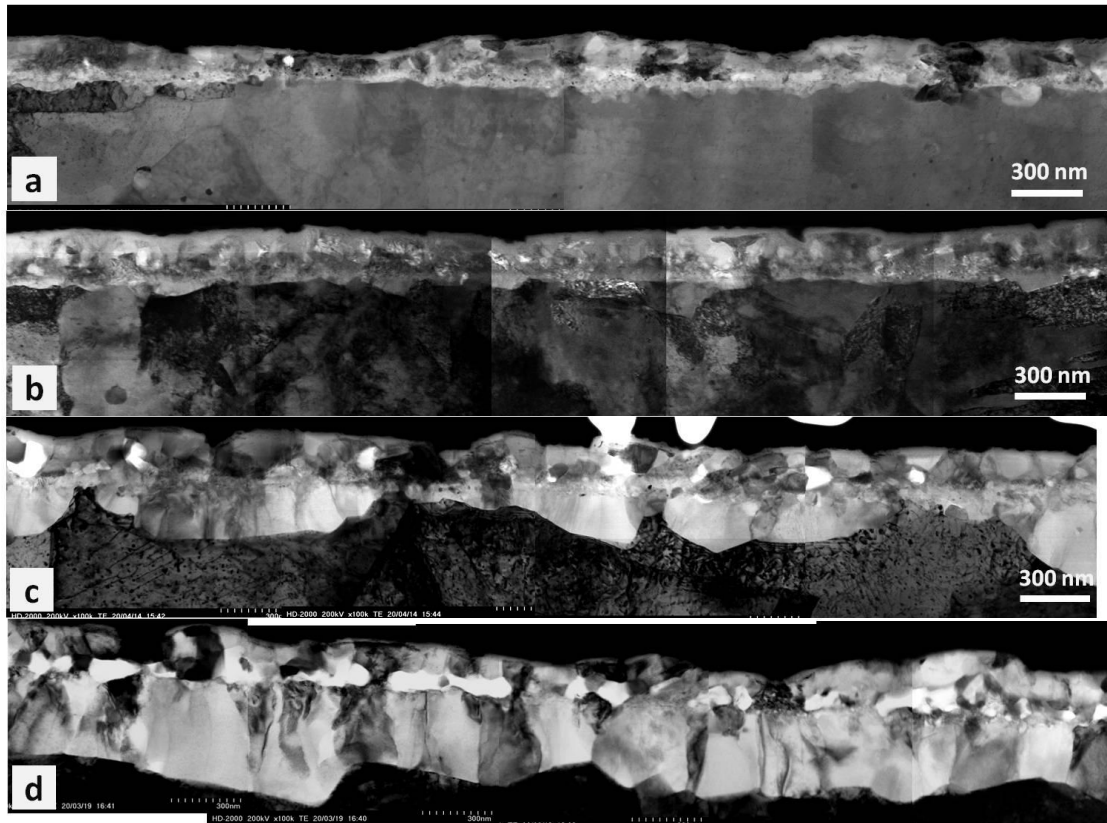


Fig. 4.18 STEM images of scale cross-sections of alloys after 16 h oxidation: a) 3Al5Co alloy, b) 3Al25Co alloy and after 225 h oxidation: c) 3Al5Co alloy, d) 3Al25Co alloy at 800 °C in air

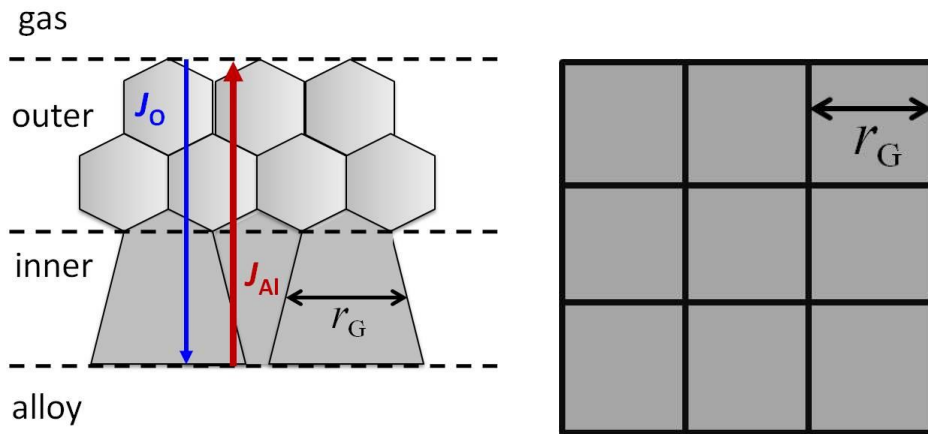


Fig. 4.19 Schematic of cross-section microstructure and top view of oxide scale.

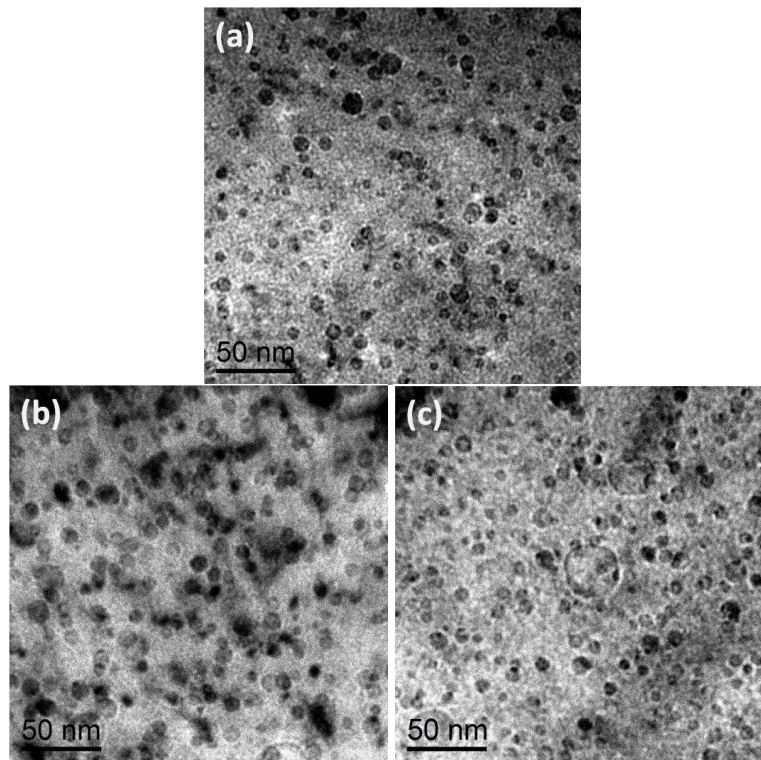


Fig. 4.20 Bright field images of oxide particles in 5Al alloys using TEM: (a) 12Cr5Al, (b) 5Al15Co, (c) 5Al25Co.

CHAPTER 5 Tensile properties of Co-added FeCrAl ODS alloy

5.1 Introduction

For Co-added FeCrAl ODS alloys, the nominal composition Fe–12Cr–5Al–25Co–0.5Y₂O₃ (wt.%) was optimized from the viewpoint of α/γ phase transformation and oxidation resistance as illustrated in the former two chapters. The thermal neutron cross section of the (n, γ) reaction for Co-59 with 100% natural abundance is 37.21 barn (b) from JENDL-4.0, which is much higher than that of the conventional light water reactor material Zr-90 (10.66 mb). Therefore, Co-added FeCrAl ODS alloy cannot be applied to the nuclear field; however, it can be applied for other industries for which high-temperature strength and corrosion and oxidation resistance are required. In this chapter, the tensile properties of the optimized Co-added FeCrAl ODS alloy were investigated, focusing on the oxide dispersion strengthening and order strengthening by B2-type CoAl intermetallic compound at both ambient and elevated temperatures.

5.2 Experimental method

Fe–12Cr–5Al–25Co–0.5Y₂O₃ alloy (FCACO) was fabricated using the following processes. High-purity powders of iron, chromium, cobalt, yttria, and 50Al–50Fe alloy were mixed in a sealed stainless-steel pot and mechanically alloyed (MAed) under argon gas atmosphere. The MAed powders were then consolidated by spark plasma sintering. Using X-ray fluorescence analysis, the chemical composition of the manufactured specimen was measured to be Fe–11.38Cr–4.74Al–22.97Co–0.45Y₂O₃ (wt.%). The sintered specimens were then subjected to hot rolling at 1150 °C with a total thickness reduction of 80%. The final homogenization was performed at 1150 °C for 1 h, and the specimens were then air cooled to room temperature. According to the phase diagram (**Fig. 3.1**) and phase transformation temperature given in **Table 3.4**, the B2-type CoAl precipitate dissolves into the matrix at approximately 800 °C, and ferrite is stable below the A_{C1} temperature of 880 °C; thus, the solution treatment consisted of holding at 850 °C for 1 h followed by quenching in cold water. Aging treatment was conducted at different temperatures (400 °C, 500 °C, 550 °C, and 600 °C) for 100 h to determine the optimal aging treatment.

The Vickers hardness (VH) of each aged sample was obtained using a HMV microhardness tester (SHIMADZU, MCT series) under a load of 0.2 kgf with a dwell time of 15 s, with 5 measurements for each sample. The tensile test was performed at room temperature (RT), 300 °C, and 500 °C at a strain rate of $1 \times 10^{-3} \text{ s}^{-1}$ using a universal material testing machine (SHIMADZU, AG-X-20kN). Miniaturized tensile specimens were prepared with gauge dimensions of 5 mm in length, 1.2 mm in width, and 0.5 mm in thickness using an electro-discharge processing machine. The fracture surfaces of the tensile samples were examined using field-emission scanning electron microscopy (FE-SEM, JEOL JSM-6500F). The distribution of oxide particles and CoAl precipitates in the aged specimens were analyzed using transmission electron microscopy (TEM, 200kV-JEOL JEM-2010 and 300kV-FEI Titan G2), and ~100nm-thick specimens were prepared using focused ion beam milling combined with FE-SEM (FIB-SEM, JEOL JIB-4601F). To study the dislocations in the tensile samples, TEM specimens near the fractures were prepared by FIB-SEM and characterized using the two-beam condition (200 kV) to observe dislocations with different g-vectors. The size of the CoAl precipitates and oxide particles were measured using image processing software (ImageJ 1.48v).

5.3 Results

5.3.1 Distribution of CoAl precipitates and oxide particles

The specimens were solution treated at 850 °C for 1 h and then quenched in cold water, resulting in the dissolution of the CoAl precipitates into the matrix. The average VH with error bars indicating the maximum and minimum are shown in **Fig. 5.1**. The initial hardness is 430 HV, and the evolution of VH is plotted as a function of aging time at 400 °C, 500 °C, 550 °C, and 600 °C. VH sharply increased at the beginning of aging within 20 h; thereafter, the increasing tendency becomes moderate and saturated. The VH of the 600 °C-aging-treated specimen (600-AT) starts to decrease after 20 h, which could be due to CoAl phase coarsening. Consequently, 550 °C and 20 h are the optimal aging temperature and aging time in this work. To confirm this behavior, CoAl precipitates in the 550 °C-20 h-aging-treated specimen (550-20-AT) and 600-100-AT were observed using a Titan transmission electron

microscope (Titan-TEM).

In **Fig. 5.2**, although it is difficult to find a Co or Al concentrated zone to distinguish CoAl precipitates because of the small size and overlap, Cr-depleted zones are apparent because of the CoAl precipitation. In other words, the presence of CoAl precipitates can be confirmed in Cr-depleted zones, and some zones mixed with blue and yellow color in Co–Al dual elemental mappings also correspond to the position of Cr-depleted zones, as observed in the circled zone. The statistics indicate that the average diameter of the CoAl precipitates in 550-20-AT is approximately 7 nm. The concentrated zones in the Co and Al elemental mappings of 600-100-AT in **Fig. 5.3** are more obvious than those in 550-20-AT. The Co and Al concentrated zones are easily noticed and were well mixed in the Co-Al dual elemental mapping. As expected, the average diameter of CoAl precipitates in 600-100-AT was 46 nm, which was much larger than that in 550-20-AT.

The distribution of oxide particles was also examined using TEM, as shown in **Fig. 5.4**. The black spots of smaller size are Y_2O_3 particles, and they are abundantly and uniformly dispersed in the alloys. A few larger particles are also observed, and they are considered to be Y–Al–O ($YAlO_3$ and $Y_3Al_5O_{12}$) complex oxides. The diameters of most of the oxide particles are distributed in the range of 3–9 nm and the average diameter is 6.2 nm according to the measurement in chapter 3.

5.3.2 Structure of CoAl precipitates and ferrite matrix

An inverse pole figure (IPF) map and the corresponding grain boundary map for 550-20-AT are presented in **Fig. 5.5**, implying that the matrix is ferrite with a body-centered cubic (bcc) structure in an average grain size (GS) of 1.60 μm transformed from austenite during air cooling. The electron diffraction patterns of the ferrite matrix and precipitates are presented in **Fig. 5.6**. The lattice constants were derived from analysis of the diffraction patterns. The calculated lattice constant of the ordered B2 phase, a_{B2} , and matrix, a_{bcc} , are summarized in **Table 5.1**. These constants, a_{B2} and a_{bcc} , are only 0.1-Å higher than those reported in the literature [111, 112], which could be caused by the error from TEM observation. The misfit strain between the matrix and ordered B2 phase was calculated using the formula of $\delta = 2 \times (a_{B2} - a_{bcc}) / (a_{B2} + a_{bcc})$. The calculated value of δ is also shown in **Table 5.1**. The

misfit strain between the B2-type precipitates and ferrite matrix is only 0.24%, implying that coherency is extremely high and that it is important to consider the strengthening mechanism by B2-type precipitates.

5.3.3 Tensile properties

Fig. 5.7 presents the stress–strain (S–S) curves of 550-20-AT at RT, 300 °C, and 500 °C. The tensile tests were conducted two times at each temperature. The yield strength (YS) and ultimate tensile strength (UTS) at room temperature are approximately 1600 MPa and decrease with increasing testing temperature. The uniform elongation (UE) and total elongation (TE) were also measured; the total elongation clearly increases with increasing temperature. The average values of the tensile data at different temperatures are summarized in **Table 5.2**.

Fig. 5.8 shows the fracture surfaces of the tensile specimens at RT, 300 °C, and 500 °C. Numerous river patterns are observed in the RT specimen, which is the typical fracture mode exhibited in transgranular fracture. The formation of these river patterns is a result of a cleavage crack crossing a twist boundary between grains. Upon increasing the temperature to 300 °C, the number of river patterns decreases, whereas that of cracks on the fracture surface increases. The specimen tested at 500 °C exhibits a cup-and-cone fracture surface and numerous spherical “dimples” are clearly observed when it was examined at higher magnification. Each dimple is one half of a microvoid that formed and then separated during the fracture process. Generally, the ductile alloy presents a cup-and-cone fracture surface, which shows agreement with the ductility increase for 500 °C tensile specimen.

5.3.4 Anisotropic properties

In order to confirm the effect of phase transformation on anisotropic properties, the alloy with nominal chemical composition Fe-12Cr-5Al-0.5Y₂O₃ (12Cr5Al-ODS) was fabricated. **Table 5.3** shows the tensile properties of 12Cr5Al-ODS and FCACO alloy tested in rolling direction (RD) and transverse direction (TD) direction at room temperatures. The total elongation of 12Cr5Al alloy was higher than that of FCACO alloy, which implied that the former one had better ductility. However, the differences of total elongations (3%) and UTS (90 MPa) at two different directions of 12Cr5Al

alloy are higher than those of FCACO alloy, which demonstrated that 12Cr5Al alloy was more anisotropic than FCACO alloy. The IPF map in **Fig. 5.5** showed that the grains in FCACO alloy after phase transformation from γ to α were equiaxial, which can be an interpretation for the better isotropic properties of FCACO alloy.

5.4 Discussion

5.4.1 Oxide particle strengthening and B2-type order strengthening

One of the strengthening factors in Co-added FeCrAl-ODS alloy comes from the dispersed oxide particles shown in **Fig. 5.6**. The oxide particles interact with the moving dislocations via the Orowan mechanism [113]. σ_o is the threshold stress and corresponds to the oxide-particle hardening stress, which is expressed in terms of the critical resolved shear stress (CRSS), τ_o , by the Orowan mechanism and the Taylor factor, M , 3.06.

$$\sigma_o = M \times \tau_o \quad (5.1)$$

$$\tau_o = A \frac{1}{2\pi} \frac{Gb}{\lambda} \left(\ln \frac{D}{r_o} + B_0 \right) \quad (5.2)$$

$$\lambda = 1.25l_s - 2r_s \quad (5.3)$$

$$l_s = \sqrt{\frac{2\pi r^3}{3f}} \quad (5.4)$$

$$r_s = \frac{\pi \overline{r^2}}{4f} \quad (5.5)$$

where G is the shear modulus of the matrix (78.0 GPa at RT, 71.1 GPa at 300 °C, and 64.3 GPa at 500 °C) [98]; b is the magnitude of the Burgers vector (2.48×10^{-10} m); λ is the average face-to-face distance between two particles; r_o is the inner cut-off radius of a dislocation core, which is taken to range from b to $3b$; D is the harmonic mean of λ and $2r_s$; \bar{r} is the average oxide particle radius obtained from TEM micrographs (**Fig. 5.4**); and $\overline{r^2}$ and $\overline{r^3}$ are the averages of r^2 and r^3 , respectively. r_s is the equivalent average particle radius and l_s is the average center to center distance. The volume fraction, f , of the oxide particles was evaluated using TEM bright field images. For a screw dislocation, B_0 is 0.6, and A is a constant given by the following equations [113, 114]:

$$A = 1/(1 - \nu) \quad (5.6)$$

$$\nu = 4.46 \times 10^{-5}T + 0.27 \quad (5.7)$$

Here, ν is Poisson's ratio and T is temperature expressed in $^{\circ}\text{C}$. The detailed parameters for the calculation are listed in **Table 5.4**, and the oxide-particle hardening stress, σ_o , values estimated using the above parameters are summarized in **Table 5.5**, where the range of σ_o is attributed to uncertainty of the cut-off radius of a dislocation core ranging from b to $3b$.

The increase of the VH after aging at 550°C for 20 h resulting from B2-type CoAl precipitates can be approximately converted into the increase of the ultimate tensile strength (ΔUTS) using the following empirical relationship [115]:

$$\Delta \text{UTS}(\text{MPa}) = \Delta H\nu(\text{MPa})/3 \quad (5.8)$$

Here, $\Delta H\nu$ was measured to be 1274 MPa (130 kgf/mm²) from **Fig. 5.1**, which corresponds to 425 MPa for ΔUTS . As shown in **Table 5.1**, the B2-type CoAl particles are an ordered phase and maintain excellent coherency with the matrix. When dislocations shear precipitates, the possible strengthening mechanisms that are generally considered are coherency strengthening, modulus mismatch strengthening, and order strengthening. For CoAl precipitates with the B2-type ordered phase maintaining excellent coherency with the matrix, Yasuda et al. confirmed that the dominant strengthening mechanism is order strengthening [116]. B2-type ordered particles are sheared by moving dislocations, and the CRSS for the order strengthening is expressed by the following equation [117]:

$$\tau_{\text{order}}(1) = \frac{\gamma_{\text{APB}}}{2b} \left[\left(\frac{\gamma_{\text{APB}} r f}{T} \right)^{\frac{1}{2}} - f \right] \quad (5.9)$$

In addition, Ardell [118] modified the above equation as follows:

$$\tau_{\text{order}}(2) = \frac{\gamma_{\text{APB}} u}{2b} \quad (5.10)$$

$$u = \frac{(4B+B^2/3)^2 - B}{2(1-B/6)} \quad (5.11)$$

$$B = \frac{3\pi^2 \gamma_{\text{APB}} f r}{32T} \quad (5.12)$$

where γ_{APB} is the anti-phase boundary (APB) energy per unit area, taken as 750 MJ/m², and T is the line tension of a dislocation, approximately equal to $Gb^2/2$, where the values of G are same as those mentioned above. The volume fraction f of precipitates and the average precipitate radius r were determined from TEM images using quantitative stereology. These values are listed in **Table 5.4**. The order strengthening

stress σ_{order} is obtained by multiplying by the Taylor factor M (3.06) and the constant α for the CRSS:

$$\sigma_{\text{order}} = \alpha \times M \times \tau_{\text{order}} \quad (5.13)$$

τ_{order} (1) was estimated to be 369 MPa according to Eq. (5.9), and τ_{order} (2) was calculated to be 442 MPa using Eq. (5.10); σ_{order} for RT was 425 MPa (ΔUTS); thus α (1) and α (2) were calculated to be 0.38 and 0.31 respectively. Then, the value of σ_{order} for 300 °C and 500 °C were derived. **Table 5.5** presents the calculation results for the order strengthening σ_{order} (1) and σ_{order} (2) together with those of the oxide dispersion strengthening σ_o .

The temperature dependencies of the order strengthening and oxide dispersion strengthening are schematically illustrated in **Fig. 5.9**. The YS results shown as black squares and connected with solid black lines are the experimental tensile test results at RT, 300 °C, and 500 °C; the oxide dispersion strengthening σ_o and order strengthening σ_{order} , calculated using Eq. (5.1) and Eq. (5.13), are indicated by the bars in cyan and yellow, respectively. Yamamoto et al. [119] reported the tensile properties of FeCrAl alloys without Y_2O_3 addition (FCA alloy) from RT to 550 °C. The YS data at RT, 300 °C, and 500 °C from that study are presented with triangles and connected with dashed blue lines in **Fig. 5.9**. Massey et al. [120] studied the tensile properties of FeCrAl ODS alloys (FCAO alloys) from RT to 800 °C with similar chemical composition and grain size as specimen in the present study. Their YS results are indicated by circles and dashed red lines in **Fig. 5.9**. The differences in YS between the FCA and FCAO alloys are attributed to the oxide dispersion strengthening σ_o , which is consistent with the values of strengthening stress estimated using Eq. (5.1) and shown in **Table 5.5**. Furthermore, the order strengthening σ_{order} by B2-type CoAl precipitates resulted in the difference in YS between the FCACO alloy and FCAO alloys, as there is no Co addition in FCAO alloys. This YS difference agrees well with the values of strengthening stress estimated using Eq. (5.13) and shown in **Table 5.5** at RT and 300 °C. When the temperature increased to 500 °C, however, this consistency breaks down; the order strengthening σ_{order} by B2-type CoAl precipitates appeared to be significantly reduced as it is compared with the stress estimated using Eq. (5.13), as shown in **Fig. 5.9**, where the calculation result for the order strengthening σ_{order} at 500 °C is indicated by the hollow yellow bar.

5.4.2 B2-type order strengthening at 500 °C

In the followings, the reduction of the ordered stress σ_{order} by B2-type CoAl precipitates at 500 °C is considered. It is known that the favorable slip system of bcc metals is $\{110\} \langle 111 \rangle$, whereas the primary slip system of B2-type CoAl precipitate is $\{010\} \langle 001 \rangle [121]$. The activation of $\langle 111 \rangle$ slip in the CoAl precipitate is extremely difficult. Therefore, when $a/2 \langle 111 \rangle$ dislocations in the bcc matrix pass through the CoAl B2 precipitates, the precipitates strongly suppress the dislocation motion, which is considered an origin of the order strengthening. Concerning $\langle 111 \rangle$ and $\langle 001 \rangle$ slip in bcc metals, Takeuchi [122] and Chin [123] reported that the CRSS for $\langle 001 \rangle$ slip is at least $\sqrt{3}$ times higher than that for $\langle 111 \rangle$ slip. Yasuda et al. [116] conducted compression tests on FeAlCo single crystals containing B2-type CoAl precipitates in various directions, and the Schmid factors for the $\langle 111 \rangle$ and $\langle 001 \rangle$ slip systems also changed with different loading directions. They stated that $\{010\} \langle 001 \rangle$ slip can be induced by CoAl precipitates in a bcc matrix because the Schmid factors of $\langle 001 \rangle$ slip are higher than those of $\langle 111 \rangle$ slip in some loading directions. Intermediate slip planes with $\langle 001 \rangle$ direction can also be thermally activated upon increasing the temperature to 450 °C–550 °C, because their CRSS decreases more rapidly than that of typical $\{010\} \langle 001 \rangle$ slip at those temperatures [116]. The $\langle 001 \rangle$ slip in the bcc matrix weakens the B2-type ordered strengthening because of the parallel slip with the CoAl-B2 phase.

The dislocation Burgers vectors in tensile specimens tested at 500 °C were then characterized by TEM to verify the possibility for $\langle 001 \rangle$ slip in the ferrite matrix. Bright-field TEM (BF-TEM) images of the tensile specimen tested at 500 °C are shown in **Fig. 5.10**, where four different g -vectors, $[110]$, $[1\bar{1}0]$, $[020]$, and $[200]$ near the $[001]$ zone axis were selected. Based on the visibility criteria ($|\vec{g} \cdot \vec{b}|$ values) given in **Table 5.6**, all the dislocations with the Burgers vectors of $\frac{a}{2} \langle 111 \rangle$ and $a \langle 100 \rangle$ were analyzed. Further analysis of the four figures indicates that the dislocations of the Burgers vectors of $a[100]$, $a[010]$, and $\frac{a}{2} \langle 111 \rangle$ can be identified as indicated by the red, yellow, and blue arrows, respectively. In the top right area, a dislocation with a $[100]$ Burgers vector shows clear contrast in all the figures except for that with the

[020] g-vector. Two dislocations with $\frac{a}{2}\langle 111 \rangle$ Burgers vectors located in the area below it are invisible in the figures with the [110] g-vector and $[1\bar{1}0]$ g-vector individually. In the lower part of the figures, a dislocation possessing a [010] Burgers vector showed weak contrast in the figure with the [200] g-vector.

More than 200 dislocations were individually characterized for the tensile specimens tested at RT and 500 °C. The statistical results indicate that $\langle 001 \rangle$ -type dislocations in the tensile specimens tested at RT accounted for approximately 6% of the dislocations, which is in good agreement with the result reported in the reference [124]; however, those in tensile specimens tested at 500 °C accounted for 13% of the dislocations, which is more than twice those in the RT tensile specimen. Therefore, it is worth noting that at approximately 500 °C, thermally activated $\langle 001 \rangle$ slip in the bcc ferrite can provide weak interaction with B2-type CoAl precipitates containing the same $\langle 001 \rangle$ slip. This situation is considered to be an origin of the decrease of the order strengthening at 500 °C.

5.4.3 Superposition consideration

Once the increment of strength due to each mechanism was assessed, it was necessary to consider how these strengthening increments should be superimposed. Several relationships have been proposed to account for the contributions to the YS of distinct obstacles of two or more strengths, most of which assume the general form [125]:

$$\sigma_{\text{total}}^k = \sum_i \Delta\sigma_i^k \quad (5.14)$$

where k is an adjustable parameter which can be taken as 1 for linear superposition or 2 for Pythagorean superposition, or any value in between. i means each precipitate strengthening mechanism.

Here, the YS of FCA alloy is taken as the strength of matrix σ_m because the concentration of Fe, Cr and Al is similar. As shown in **Table 5.7**, the oxide dispersion strengthening and order strengthening can be linearly add at RT to meet the experimental result. As discussed above, the order strengthening by CoAl precipitates failed at 500 °C such that the YS can be obtained by the summation of the matrix strength and oxide dispersion strengthening. Whereas, the value of k is estimated to be 1.2 to meet the experiment result at 300 °C, which implies that the interaction

between dislocations and two types of obstacles (CoAl precipitates and oxide particles) can be variable at different temperature.

5.5 Conclusion

The hardness and tensile properties of Co-added FeCrAl ODS alloy containing oxide particles and B2-type CoAl precipitates were evaluated, focusing on the oxide particle dispersion strengthening and CoAl order strengthening at both ambient and elevated temperatures. The aging treatment condition for Fe–12Cr–5Al–25Co–0.5Y₂O₃ alloy is 20 h and 550 °C to optimize the formation of CoAl B2-type precipitates. The contributions of ODS and CoAl order strengthening were calculated, and the results reasonably agreed with the experimental results at RT and 300 °C. It was found, however, that the tensile strength contributed by the CoAl ordered precipitate was completely reduced at 500 °C. Through characterization of the dislocation Burgers vector in the specimens tested at RT and 500 °C, the abundance frequency of $\langle 001 \rangle$ -type dislocations in the ferrite matrix was 13% in the 500 °C tensile specimens, which is more than twice that in the RT tensile specimens. Considering that the slip system of the B2-type CoAl phase is $\{010\}\langle 001 \rangle$, the significant reduction of the order strengthening σ_{order} at 500 °C is attributed to the thermally activated $\langle 001 \rangle$ slip in the ferrite matrix, which provides weak interaction with B2-type CoAl precipitates with the same $\langle 001 \rangle$ slip.

Table 5.1 Lattice constants and misfit strain between B2 phase and matrix of 550-20-AT.

Sample ID	$a_{B2} / \text{\AA}$	$a_{BCC} / \text{\AA}$	$\delta / \%$
FCACO	2.959	2.952	0.24

Table 5.2 Average values of tensile properties tested at different temperatures.

Sample ID	YS/ MPa	UTS/ MPa	UE/ %	TE/ %
RT	1583	1642	2.3	2.3
300 °C	1329	1477	5.5	5.5
500 °C	667	703	0.7	6.6

Table 5.3 Tensile properties of 12Cr5Al and FCACO alloys tested in RD and TD direction at room temperatures.

Sample ID	YS/ MPa	UTS/ MPa	UE/ %	TE/ %
FCACO-RD	1583	1642	2.3	2.3
FCACO-TD	1550	1583	0.5	0.5
12Cr5Al-RD	960	1131	8.7	14.5
12Cr5Al-TD	890	1041	6.6	11.6

Table 5.4 Detailed parameters for calculations.

Sample ID	r_o / nm	\bar{r} / nm	$\overline{r^2} / \text{nm}^2$	$\overline{r^3} / \text{nm}^3$	r_s / nm	l_s / nm	$f / \%$	λ / nm	D / nm	r / nm	B	u
Oxide particles	0.25~0.75	3.1	9.8	32.7	2.5	54	0.53	63	5	-	-	-
CoAl	-	-	-	-	-	-	11.4	-	-	3.6	0.11	0.29

Table 5.5 Calculation of strengthening stress from oxide particles and CoAl precipitates.

	RT	300 °C	500 °C
Measured UTS (MPa)	1642	1477	703
σ_o oxide dispersion strengthening (MPa)	415 ~ 603	386 ~ 560	353 ~ 512
$\sigma_{\text{order}(1)}$ ordered strengthening (MPa)	425	454	488
$\sigma_{\text{order}(2)}$ ordered strengthening (MPa)	425	442	461

Table 5.6 Visibility analysis of dislocations with different g-vectors near to [001] zone axis in tensile specimens. (● and ○ indicate that the dislocation is visible and invisible respectively)

$g \backslash b$	$b(\times a)$					
	[100]	[010]	$1/2[111]$	$1/2[\bar{1}11]$	$1/2[1\bar{1}1]$	$1/2[11\bar{1}]$
[110]	●	●	●	○	○	●
[1-10]	●	●	○	●	●	○
[020]	○	●	●	●	●	●
[200]	●	○	●	●	●	●

Table 5.7 Superposition results using different values of k .

	RT	300 °C	500 °C
σ_m	650	500	250
σ_o -average	509	473	432
$\sigma_{order}(1)$	425	454	488
YS	1583	1329	667
k	1	1.2	-
Superposition results	1584	1325	682

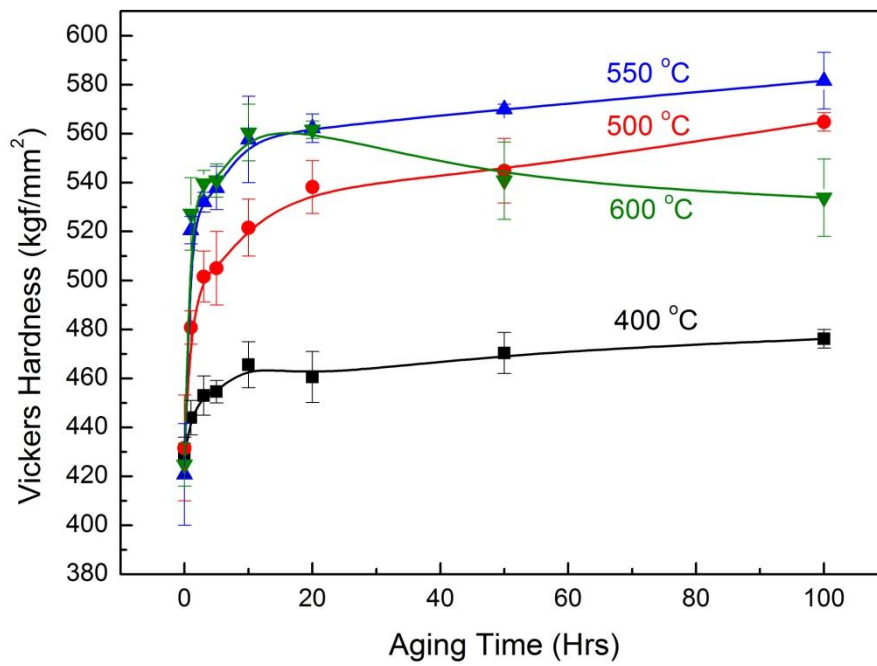


Fig. 5.1 Evolution of Vickers hardness as a function of ageing time.

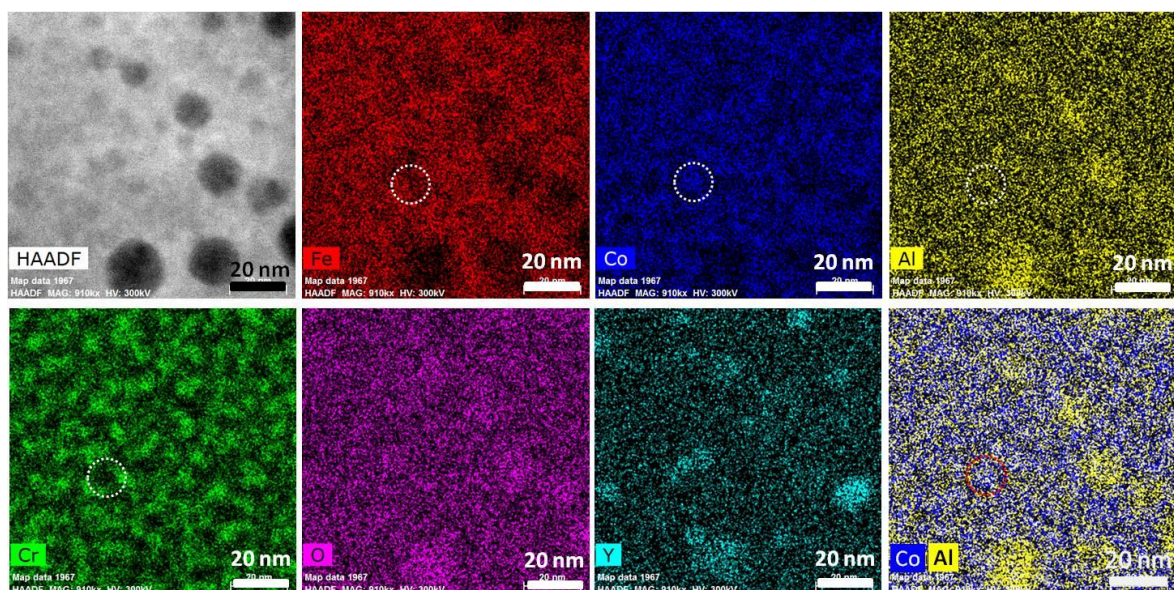


Fig. 5.2 HAADF image and corresponding elemental mappings of 550-20-AT obtained using a Titan-TEM.

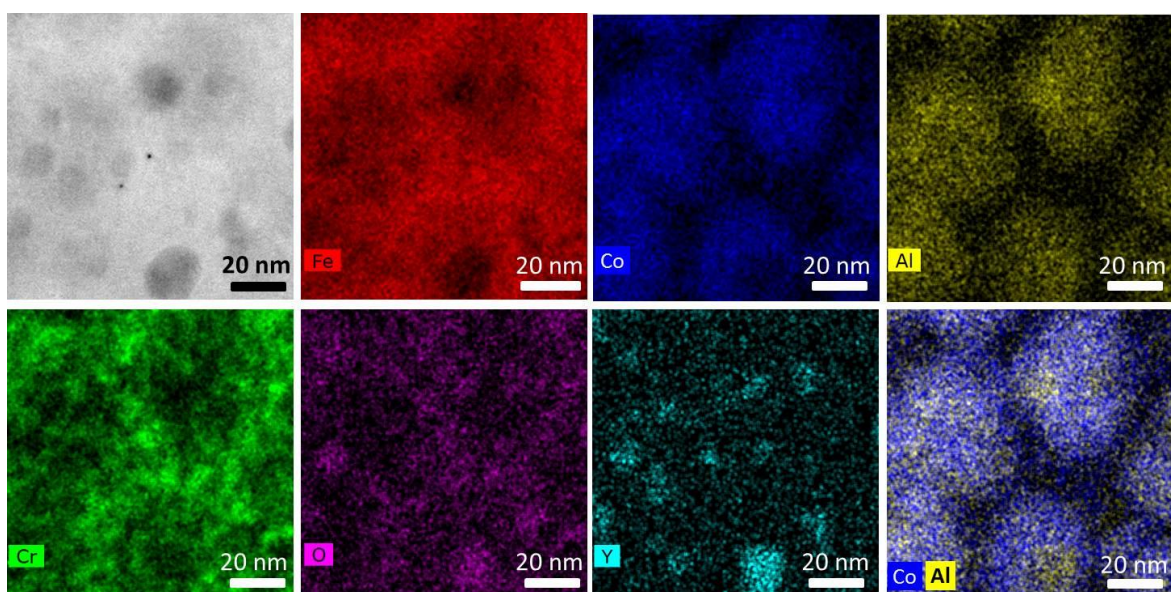


Fig. 5.3 HAADF image and corresponding elemental mappings of 600-100-AT obtained using a Titan-TEM.

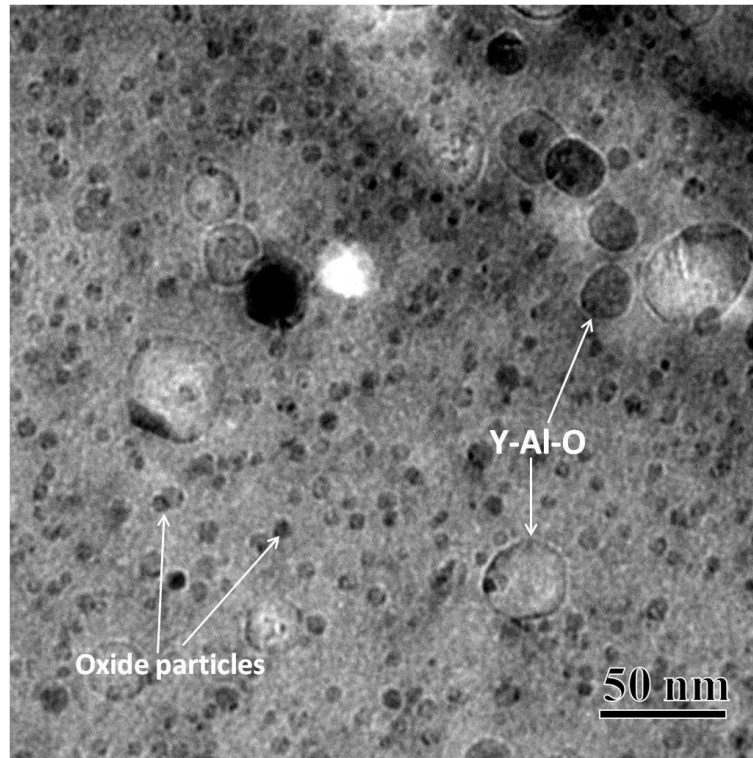


Fig. 5.4 Bright field image of oxide particles observed by TEM.

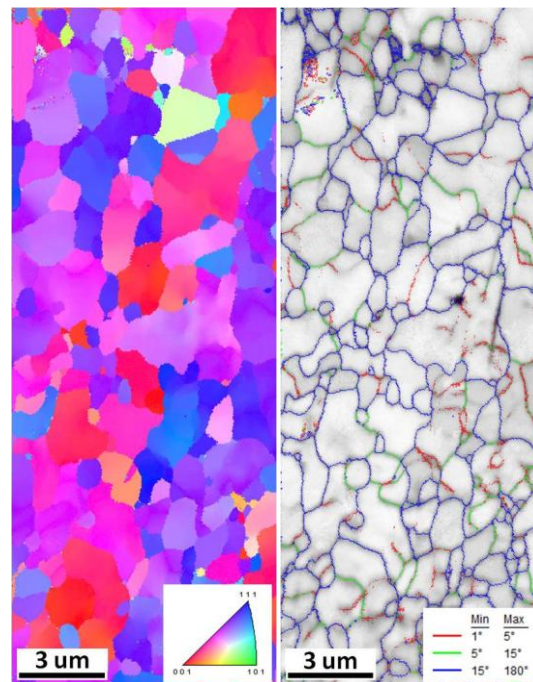


Fig. 5.5 IPF map and corresponding grain boundary map of 550-20-AT.

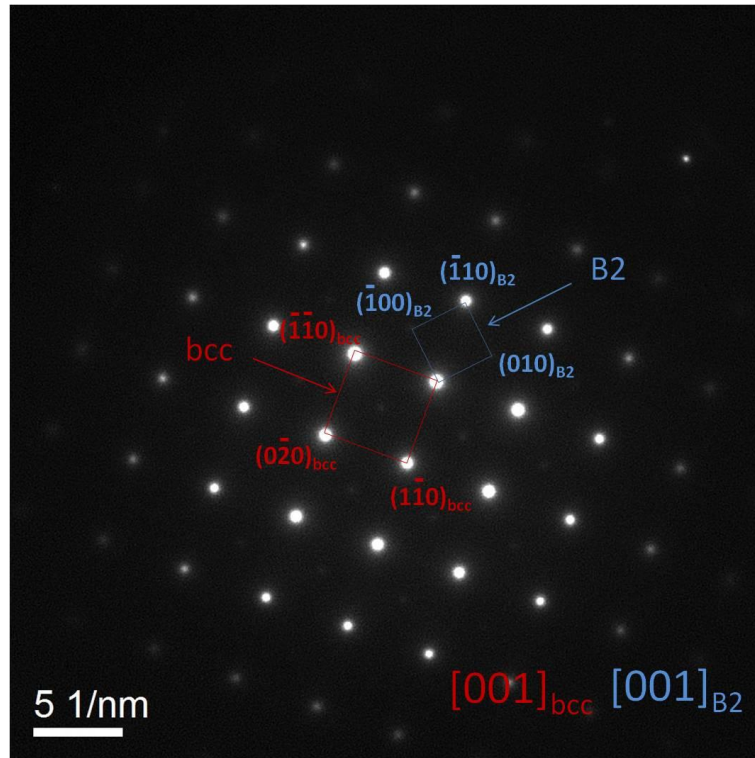


Fig. 5.6 Diffraction pattern of B2 phase and matrix in 550-20-AT obtained by TEM.

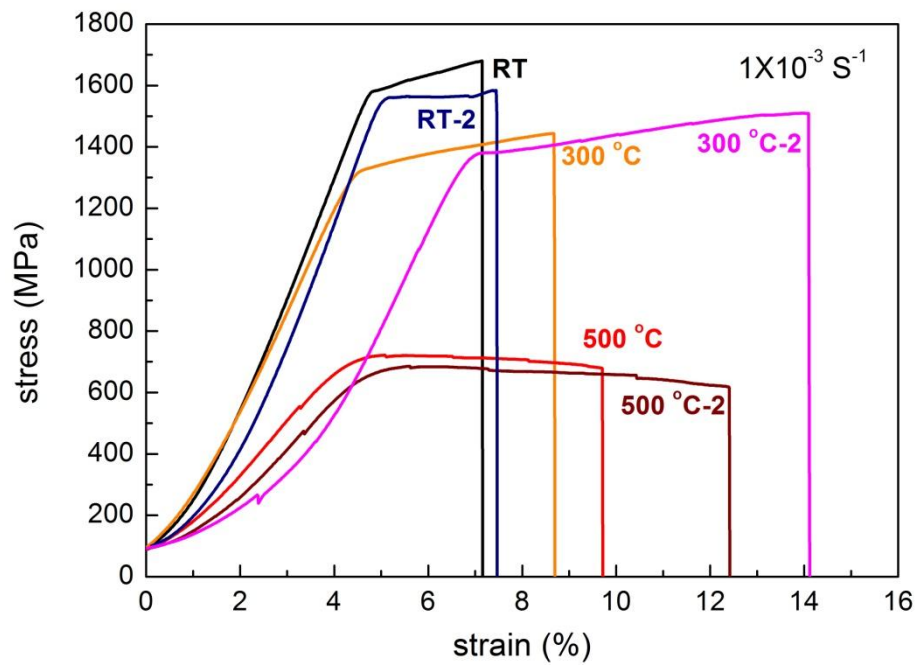


Fig. 5.7 S-S curves of 550-20-AT at RT, 300 °C, 500 °C.

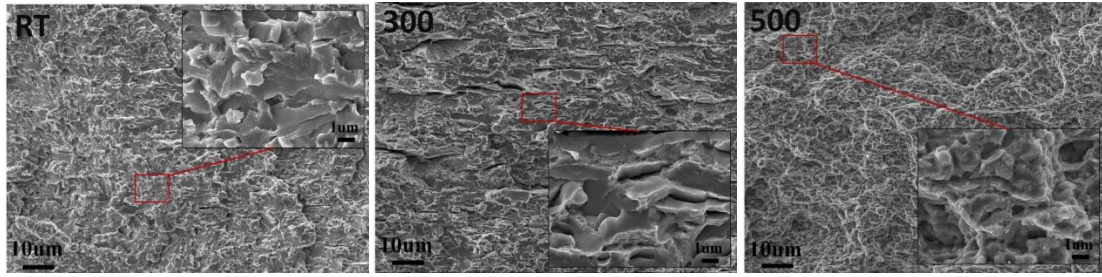


Fig. 5.8 Fracture surfaces of tensile specimens tested at RT, 300 °C and 500 °C.

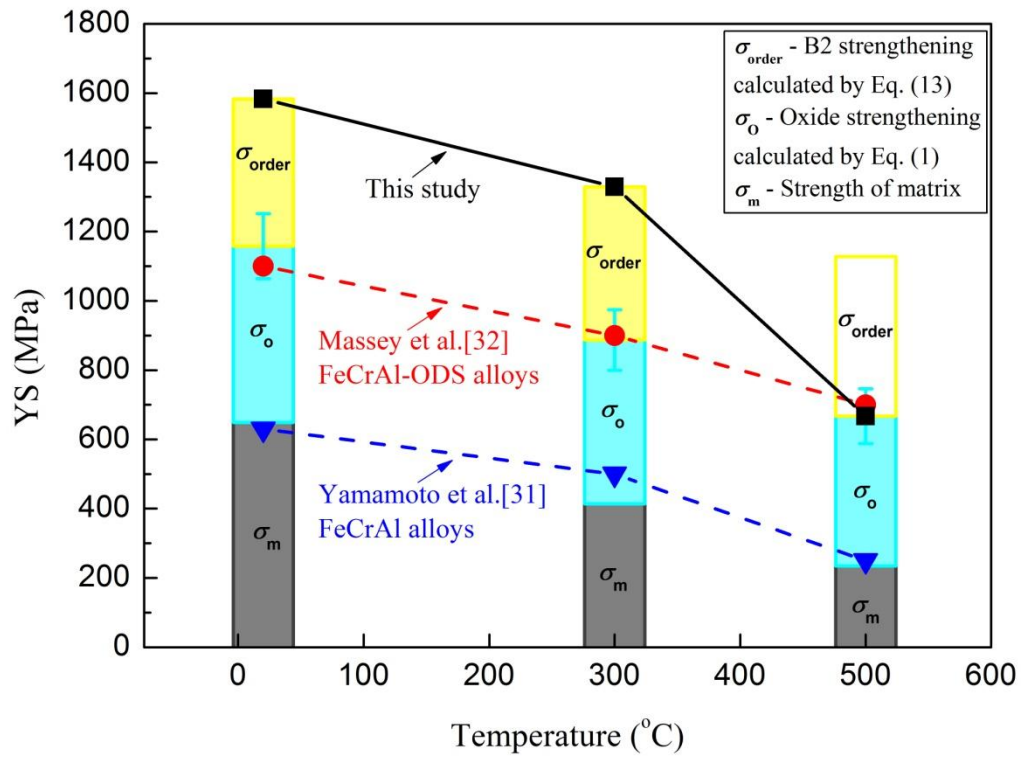


Fig. 5.9 Temperature dependency of order strengthening and oxide dispersion strengthening

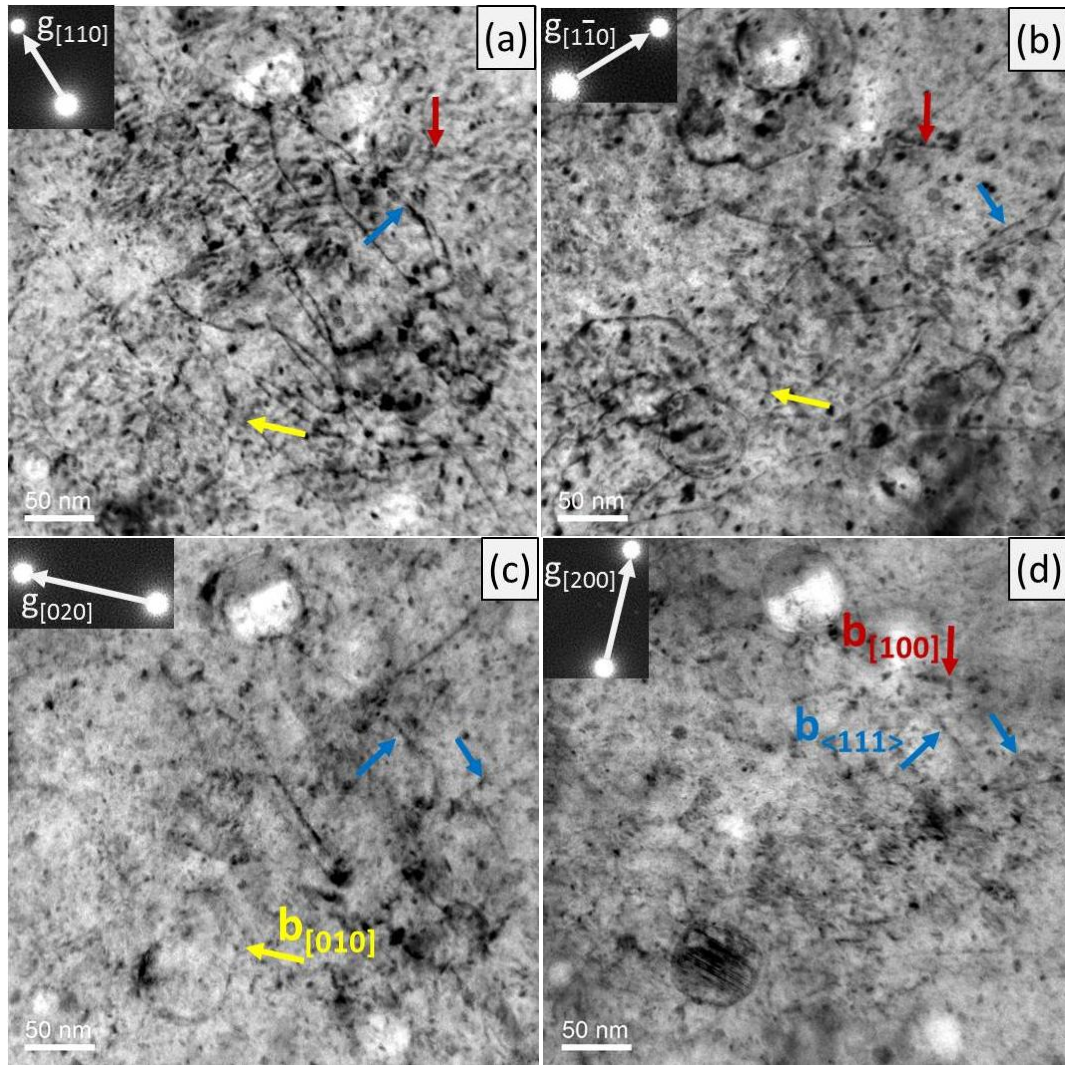


Fig. 5.10 BF-TEM images of tensile specimen tested at 500 °C with four different g -vectors: a) $[110]$, b) $[1\bar{1}0]$, c) $[020]$, d) $[200]$, z -axis= $[001]$.

CHAPTER 6 Development of FeCrAl-ODS alloys by nickel addition

6.1 Introduction

In order to stabilize γ -austenite at solution treatment temperature of around 1000 °C for the Al_2O_3 -forming FeCrAl-ODS alloy, the strong austenite former elements should be incorporated, because typical structure of Fe-12Cr6Al-ODS alloys are α -ferrite up to melting point. US-ORNL has developed Al_2O_3 -forming austenitic alloys; their main composition is Fe-(20-25)Ni-(12-15)Cr-(3-4)Al in wt.% by incorporating with large amount of Ni [126, 127]. However, the stable phase of these austenitic alloys is γ -austenite at the entire temperature ranging from RT to melting point, and γ/α transformation cannot be encountered. Our intention is to make γ/α transformation during cooling, which needs α -phase at the service temperature due to better radiation resistance and prevention of irradiation-assisted stress corrosion cracking (IASCC) as well as γ -phase at solution heat treatment.

In the former chapters, γ/α transformable alloys were developed by Co addition. From the next page, to realize the γ/α transformation in FeCrAl-ODS alloys, available Ni addition was studied as an austenite former element. At first, neutron capture cross section of Ni was surveyed, because it is indispensable for applying to nuclear fuel cladding. **Table 6.1** lists neutron capture cross section of the cladding constituent elements for thermal and fast neutron [128]. The neutron capture cross section of Ni is 1.8 times larger than that of Fe for thermal neutron, suggesting that application of Ni-added alloys to the LWR fuel cladding could be limited. For the fast reactor fuel application, Ni-addition to FeCrAl-ODS alloys is adequately feasible from the neutron capture cross section at the fission spectral neutron.

In this chapter, we explore appropriate phase diagram satisfying above requirement by adding austenite former element Ni into Al_2O_3 -forming FeCrAl-ODS alloys. Thermochemical computer software FactSage was used for this purpose. Under the condition of 5 and 7 wt.% Al to satisfy the Al_2O_3 formation, possibility of γ/α transformation was predicted as a parameter of Ni-content by computing phase diagram using FactSage software. Then, both structural control via γ/α transformation and oxidation resistance via Al_2O_3 formation are experimentally verified, and

optimized composition for Al₂O₃-forming FeCrAl-ODS alloy with γ/α transformation will be proposed.

6.2 Alloying design and computed phase diagram

The base composition of the alloys is FeCrAl-ODS with 12 wt.% Cr and 0.5 wt.% Y₂O₃, where Cr is beneficial element to lower the Al content necessary for the Al₂O₃ scale formation through third element effect [129, 130]. However, excessive Cr addition is detrimental due to causing embrittlement by α' precipitation. From previous results of experiments for FeCrAl alloys, Cr content was set to be 12 wt.%. Y₂O₃ content was selected as 0.5 wt.%, according to the composition of already existed FeCrAl-ODS alloys [131-135].

We have two major targets in this alloying design, which are to make the protective Al₂O₃ scale to prevent steam oxidation as well as possible γ/α transformation to realize capability for the microstructure control. Al content is necessary to be more than about 4 wt.% to produce Al₂O₃ scale [136], however, excessively higher Al content inhibits the formation of γ phase as strong ferrite stabilizing element.

Based on above consideration, the pseudo binary phase diagrams for both composition of Fe-12Cr-5Al-xNi and Fe-12Cr-7Al-xNi were analyzed by using thermochemical computer software FactSage, which are shown in **Fig. 6.1** for Fe-12Cr-5Al-xNi and **Fig. 6.2** for Fe-12Cr-7Al-xNi. Regions in pale blue, pale green and pale red colors correspond to α -ferrite, dual phase of α -ferrite and γ -austenite, and single γ -austenite, respectively. These figures imply that appropriate selection of Ni-content make possible to induce the γ/α transformation during cooling after solid solution heat treatment. As shown in the list of computed phases in **Fig. 6.1**, BCC_A2 is the α -ferrite, B2BCC is NiAl intermetallic compound, BCCA2#2 is the pure Cr and FCC_A1 is the γ -austenite. The single α -ferrite region expands to higher Ni content with increasing Al addition by comparing **Fig. 6.1** and **Fig. 6.2**. Nickel addition of 12, 18, 23 wt.% was selected from **Fig. 6.1** and **Fig. 6.2** as shown by solid circle symbols, where phase transformations are expected during cooling from 1000 °C to room temperature: $\alpha+\gamma$ to α for 12 wt.% Ni, γ to α ($+\gamma$) for 18 wt.% Ni and γ to $\alpha+\gamma$ for 23 wt.% Ni. In addition, intermetallic compound, B2BCC(NiAl) and Ni₅Al₃, are also

predicted.

6.3 Experimental procedure

The FeCrAl-ODS alloys with a parameter of Al and Ni contents were prepared in accordance to a standard process of fabrication except for mechanically alloying. In order to avoid the cold welding of nickel to the surface of the pots and balls during the mechanical alloying, two steps of mechanical alloying were applied. At the preliminary process, Y₂O₃ powder, Fe powder, Cr powder and 50 wt.% Fe-50 wt.% Al alloyed powder were mechanically alloyed for 48 h at 300 rpm, where Fe-Al alloyed powder rather than pure Al powder was used to prevent Al powder adherence; then at the subsequent process Ni powder were added and mechanically alloyed at lower rotational speed of 250 rpm for 24 h to prevent adherence of Ni powder on the surface of pot and balls. **Table 6.2** lists the chemical composition of mechanically alloyed powders measured by X-ray fluorescence, which does not include carbon and oxygen. Target compositions are two levels of Al content: 5 wt.% Al: LAI-LNi(5wt.%Al-12wt.%Ni), LAI-MNi(5wt.%Al-18wt.%Ni), LAI-HNi(5wt.%Al-23wt.%Ni) and 7 wt.% Al: HAI-LNi(7wt.%Al-12wt.%Ni), HAI-MNi(7wt.%Al-18wt.%Ni), HAI-HNi(7wt.%Al-23wt.%Ni), where both contain different Ni contents (12, 18, 23 wt.%). The chemical composition of the mechanically alloyed powders produced in this experiment is slightly dispersed around target.

The mechanically alloyed powders were consolidated by spark plasma sintering (SPS) at 1150 °C for 1 h then solution treated at 1150 °C for 1 h. After solution treatment for homogenization, furnace cooled sample and quenched sample were prepared for chemical composition measurement. Specimens for element analyses by an electron probe micro-analyzer (EPMA) were embedded into resin and grinded with SiC paper and polished with 1 µm diamond. An X-ray diffraction (XRD) samples were cut into a flat circular sheet of about 0.8 mm in thickness with 15 mm diameter. An XRD measurement was carried out using Rigaku-SmartLab with an infrared heating attachment. The specimen was set in a vacuum chamber. Cu-Kα emitted by 40 kV and 200 mA was used, and Bragg Brentano method was applied for measurement in a range of 20 °-90 ° at 2θ with a scan speed of 0.5 ° per minute. 2D single image shot mode was used for the X-ray detection. Measurement was

conducted at room temperature and 1000 °C and during cooling from 1000 °C to room temperature at different cooling rates. Fractions of the γ -phase, α -phase and each precipitate were estimated from a ratio of the measured X-ray intensities to those from the standard specimens.

For oxidation test, 6 specimens were applied as parameters of Al and Ni contents, and SP1 and SP3 [131-135] were also included as reference materials. Chemical composition of SP1 and SP3 are listed in **Table 6.2**, where SP1 is 12CrODS alloy without Al and Ni, and SP3 is typical FeCrAl-ODS steel with 12Cr-5Al. The specimen surfaces were wet ground and polished sufficiently until using 1 μ m-diamond paste and subsequently ultrasonically cleaned in ethanol. Isothermal oxidation test was carried out at 1000 °C up to 49 h in an air-atmosphere muffle furnace, and the oxidation weight gains at different time of exposures were measured by a Sartorius precision electronic balance with an accuracy of 1 μ g.

6.4 Results and discussion

6.4.1 Stable α/γ phases at high and room temperatures

The element distributions in the manufactured specimens were measured by EPMA. As an example, **Fig. 6.3** shows the results of element-mapping of specimen HAl-MNi at the furnace-cooled condition (1.5 °C/min). These data confirm three phases: Fe-based matrix, Ni-Al intermetallic compound and Cr-carbide. The phase diagram computed by Factsage shown in **Fig. 6.2** represents α -ferrite (BCC_A2), two types of intermetallic compound of NiAl (B2BCC) and Al₃Ni₅, and Cr rich phase (BCCA2#2) at room temperature. The two types of intermetallic compounds cannot be separately characterized by EPMA measurement. Two obvious features can be pointed out from **Fig. 6.3**; Ni-Al compound is granular shape precipitates, and Cr rich BCC phase is obviously modified to Cr-carbide by reaction with carbon contaminated during sintering process.

The results of XRD measurements for all of specimens at room temperature are shown in **Fig. 6.4**, and quantitative fraction derived from the X-ray intensity is listed in **Table 6.3**, where specimens were furnace-cooled at extremely slow cooling rate. For specimen HAl-MNi, of which element-mapping is shown in **Fig. 6.3**, Fe-based

matrix is found to be the α -ferrite. 5 wt.% Al specimens lead to more stable γ -phase, while Al-content increased from 5 wt.% to 7 wt.% stabilizes the α -ferrite. Furthermore, close examination by the XRD revealed that intermetallic compound is NiAl with B2 structure and Cr-carbide is the form of Cr_7C_3 .

The results of XRD measurements at 1000 °C are shown in **Fig. 6.5**, and are summarized in **Table 6.4**. Major phase is γ -austenite at 1000 °C except for specimen HAl-LNi, which is dominated by the α -ferrite. This reason could be associated with balance between driving force for the α to γ phase transformation and pinning force by oxide particles. The specimen HAl-LNi with the lowest Ni-content in higher Al-content specimens has the lowest driving force among the manufactured six specimens; thus, it is likely attributed to the retaining α -ferrite during α to γ phase transformation at temperature increasing from room temperature to 1000 °C [137]. This α -ferrite could not be stable, and it will be discussed in the next section.

The phases measured by XRD at 1000 °C and the room temperature are summarized in **Fig. 6.6**, of which data are listed in **Table 6.4** and **Table 6.3**. There are three distinct modes in phase transformation measured by XRD; LAl-HNi is higher Ni-content and lower Al-content enough to stabilize the γ -phase at 1000 °C and the room temperature. On the other hand, the HAl-LNi is stable α -ferrite throughout all temperature ranges due to high Al and low Ni composition. Between these two zones, γ -stabilizing Ni and α -stabilizing Al allow for a γ/α transformation during cooling. For specimen LAl-LNi, the γ -phase is almost only stable phase at 1000 °C, and this γ -phase transforms into an α -phase during cooling thus having almost perfect $\gamma \Rightarrow \alpha$ transformation. For specimen HAl-MNi, both α and γ -phase are stable at 1000 °C, leading to $\gamma + \alpha \Rightarrow \alpha$ transformation. The γ -phase is somewhat more stable having a single γ phase at 1000 °C and γ/α dual phase at room temperature, thus transformation is $\gamma \Rightarrow \gamma + \alpha$ in A2. Finally in HAl-HNi, both phases of γ and α are present at 1000 °C.

Following two points are obviously inconsistent with the computed pseudo-binary phase diagram (**Fig. 6.1** and **Fig. 6.2**). For 7 wt.% Al specimens, large amount of α -ferrite was observed at 1000 °C by XRD. This reason could be ascribed to pinning of α/γ interface by oxide particles during heating, as described in the previous chapters, and this point will be discussed in the next section. The other is concerned with 5 wt.% Al specimens at room temperature. The large amount of γ -austenite

predicted particularly in LAI-HNi might be associated with uncertainty of ($\alpha + \gamma$) and γ phase boundaries in computed pseudo-binary phase diagram.

6.4.2 γ/α phase transformation during cooling

The γ/α phase transformation behavior is studied by using in-situ XRD measurement during cooling from 1000 °C to room temperature. Specimen HAl-MNi was used in this study, and cooling rate was varied in 5, 10, 30, 50 °C/min. The results are represented in **Fig. 6.7**, which is so called continuous cooling transformation (CCT) diagram. It was confirmed in the case of the lowest cooling rate of 5 °C/min that the intensity of γ -peak keeps the same level at the temperature range between 1000 °C to 650 °C, and γ -peak intensity decreases and α -peak increases gradually between 650 °C and 350 °C. Finally, only single α -peak was observed below 350 °C. Similar behavior was observed at 10 °C/min and 30 °C/min. A_3 & A_1 temperatures can be defined in the pseudo binary phase diagrams (**Fig. 6.2**), and A_{r3} & A_{r1} temperatures can be shown in **Fig. 6.7**, based on in-situ XRD results. It is deduced from these results that specimen HAl-MNi is basically consisted of single γ -phase at 1000 °C, and the α -ferrite fraction of 0.21 (**Fig. 6.6**) is not equilibrium phase. Several studies suggest that oxide particle pinning force sometimes prevents α to γ phase transformation, and α -phase retains even at the austenite region, and this α -phase is called as a residual α -ferrite [137]. As shown in **Fig. 6.6**, this residual ferrite fraction systematically decreases in 0.93 α (HAl-LNi), 0.21 α (HAl-MNi) and 0.14 α (HAl-HNi) at 1000 °C in accordance with increasing content of austenite former element Ni. The residual α -ferrite cannot be found at 1000 °C in specimens LAI-LNi, LAI-MNi and LAI-HNi (**Fig. 6.6**). Based on the previous study, the residual α -ferrite formation is dominated by a balance between chemical driving force for a α to γ phase transformation at 1000 °C and an oxide particle pinning force for α/γ interfaces. The chemical driving force corresponds to a free energy difference of the α and γ -phases at 1000 °C, where γ -phase is more stable than α -phase at this temperature. Those were estimated by using Factsage 7.2, and results are listed in **Table 6.5**. The chemical driving forces are obviously low in HAl-LNi, and increase with increasing Ni content for HAl-MNi and HAl-HNi. Those results of the γ -phase fraction vs. chemical driving force are shown in **Fig. 6.8**, suggesting that phases are completely transformed from α

to γ , when the chemical driving force approaches 100 MJ/m^3 . On the other hand, pinning force is affected by the oxide particle dispersion condition, and is generally known to be 5 to 10 MJ/m^3 [137]. Therefore, the lowest case of chemical driving force of 2.5 MJ/m^3 in HAl—LNi forms the residual α -ferrite by higher pinning force than chemical driving force.

The γ and α intensities at the cooling rate of $50 \text{ }^\circ\text{C/min}$ are shown in **Fig. 6.9**. These intensities are almost same at room temperature and $1000 \text{ }^\circ\text{C}$, suggesting that γ to α transformation cannot be induced and almost all γ -phase retain at the cooling rate of $50 \text{ }^\circ\text{C/min}$. It was therefore found that the upper critical cooling rate for γ to α diffusional transformation is between $50 \text{ }^\circ\text{C/min}$ and $30 \text{ }^\circ\text{C/min}$. Furthermore, quench to liquid nitrogen ($-196 \text{ }^\circ\text{C}$) induces γ to α phase transformation, as shown in **Fig. 6.9**, where α -peak intensity obviously increases and γ -intensity decreases. This is most likely caused by the martensitic transformation, and martensite transformation starts at temperature (M_s) somewhere between room temperature ($25 \text{ }^\circ\text{C}$) and $-196 \text{ }^\circ\text{C}$. This result is consistent with Ref. [138] and [139]. These results indicate that γ -austenite is fairly stable and large driving force is necessary to induce martensitic transformation on this alloy.

6.4.3 Oxidation resistance

Fig. 6.10 shows the results of oxidation test up to 49 h at $1000 \text{ }^\circ\text{C}$ in air atmosphere, where horizontal axis means time in root of second and vertical axis means weight gain per unit area in mg cm^{-2} . Specimens HAl-LNi, HAl-MNi and HAl-HNi containing 7 wt% Al undergo stable oxidation behavior, and data band of these specimens is the same level of SP3, which is the typical Al_2O_3 -forming FeCrAl-ODS steel developed in the previous study, and excellent oxidation resistance was demonstrated even at extreme temperature up to $1400 \text{ }^\circ\text{C}$ [131, 132, 134, 135]. The distribution map of aluminum and oxygen in the scale of the specimen HAl-LNi as a representative of this group is shown in **Fig. 6.11**. Continuous alumina scale is certainly confirmed to form on the outer surface of specimen HAl-LNi, because of enrichment of aluminum and oxygen. For specimens LAl-LNi, LAl-MNi and LAl-HNi containing 5 wt.% Al, oxidation weight gains are significantly dispersed; specimen LAl-LNi with 12 wt.% Ni exhibits extremely low oxidation weight gain.

This level is superior to SP3. However, with increasing Ni content from 12 wt.% to 18 wt.% and 23 wt.%, weight gain stepwise increases. Specimen SP1 without Al element takes different oxidation trend; weight gain doesn't saturate, but increases in terms of oxidation time due to chromia (Cr_2O_3) scale rather than alumina (Al_2O_3) scale.

Assuming that oxidation progresses in a parabolic type as shown in Eq. (6.1), parabolic rate constant k_p in $\text{g cm}^{-2} \text{s}^{-1}$, is derived,

$$\Delta w = k_p \sqrt{t} \quad (6.1)$$

where Δw (g cm^{-2}) is weight gain per unit area, t oxidation time in sec. The k_p values derived in this analysis are listed in **Table 6.6**, and are plotted in terms of Al-content measured by EPMA in **Fig. 6.12**, where EPMA measurement was implemented for the water-quenched specimen from 1000 °C to get information on Al matrix content at the oxidation test. Regarding HAl-LNi, HAl-MNi and HAl-HNi, Al-content (4.89 wt.%) measured by EPMA in the matrix of HAl-HNi is lower than the average one (6.47 wt.%) measured by XRF shown in **Table 6.2**, although both measured by EPMA and XRF are almost consistent in the case of HAl-MNi and HAl-LNiB1. This is likely due to Al-consumption by B2BCC (NiAl) formation for higher Ni-containing specimen HAl-HNi, based on consideration of the region ⑫ (FCC and B2BCC) at 1000 °C as shown in **Fig. 6.2**. The k_p level of these specimens is similar to SP3 with 12Cr-5Al without Ni in full-ferrite. On the other hand, the k_p values for LAl-LNi, LAl-MNi and LAl-HNi are considerably dispersed; in particular, specimen LAl-LNi with lower Ni-content took the lowest k_p value, which implied that high Ni content is detrimental for the oxidation behavior of austenitic alloys. The k_p values for LAl-MNi and LAl-HNi increase with slightly decreasing Al-content in the matrix. Interpretation of this trend and change of Al-content in LAl-LNi, LAl-MNi and LAl-HNi is not clear. One of the possible reasons could be related to B2BCC (NiAl) formation in higher Ni-content: LAl-MNi and LAl-HNi as being similar to specimen HAl-HNi. For 5 wt.% Al specimens, however, the pseudo binary phase diagram suggests that B2BCC is unstable at 1000 °C. We think that uncertainty still exists in the computed phase diagram. Based on the experimental results shown in **Fig. 6.12**, Al-content could be critical at around 5 wt.%; oxidation is resisted above 5 wt.% and accelerated below 5 wt.%. This result coincides with Fe-Cr-Al oxide map at 1100 °C reported by Mrowec et al. [140], where Al-content is around 4.5 wt.% Al for scale boundary between Al_2O_3

and Fe_2O_3 scale.

6.5 Conclusion

In order to develop the α/γ transformable Al_2O_3 -forming FeCrAl-ODS steels, six kinds of alloys were produced in the parameter of Al-content (5 and 7 wt.%) and Ni-content (12, 18, 23 wt.%) through mechanical alloying on the basis of Fe-12Cr-0.5Y₂O₃. These compositions were selected from the pseudo binary phase diagram computed by FactSage software. The γ/α phase transformation during cooling after solution treatment and oxidation resistance due to Al_2O_3 formation at 1000 °C were investigated. Combination of the high Al and low Ni leads to stabilization of the α -ferrite at 1000 °C, which could be resulted from the pinning of γ/α boundaries by the oxide particles. In contrast, low Al and high Ni provides γ -austenite at room temperature. The low Al (5 wt.%) & low Ni (12 wt.%) or high Al (7 wt.%) & high Ni (23 wt.%) are preferable for γ to α phase transformation during cooling. A_{C1} and A_{C3} temperatures and critical cooling rate for the martensite transformation were also clarified. The oxidation test in air at 1000 °C revealed that 7 wt.% Al is enough to form Al_2O_3 scale. Even at 5 wt.% Al, the reduced Ni-content induces superior resistance for the oxidation via Al_2O_3 formation. This could be resulted from maintaining Al-content in matrix by suppressing formation of the Ni-Al intermetallic compound. Based on above results, LAI-LNi (5 wt.% Al-12 wt.% Ni) and HAI-HNi (7 wt.% Al-23 wt.% Ni) are recommended as a preferable composition for α/γ transformable Al_2O_3 -forming FeCrAl-ODS steels.

Table 6.1 Neutron capture cross section for main isotopes.

Isotope	Abundance (%)	Thermal neutron 0.025 eV (burn)	Fission spectral average (m burn)
Fe-56	92	2.60	3.40
Cr-52	84	0.86	1.90
Al-27	100	0.23	0.67
Y-89	100	1.28	4.87
Ni-58	68	4.62	8.70
Ni-60	26	2.90	6.36

Table 6.2 Chemical composition of mechanically alloyed powders measured by XRF
in wt.%

Specimen	Fe	Cr	Al	Ni	Y ₂ O ₃	Comments
LAl-LNi	70.85	11.76	4.30	12.68	0.41	
LAl-MNi	65.11	11.52	4.84	18.05	0.48	
LAl-HNi	61.92	11.21	4.09	22.30	0.48	
HAl-LNi	69.50	11.40	6.82	11.85	0.43	
HAl-MNi	64.87	10.84	6.04	17.83	0.42	
HAl-HNi	59.21	11.45	6.47	22.45	0.42	
SP1	85.85	11.78	—	—	0.24	W=1.9 Ti=0.23
SP3	82.58	11.72	4.71	—	0.47	Ti=0.52

Table 6.3 Fraction of each phase measured by XRD at RT

	Composition	γ -austenite	α -ferrite	Cr ₇ C ₃	NiAl
LAl-LNi	5Al-12Ni	0.03	0.94	0.01	0.03
LAl-MNi	5Al-18Ni	0.37	0.58	0.02	0.03
LAl-HNi	5Al-23Ni	0.88	0.08	0.02	0.02
HAl-LNi	7Al-12Ni	0	0.98	0.01	0.01
HAl-MNi	7Al-18Ni	0	0.96	0.01	0.03
HAl-HNi	7Al-23Ni	0	0.96	0.00	0.04

Table 6.4 Fraction of each phase measured by XRD at 1000 °C.

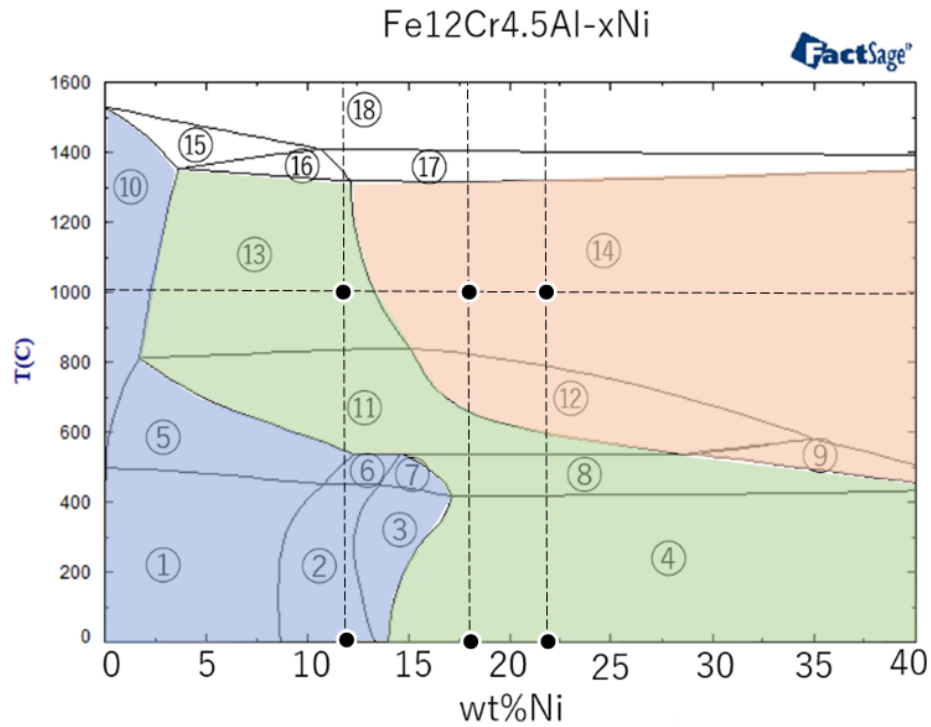
	Composition	γ -austenite	α -ferrite	Cr_7C_3	NiAl
LAl-LNi	5Al-12Ni	0.97	0.0	0.03	0.0
LAl-MNi	5Al-18Ni	1.00	0.0	0.0	0.0
LAl-HNi	5Al-23Ni	1.00	0.0	0.0	0.0
HAl-LNi	7Al-12Ni	0.03	0.93	0.04	0.01
HAl-MNi	7Al-18Ni	0.75	0.21	0.04	0.0
HAl-HNi	7Al-23Ni	0.84	0.14	0.01	0.01

Table 6.5 Chemical driving force for α - γ phase transformation at 1000 °C that was estimated by FactSage computer software.

	LAl-LNi	LAl-MNi	LAl-HNi	HAl-LNi	HAl-MNi	HAl-HNi
Chemical driving force (MJ/m ³)	146.3	347.0	484.3	2.5	76.0	137.5

Table 6.6 Parabolic rate constant k_p for oxidation at 1000 °C

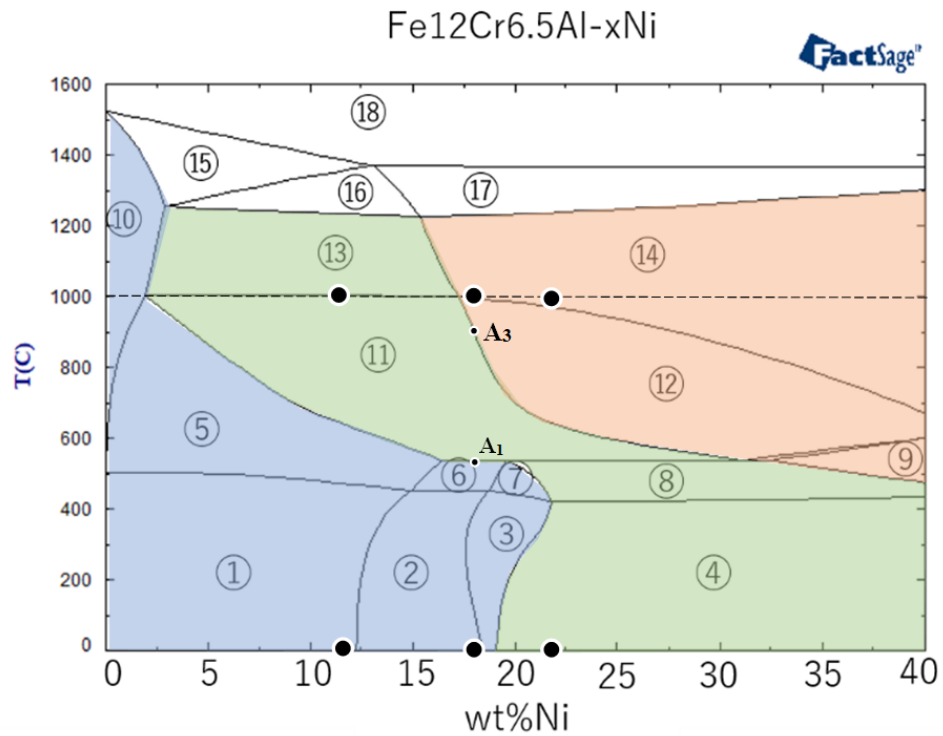
Specimen	$k_p \times 10^{-2} \text{ (mg cm}^{-2} \text{ h}^{-1/2})$
LAl-LNi	2.02
LAl-MNi	6.24
LAl-HNi	4.30
HAl-LNi	2.15
HAl-MNi	2.17
HAl-HNi	1.87
SP1	7.74
SP3	3.03



- ① : B2BCC, BCC_A2, BCC_A2#2
- ② : B2BCC, BCC_A2, BCC_A2#2, Al3Ni5
- ③ : BCC_A2, BCC_A2#2, Al3Ni5
- ④ : FCC_A1, BCC_A2, BCC_A2#2, Al3Ni5
- ⑤ : BCC_A2, B2BCC
- ⑥ : BCC_A2, B2BCC, Al3Ni5
- ⑦ : BCC_A2, Al3Ni5
- ⑧ : FCC_A1, BCC_A2, Al3Ni5
- ⑨ : FCC_A1, Al3Ni5
- ⑩ : BCC_A2
- ⑪ : BCC_A2, FCC_A1, B2BCC
- ⑫ : FCC_A1, B2BCC
- ⑬ : BCC_A2, FCC_A1
- ⑭ : FCC_A1
- ⑮ : Liquid, BCC_A2
- ⑯ : Liquid, BCC_A2, FCC_A1
- ⑰ : Liquid, FCC_A1
- ⑱ : Liquid

	α matrix
	$\alpha + \gamma$ matrix
	γ matrix

Fig. 6.1 Pseudo binary phase diagram Fe-12Cr-5Al-xNi calculated by FactSage



- ① : B2BCC, BCC_A2, BCC_A2#2
- ② : B2BCC, BCC_A2, BCC_A2#2, Al3Ni5
- ③ : BCC_A2, BCC_A2#2, Al3Ni5
- ④ : FCC_A1, BCC_A2, BCC_A2#2, Al3Ni5
- ⑤ : BCC_A2, B2BCC
- ⑥ : BCC_A2, B2BCC, Al3Ni5
- ⑦ : BCC_A2, Al3Ni5
- ⑧ : FCC_A1, BCC_A2, Al3Ni5
- ⑨ : FCC_A1, Al3Ni5
- ⑩ : BCC_A2
- ⑪ : BCC_A2, FCC_A1, B2BCC
- ⑫ : FCC_A1, B2BCC
- ⑬ : BCC_A2, FCC_A1
- ⑭ : FCC_A1
- ⑮ : Liquid, BCC_A2
- ⑯ : Liquid, BCC_A2, FCC_A1
- ⑰ : Liquid, FCC_A1
- ⑱ : Liquid

α matrix
 α + γ matrix
 γ matrix

Fig. 6.2 Pseudo binary phase diagram Fe-12Cr-7Al-xNi calculated by FactSage

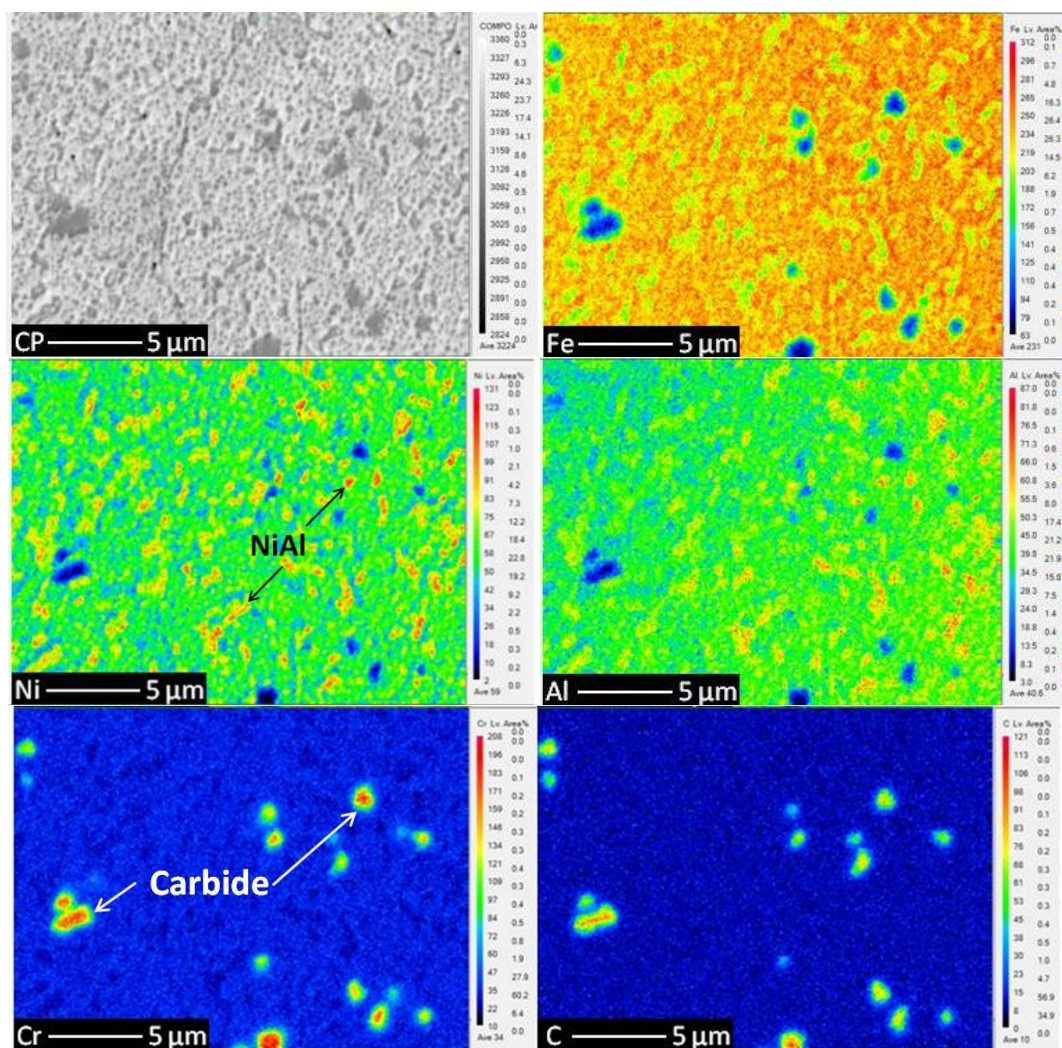


Fig. 6.3 EPMA Mapping of specimen HAl-MNi after being furnace cooled at 1.5 °C/min.

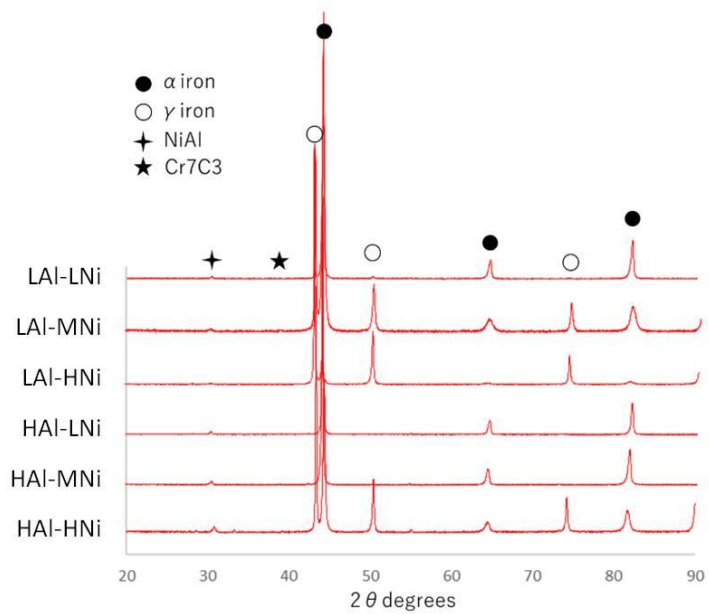


Fig. 6.4 XRD results at RT after furnace cooling at 1.5 °C/min.

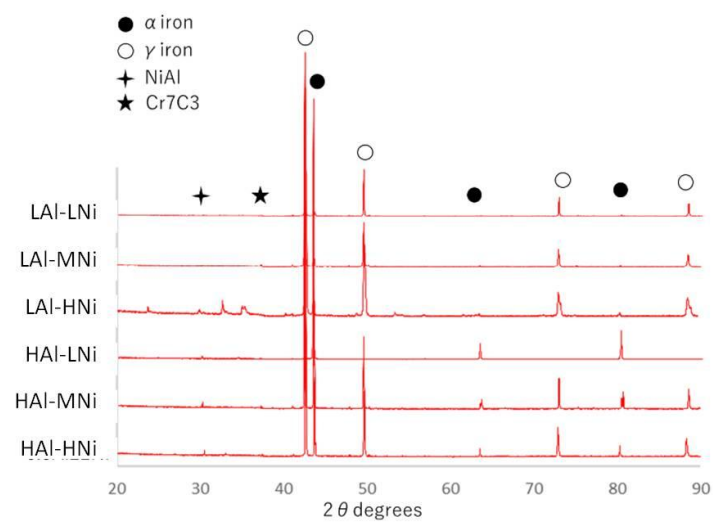


Fig. 6.5 In-situ XRD results at 1000 °C

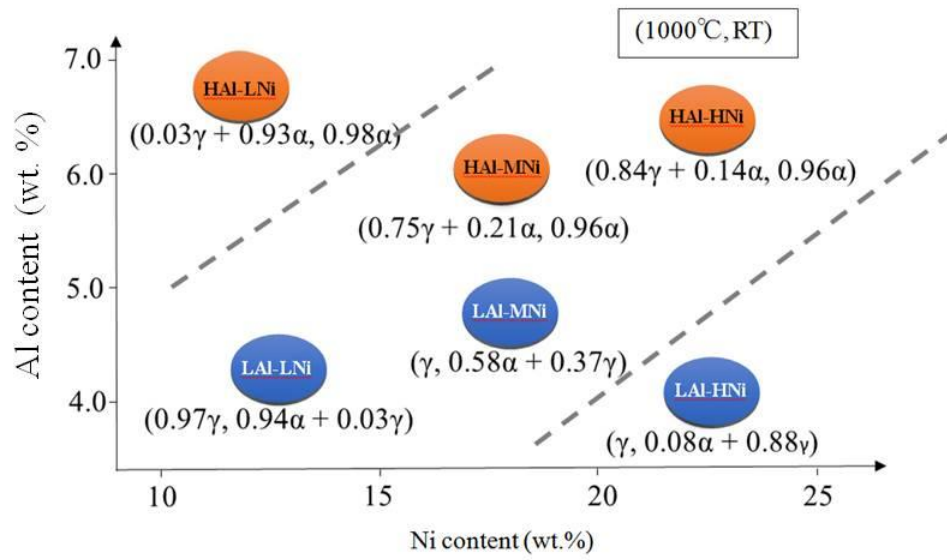


Fig. 6.6 Phase fraction at 1000 °C and RT measured by XRD in the diagram of Ni-Al contents.

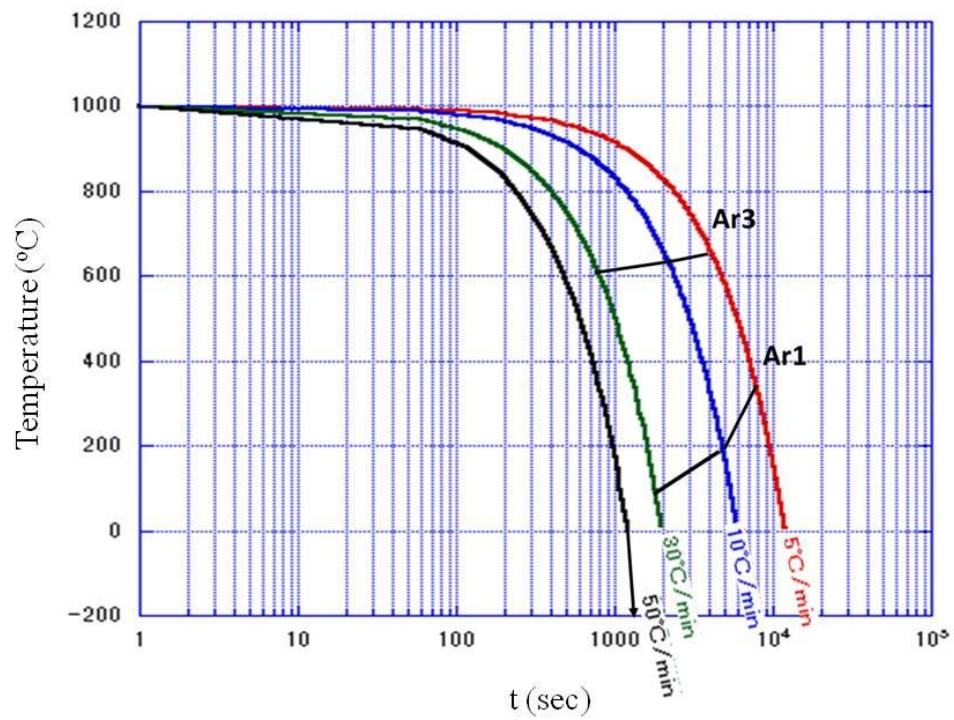


Fig. 6.7 Continuous cooling transformation diagram for specimen HAl-MNi at various cooling rates.

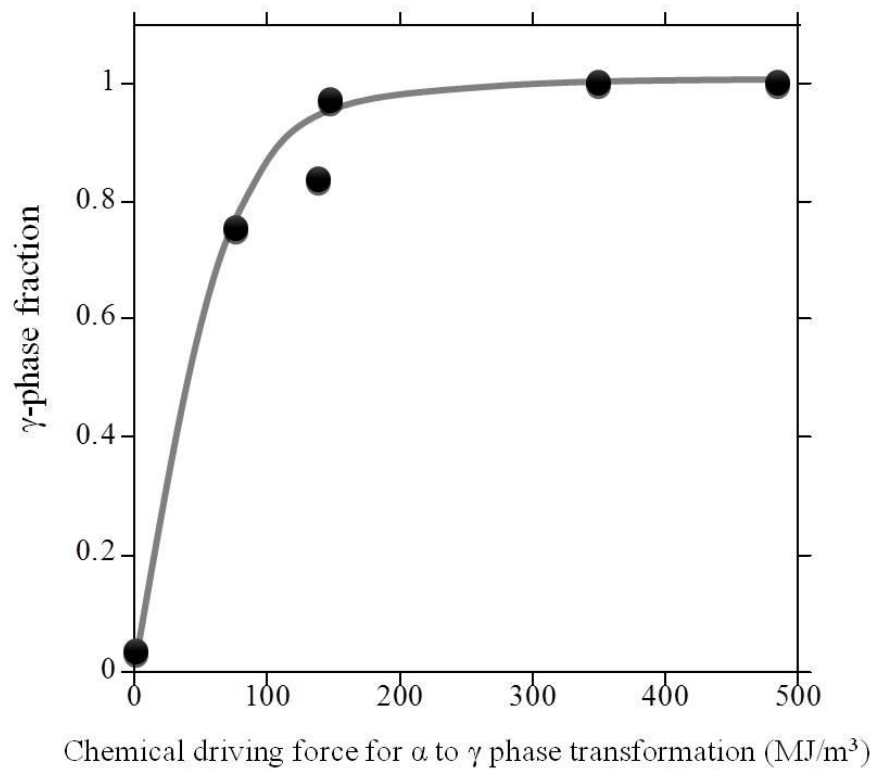


Fig. 6.8 γ -phase fraction vs. chemical driving force for α to γ phase transformation at 1000 °C that was estimated by FactSage 7.2 computer software.

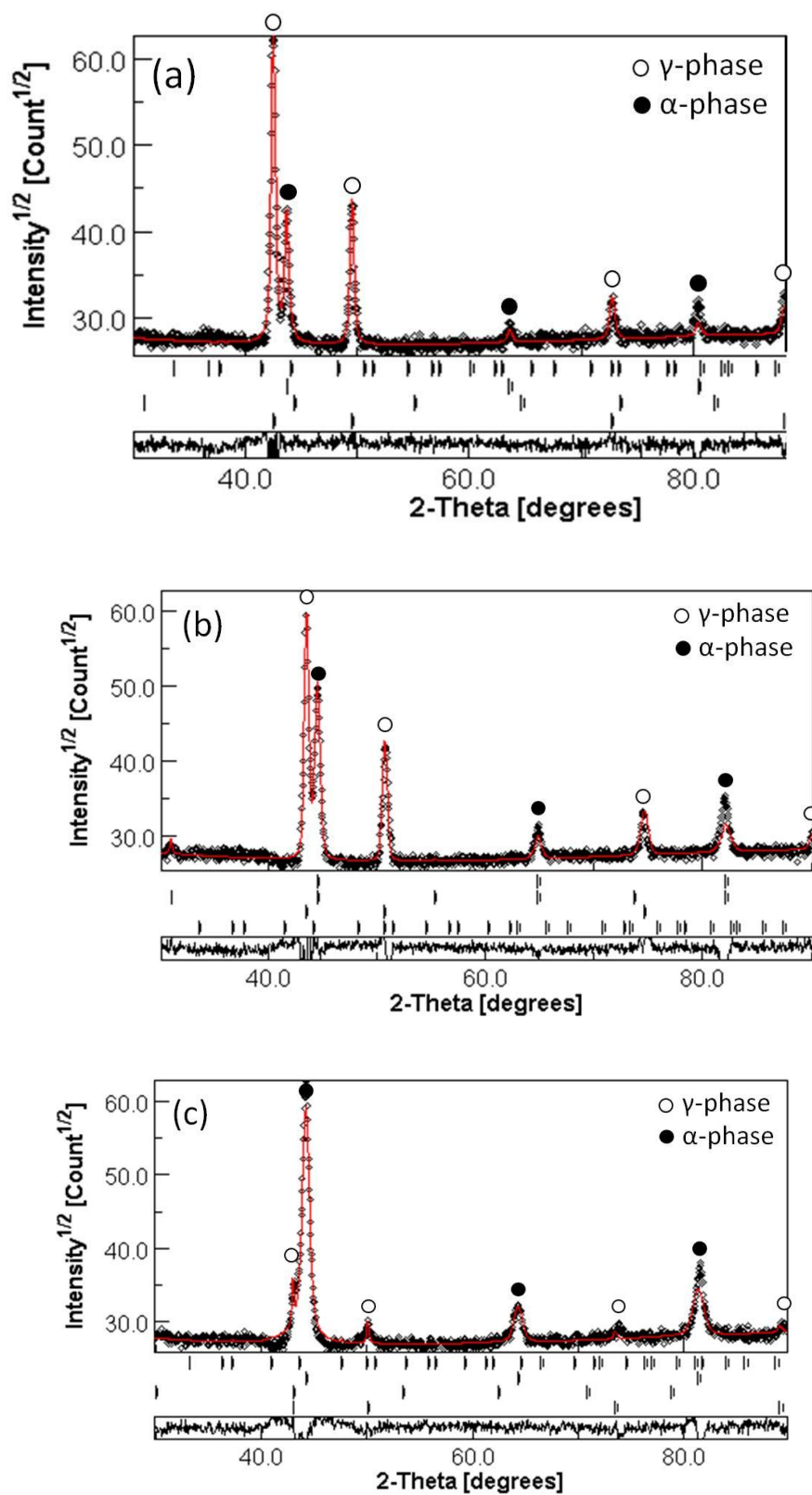


Fig. 6.9 XRD results at (a) 1000 °C, (b) RT and (c) -196 °C for specimen HA1-MNi at cooling rate of 50 °C/min.

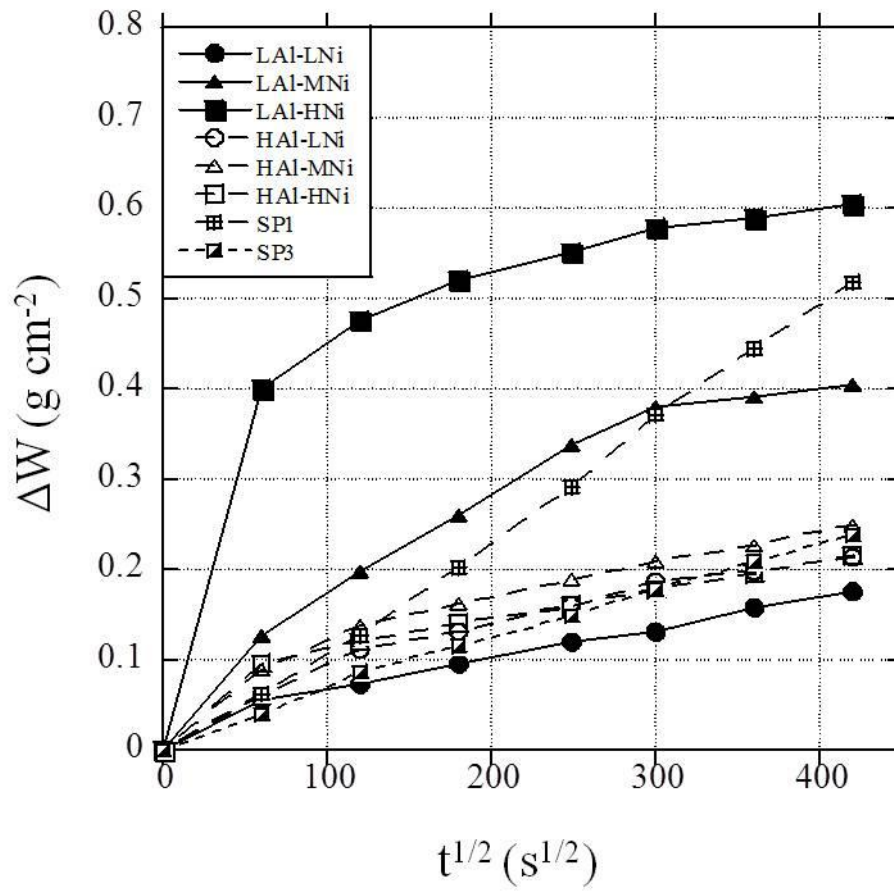


Fig. 6.10 Weight gain vs. square root of oxidation time at 1000 °C.

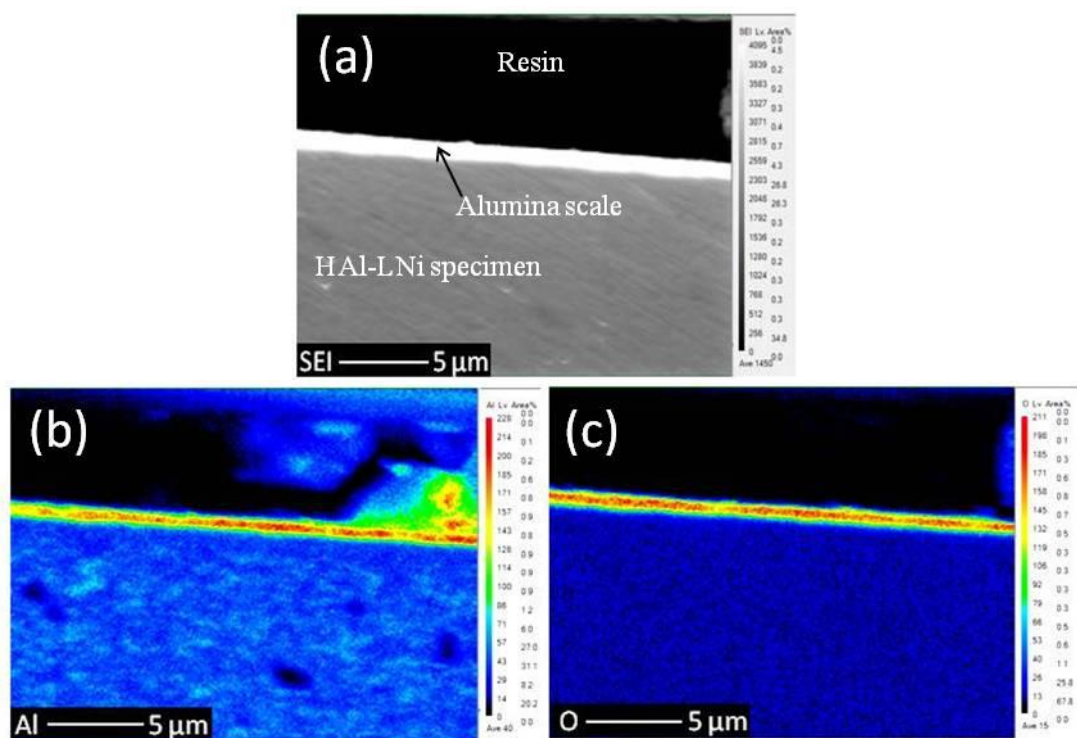


Fig. 6.11 (a) SEM, (b) aluminum and (c) oxygen distribution for specimen HAl-LNi at the initial scale after 1 h oxidation at 1000 °C.

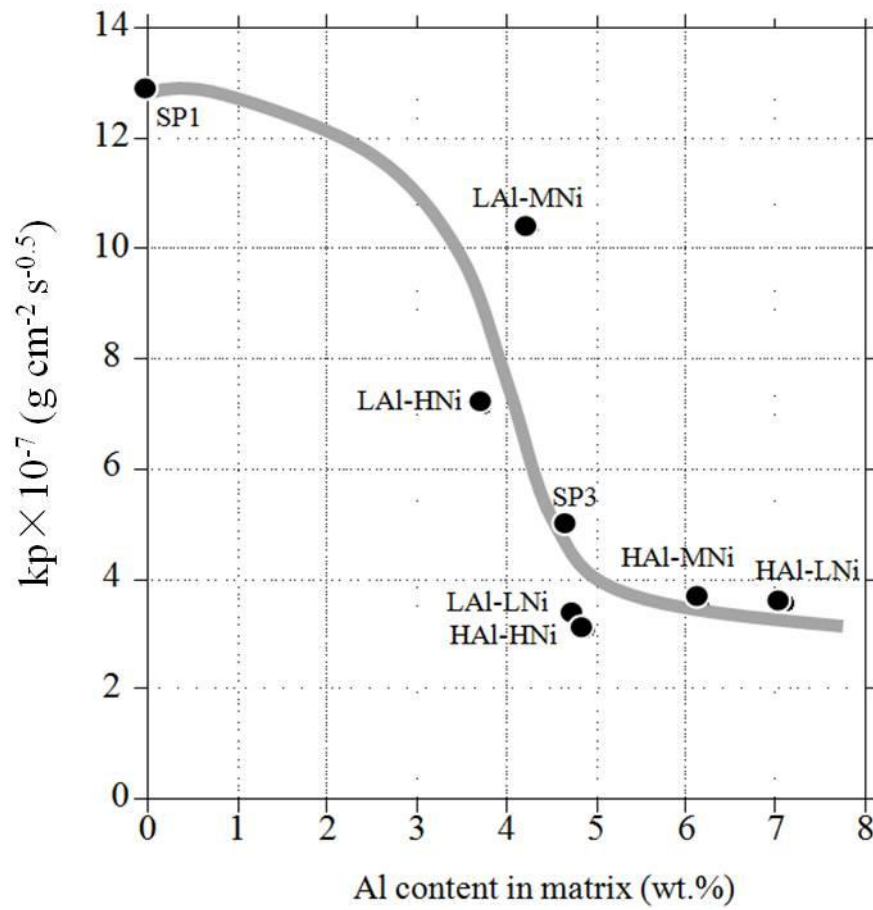


Fig. 6.12 k_p vs. aluminum concentration in matrix measured by EPMA for quench specimen from 1000 °C.

CHAPTER 7 Conclusions

In order to modify microstructure and obtain equiaxial grains in FeCrAl ODS alloys using γ/α transformation, the Co-added and Ni-added FeCrAl ODS alloys were developed. Fe-12Cr-(3,5)Al-(15,25)Co-0.5Y₂O₃ (wt.%) ODS alloys and Fe-12Cr-(5,7)Al-(12,18,23)Ni-0.5Y₂O₃ (wt.%) were designed based on the pseudo phase diagram and fabricated using mechanical alloying (MA), spark plasma sintering (SPS), hot rolling and final annealing at 1150 °C. In the past three years, fruitful results were obtained with respect to microstructure and phase transformation characterization, high temperature oxidation mechanism and mechanical properties evaluation. The main achievements are concluded as follows:

(1) Microstructure and phase transformation characterization

According to the characterization results of Co-added alloys, three phases were identified: matrix with bcc structure, chromium carbide, and dispersed CoAl intermetallic compound. Nanosized oxide particles were also characterized by transmission electron microscopy. As the temperature increased to 1000 °C, the 3Al-alloys with 15 or 25 wt.% Co and 5Al alloy with 25 wt.% Co demonstrated α to γ transformation, whilst α -phase remained in the 5Al-alloy with 15 wt.% Co. Suppression of α to γ transformation in specimen 5Al15Co was successfully explained by the pinning of α/γ interfaces by oxide particles. Continuous cooling transformation curves constructed by in-situ high temperature X-ray diffraction showed that microstructure control using the γ/α phase transformation is feasible.

The results of microstructure characterization of Ni-added alloys showed that combination of the high Al and low Ni leads to stabilization of the α -ferrite at 1000 °C, which could be resulted from the pinning of γ/α boundary by the oxide particles. In contrast, low Al and high Ni provides γ -austenite at room temperature. The Fe12Cr5Al12Ni ODS alloy and Fe12Cr7Al22Ni ODS alloy are preferable for γ to α phase transformation during cooling. A_{C1} and A_{C3} temperatures and critical cooling rate for the martensite transformation were also clarified.

(2) High temperature oxidation mechanism

The high temperature oxidation behavior of Co-added alloys was studied at 800 °C, 900 °C and 1000 °C in air. Exclusive alpha-alumina scales were formed on the surfaces of 5Al alloys at the temperature range from 800 °C to 1000 °C. The Co

addition increased the thickness of outer layer and the lateral grain size of alumina with depth beneath the oxide/gas interface. The decrease of oxidation kinetics of Co-added 5Al alloys was attributed to the increase of the lateral grain size of alumina which led to decrease the fraction of diffusion sites within the boundary decrease. On the other hand, protective alpha-alumina scales were also formed on the surfaces of 3Al alloys at the temperature range from 800 °C to 900 °C except for the 3Al15Co alloy oxidized at 900 °C. The Co addition was detrimental to the oxidation kinetics when 3Al alloys were oxidized at 800 °C and 900 °C. The severe oxidation of 3Al15Co alloy at 900 °C may be due to the phase transformation process. 3 wt. % of Al was not sufficient forming protective alumina scale at 1000 °C.

The oxidation test at 1000 °C in air revealed that 7 wt.% Al is sufficient to form protective Al₂O₃ scale. Even at 5 wt.% Al, the reduced Ni-content induces superior oxidation resistance via Al₂O₃ formation. This could be resulted from maintaining Al-content in matrix by suppressing formation of the Ni-Al intermetallic compound.

(3) Mechanical properties evaluation

On the consideration of phase transformation and high temperature oxidation behavior, the tensile properties of Fe12Cr5Al25Co ODS alloy were evaluated, focusing on the oxide dispersion strengthening and B2-type CoAl ordered strengthening at both ambient and elevated temperatures. The oxide particles and B2-type CoAl precipitate were characterized using transmission electron microscopy, and strengthening mechanisms for the oxide particles and CoAl-precipitate were evaluated by hardness and tensile tests at room temperature, 300 °C, and 500 °C. The theoretically estimated values showed good agreement with the experimental results at RT and 300 °C. However, the order strengthening by CoAl precipitates was significantly reduced at 500 °C, which is attributed to the increase of thermally activated {001} slip in the body-centered cubic matrix. The {001} slip weakens the dislocation interaction with CoAl precipitates with the same {001} slip system.

In conclusion, since 5 wt. % of Al provided exclusive alpha-alumina at the temperature range from 800 °C to 1000 °C and 25 wt. % of Co addition made Fe12Cr5Al ODS alloys phase transformable, Fe12Cr5Al25Co ODS alloy was the optimal composition for Co-added alloys. Besides, it possessed sufficient strength. Regarding Ni-added alloys, Fe12Cr5Al12Ni ODS alloy and Fe12Cr7Al22Ni ODS

alloy were considered to be preferable compositions for transformable Al_2O_3 -forming FeCrAl-ODS alloys.

References

- [1] T. M. Pollock, S. Tin. J. Propuls. Power, 22 (2006) 361-374.
- [2] A. Bauer, S. Neumeier, F. Pyczak, M. Göken, Scr. Mater. 63 (2010) 1197-1200.
- [3] A. Bauer, S. Neumeier, F. Pyczak, R.F. Singer, M. Göken, Mater. Sci. Eng. A 550 (2012) 333-341.
- [4] H.Long, S. Mao, Y. Liu, Z. Zhang, X. Han, J. Alloys Compd. 743 (2018) 203-220.
- [5] H. Kodama, H. Sakamoto, T. Miyoshi, J. Am. Ceram. Soc. 72 (1989) 551-558.
- [6] Sixth annual report -High Temperature materials program, 1967.
- [7] Fourth Annual Report-High temperature materials and reactor component development programs, 1965.
- [8] Fith annual report on high temperature materials programs - Part A, 1966.
- [9] Seventh annual report - AEC Fuels and Materials Development program, (1968) 368.
- [10] High-Temperature Materials Program Progress Report No. 59, Part A, GEMP-59A. (1966).
- [11] High-Temperature Materials Program Progress Report No. 55, Part A, GEMP-55A. (1966).
- [12] Fourth Annual Report-High-Temperature Materials and Reactor Component Development Programs, GEMP-334A. (1965).
- [13] J.F. Collins, F.C. Robertshaw, Advanced Long-Life Reactor Fuel Cladding and Structural Materials Development, General Electric, Cincinnati, Ohio, 1967.
- [14] G.R. VanHouten, M.R. Broz, Advanced Log-Life Reactor Fuel Element, Moderator, Control, and Shield Materials Development, General Electric, Cincinnati, Ohio, n.d.
- [15] E.A. Little, D.A. Stow, J. Nucl. Mater. 87 (1979) 25-39.
- [16] F.G. Wilson, B.R. Knott, C.D. Metall. Trans. A. 9 (1978) 275-282.
- [17] M. Kangilaski, R.E.I. Center, REIC Rep. No. 45. (1967) 94-103.
- [18] S. J. Zinkle, K. A. Terrani, J. C. Gehin, L. J. Ott, L. L. Snead, J, Nucl. Mater. 448 (1-3) (2014) 374-379.
- [19] K. A. Terran, S. J. Zinkle, L. L. Snead, J. Nucl. Mater. 448 (2014) 420-435.

- [20] Y. Yamamoto, B. A. Pint, K. A. Terrani, K. G. Field, Y. Yang, L. L. Snead, J. Nucl. Mater. 467 (2015) 703-716.
- [21] K. G. Field, S. A. Briggs, K. Sridharan, R. H. Howard, Y. Yamamoto, J. Nucl. Mater. 489 (2017) 118-128.
- [22] K.A. Terrani, J. Nucl. Mater. 501 (2018) 13-30.
- [23] S. Ukai, N. Oono, S. Ohtsuka, T. Kaito, K. Sakamoto, T. Torimaru, A. Kimura, S. Hayashi, Proceeding of LWR Fuel with Enhanced Safety and Performance, TOPFUEL2016, September 13, 2016, Boise, Idaho, USA.
- [24] S. Ukai, N. Oono, K. Sakamoto, T. Torimaru, T. Kaito, A. Kimura, S. Hayashi, Proceedings of ICAPP, April 24-28, 2017, Fukui and Kyoto (Japan).
- [25] M. Yamamoto, S. Ukai, S. Hayashi, T. Kaito, S. Ohtsuka, J. Nucl. Mater. 417 (2011) 237-240.
- [26] S. Ukai, S. Ohtsuka, T. Kaito, H. Sakasegawa, N. Chikata and S. Hayashi, Mater. Sci. Eng. A 510 (2009) 115-120.
- [27] S. Ukai, S. Muzuta, M. Fujiwara, T. Okuda and T. Kobayashi, J. Nucl. Sci. Technol. 39 (2002) 778-788.
- [28] B. Leng, S. Ukai, Y. Sugino, Q. Tang, T. Narita, S. Hayashi, F. Wan. S. Ohtsuka and T. Kaito, ISIJ Int. 51 (2011) 951-957.
- [29] T. Narita, S. Ukai, T. Kaito, S. Otsuka and T. Kobayashi, J. Nucl. Sci. Technol. 41 (2004) 1008-1012.
- [30] S. Ukai, T. Okuda, M. Fujiwara, T. Kobayashi, S. Mizuta, H. Nakashima, J. Nucl. Sci. Technol. 39 (2002) 872-879.
- [31] A. Kimura, R. Kasada, N. Iwata, H. Kishimoto, C.H. Zhang, J. Isselin, P. Dou, J.H. Lee, N. Muthukumar, T. Okuda, M. Inoue, S. Ukai, S. Ohnuki, T. Fujisawa, F. Abe, J. Nucl. Mater. 417 (2011) 176-179.
- [32] T. Narita, S. Ukai, T. Kaito, S. Otsuka and T. Kobayashi, J. Nucl. Sci. Technol. 41 (2004) 1008-1012.
- [33] S. Ukai, S. Mizuta, T. Yoshitake, T. Okuda, M. Fujiwara, S. Hagi, T. Kobayashi, J. Nucl. Mater. 283-287 (2000) 702-706.
- [34] S. Ukai, S. Ohtsuka, T. Kaito, Y. de Carlan, J. Ribis, J. Malaplate. Structural Materials for Generation IV Nuclear Reactors. Woodhead publishing, Cambridge. (2017) 357-414.

- [35] Kelly, A., Strengthening methods in crystals. 1971: Elsevier Pub. Co.
- [36] M.J. Alinger: Ph.D dissertation, University of California Santa Barbara, 2004.
- [37] S. Ukai, S. Ohtsuka, T. Kaito, H. Sakasegawa, N. Chikata, S. Hayashi, S. Ohnuki, Mater. Sci. Eng. A 510-511 (2009) 115-120.
- [38] R.O. Scattergood, D.J. Bacon, Phil. Mag. A 31 (1975) 179-198.
- [39] Wouters, Plasticity in Aluminum Alloys at Various Length Scales. University Library Groningen [Host], 2006.
- [40] H. Gleiter and E. Hornbogen, Phys. Stat. Sol. 12.1 (1965) 235-250
- [41] Young, D. J. High temperature oxidation and corrosion of metals. Elsevier (2008).
- [42] E. W. Hart, Acta Met. Metall. 5 (1957) 597.
- [43] W. W. Smeltzer, R. R. Haering, J. S. Kirkaldy, Acta Metall. 9 (1961) 880.
- [44] Kaur, W. Gust, Fundamentals of Grain and Interphase Boundary Diffusion, Ziegler Press, Stuttgart, 1989.
- [45] D. Caplan, M.J. Graham, M. Cohen, J. Electrochem, J. Electrochem. Soc. 119 (1972) 1205-1215.
- [46] J. M. Perrow, W. W. Smeltzer, J. D. Embury, Acta Met. 16 (1968) 1209-1218.
- [47] L. B. Pfeil, U. K. Patent No. 459848, 1937.
- [48] K. P. R. Reddy, J. L. Smialek and A. R. Cooper, Oxid. Met. 17 (1982) 429-449.
- [49] W. J. Quadakkers, H. Holzbrecher, K. G. Brief, H. Beske, Oxid. Met. 32 (1989) 67-88.
- [50] B. A. Pint, J. R. Martin, L. W. Hobbs, Oxid. Met. 39 (1993) 167-195.
- [51] R. Prescott, D. F. Mitchell, M. J. Graham, J. Doychak, Corr. Sci. 37 (1995) 1341-1364.
- [52] R. A. Versaci, D. Clemens, W. J. Quadakkers, R. Hussey, Solid State Ion. 59 (1993) 235-242.
- [53] S. Chevalier, Mater. Corros. 65 (2014) 109.
- [54] F. A. Golightly, F. H. Stott, G. C. Wood, Oxid. Met. 10 (1976) 163-187.
- [55] B. A. Pint, Oxid. Met. 45 (1996) 1-37.
- [56] B. A. Pint, A. J. Garratt-Reed, L. W. Hobbs, Mater. High Temp. 13 (1995) 3-16.
- [57] E. Schumann, J. C. Yang, M. J. Graham, M. Rühle, Mater. Corr. 47 (1996) 631.
- [58] K. Y. Kim, S. H. Kim, K. W. Kwon, I. H. Kim, Oxid. Met. 41 (1994) 179-201.

- [59] P. Y. Hou, J. Stringer, *Oxid. Met.* 38 (1992) 323-345.
- [60] P. Choquet, R. Mevrel, *Mater. Sci. Eng. A* 120 (1989) 153-159.
- [61] P. Y. Hou, *Oxid. Met.* 52 (1999) 337-351.
- [62] D.B. Williams and C.B. Carter. *Transmission Electron Microscopy-A Textbook for Materials Science, by Microscopy and Microanalysis*, 5(6), 452-453.
- [63] S. Mrowec and T. Weber, Published for NBS and NFS by Foreign Scientific Technical and Economic Information, Warsaw, Poland. (1978) 447.
- [64] S. Ukai, N. Oono, S. Ohtsuka, T. Kaito, K. Sakamoto, T. Torimaru, A. Kimura, S. Hayashi, Development of FeCrAl-ODS steels for ATF cladding, in: *Proc. LightWater Reactor (LWR) Fuel Performance Meeting (TOP FUEL)* 2016.
- [65] S. Ukai, N. Oono, K. Sakamoto, T. Torimaru, T. Kaito, A. Kimura, S. Hayashi, Development of FeCrAl-ODS steels claddings for accident tolerant fuel of light water reactors. *Proc. of ICAPP 2017, Fukui and Kyoto (Japan)*, April 24-28 (2017).
- [66] V. de Castro, T. Leguey, M.A. Monge, A. Muñoz, R. Pareja, D.R. Amador, J.M. Torralba, M. Victoria, *J. Nucl. Mater.* 322 (2003) 228-234.
- [67] V. de Castro, T. Leguey, A. Muñoz, M. A. Monge, R. Pareja, E. A. Marquis, S. Lozano-Perez, M. L. Jenkins, *J. Nucl. Mater.* 368 (2009) 449-452.
- [68] P. Olsson, I. A. Abrikosov, L. Vitos, J. Wallenius, *J. Nucl. Mater.* 321 (2003) 84-90.
- [69] G. Bonny, D. Terentyev, L. Malerba, *Scr. Mater.* 59 (2008) 1193-1196.
- [70] W. Xiong, M. Selleby, Q. Chen, J. Odqvist, Y. Du, *Crit. Rev. Solid State* 35 (2010) 125-152.
- [71] M. Klimiankou, R. Lindau, A. Möslang, J. Schröde, *Powder Metall.* 48 (3) (2005) 277-287.
- [72] C. S. Smith. *Trans. AIME.* 175 (1948) 15-51.
- [73] T. Nishizawa, I. Ohnuma, K. Ishida, *Mater. Trans. JIM.* 38 (1997) 950-956.
- [74] J. W. Martion and R. D. Doherty. *Stability of microstructure in metallic systems.* 173, 1976, Cambridge, Cambridge University Press.
- [75] H. Je, A. Kimura, *Corros. Sci.* 78 (2014) 193-199.
- [76] J. Isselin, R. Kasada, A. Kimura, *Corros. Sci.* 52 (2010) 3266-3270
- [77] J.H. Lee, R. Kasada, A. Kimura, T. Okuda, M. Inoue, S. Ukai, S. Ohnuki,

- T.Fujisawa, F. Abe, J. Nucl. Mater. 417 (2011) 1225-1228.
- [78] H.S. Cho, A. Kimura, S. Ukai, M. Fujiwara, J. Nucl.Mater. 329–333 (2004) 387
- [79] D. P. Whittle, J. Stringer, Philos. Trans. R. Soc. Lond. 295 (1980) 309-329.
- [80] B.A. Pint, A.J. Garratt-Reed and L. W. Hobbs, Mater. High Temp. 13 (1995) 3-16.
- [81] D. Naumenko, B. Gleeson, E. Wessel, L. Singheiser, W. J.Quadackers, Metall. Mater. Trans. A 38 (2007) 2974-2983.
- [82] M. Yamamoto, S. Ukai, S. Hayashi, T. Kaito, S. Ohtsuka, J. Nucl. Mater. 417 (2011) 237-240.
- [83] S. Ukai, S. Ohtsuka, T. Kaito, H. Sakasegawa, N. Chikata and S. Hayashi, Mater. Sci. Eng. A 510 (2009) 115-120.
- [84] S. Ukai, T. Okuda, M. Fujiwara, T. Kobayashi, S. Mizuta, H. Nakashima, J. Nucl. Sci. Technol. 39 (2002) 872-879.
- [85] J. Stringer, Mater. Sci. Eng. A 120 (1989) 129-137.
- [86] R. Prescott and M. J. Graham, Oxid. Met. 38 (1992) 233-254.
- [87] B. A. Pint, J. R. Martin, and L. W. Hobbs, Solid State Ion. 78 (1995) 99-107.
- [88] G. C. Rybicki and J. L. Smialek, Oxid. Met. 31 (1989) 275-304.
- [89] B. Gleeson, W. Wang, S. Hayashi and D. Sordellet, Mater. Sci. Forum 461 (2004) 213-222.
- [90] S. Hayashi, B. Gleeson, Oxid. Met. 71 (2009) 5.
- [91] E. Schumann, J. C. Yang, M. Ruhle and M. J. Graham, Oxid. Met. 46 (1996) 37-49.
- [92] K. Przbylski, A. J. Garratt-Reed, B. A. Pint, E. P. Katz, and G. J. Yurek, J. Electrochem. Soc. 134 (1987) 3207-3208.
- [93] W. J. Quadackers, Mater. Corros. 41 (1990) 659-668.
- [94] Z. Liu, W. Gao, Y. He, Oxid. Met. 53 (2000) 341-350.
- [95] S. Hayashi and T. Maeda, Oxid. Met. 93 (2020) 573-586.
- [96] S. Zhang, S. Ukai, T. Nishikawa, S. M. S. Aghamiri, N. Oono, S. Hayashi, J. Alloys Compd. 797 (2019) 390-398.
- [97] Z. G. Zhang, F. Gesmundo, P. Y. Hou and Y. Niu, Corros. Sci. 48 (2006) 741-765.
- [98] F.H. Stott, G. C. Wood, and J. Stringer. Oxid. Met. 44 (1995) 113-145.
- [99] T. Liu, L. Wang, C. Wang and H. Shen, Corros. Sci. 104 (2016) 17-25.

- [100] S. Ukai, N. Oono, K. Sakamoto, T. Torimaru, T. Kaito, A. Kimura, S. Hayashi, Proceedings of 2017 international congress on advances in nuclear power plants (ICAPP2017), (p. 2573). Japan
- [101] W.J. Quadakkers, D. Naumenko, E. Wessel, V. Kochubey, L. Singheiser, *Oxid. Met.* 61 (2004) 17-37.
- [102] D.J. Young, *High temperature oxidation and corrosion of metals*. Elsevier (2008).
- [103] B.A. Pint, J. Leibowitz, J.H. De Van, *Oxid. Met.* 51 (1999) 181.
- [104] A. M. Huntz, G. B. Abderrazik, G. Moulin, E. W. A. Young and J. H. W. De Wit, *Appl. Surf. Sci.* 28 (1987) 345-366.
- [105] E. W. Hart, *Acta Metall.* 5 (1957) 597-605.
- [106] W. W. Smeltzer, R. R. Haering, J. S. Kirkaldy, *Acta Metall.* 9 (1961) 880-885.
- [107] R. E. Mistler and R. L. Coble, *J. Am. Ceram. Soc.* 54 (1971) 60-61.
- [108] D. Clemens, K. Bongartz, W. J. Quadakkers, H. Nickel, H. Holzbrecher and J. - S. Becker. *Fresenius J. Anal. Chem.* 353 (1995) 267-270.
- [109] S. Hayashi, Y. Takada, S. Yoneda and S. Ukai, *Oxid. Met.* 86 (2016) 151-164.
- [110] S. Yoneda, S. Hayashi, I. Saeki and S. Ukai, *Oxid. Met.* 86 (2016) 357-370.
- [111] C. Vailhé & D. Farkas, *J. Mater. Res.* 12 (1997) 2559-2570.
- [112] P. Haas, F. Tran, P. Blaha, *Phys. Rev. B* 79 (2009) 085104.
- [113] R.O. Scattergood, D.J. Bacon, *Phil. Mag. A* 31 (1975) 179-198.
- [114] K.G. Field, M.A. Snead, Y. Yamamoto, K.A. Terrani, *Handbook on the Material Properties of FeCrAl Alloys for Nuclear Power Production Applications*, ORNL/TM-2017/186.
- [115] D. Tabor, *The hardness of metals*, Oxford university press, 1951.
- [116] H. Y. Yasuda, Y. Odawara, K. Soma, T. Yoshimoto, K. Cho, *Intermetallics* 91 (2017) 140-149.
- [117] R. C. Reed, *The superalloys Fundamentals and Applications*, Cambridge University Press, 2006.
- [118] A. J. Ardell, *Metall. Trans. A* 16 (1985) 2131-2165.
- [119] Y. Yamamoto, B. A. Pint, K. A. Terrani, K. G. Field, Y. Yang, L. L. Snead, J. Nucl. Mater. 467 (2015) 703-716.

- [120] C. P. Massey, S. N. Dryepondt, P. D. Edmondson, K. A. Terrani, S. J. Zinkle, Nucl. Mater. 512 (2018) 227-238.
- [121] Y. Zhang, S. C. Tonn, M. A. Crimp, Mat. Res. Soc. Symp. Proc. 288 (1992) 379-384.
- [122] S. Takeuchi, Jpn. J. Appl. Phys. 8 (1969) 1205-1210.
- [123] G.Y. Chin, Jpn. J. Appl. Phys. 9 (1970) 1260-1262.
- [124] K.F. Hale, M.H. Brown, Proc. Roy. Soc. A 310 (1969) 479-491.
- [125] R.W. Kozar, A. Suzuki, W.W. Milligan, J.J. Schirra, M.F. Savage, T.M. Pollock, Metall. Mater. Trans. A 40 (2009) 1588-1603.
- [126] M. P. Brady, Y. Yamamoto, M. L. Santella, P. J. Maziasz, B. A. Pint, C. T. Liu, Z. P. Lu and H. Bei, JOM 60 (2008) 12-18.
- [127] Y. Yamamoto, M. P. Brady, Z. P. Lu, P. J. Maziasz, C. T. Liu, B.A. Pint, K. L. More, H. M. Meyer, E. A. Payzant, Science 316.5823 (2007) 433-436.
- [128] S. Mrowec and T. Weber, Published for NBS and NFS by Foreign Scientific Technical and Economic Information, Warsaw, Poland. (1978) 447.
- [129] Y. Kitajima, S. Hayashi, T. Nishimoto, T. Narita, S. Ukai, Oxid. Met. 75(1-2) (2011) 41-56.
- [130] S. Yoneda, S. Hayashi and S. Ukai, Oxid. Met. 89 (2018) 81-97.
- [131] Y. Shizukawa, S. Ukai, N. Oono, S. Hayashi, S. Ohtsuka, T. Kaito, T. Torimaru, A. Kimura, Proceeding on Advanced High-Temperature Materials Technology for Sustainable and Reliable Power Engineering (123HiMAT-2015) 29, June-3 July, 2015, Sapporo, Japan.
- [132] S. Ukai, N. Oono, S. Ohtsuka, T. Kaito, K. Sakamoto, T. Torimaru, A. Kimura, and S. Hayashi, The Ninth Pacific Rim International Conference on Advanced Materials and Processing (PRICM9), Kyoto Japan, Aug. 1-5, 2016.
- [133] Y. Yano a, T. Tanno, H. Oka, S. Ohtsuka, T. Inoue, S. Kato, T. Furukawa, T. Uwaba, T. Kaito, S. Ukai, N. Oono, A. Kimura, S. Hayashi, T. Torimaru, J. Nucl. Mater. 487 (2017) 229-237.
- [134] S. Ukai, N. Oono, S. Ohtsuka, T. Kaito, K. Sakamoto, T. Torimaru, A. Kimura, S. Hayashi, Proceeding of LWR Fuel with Enhanced Safety and Performance, TOPFUEL2016, September 13, 2016, Boise, Idaho, USA.
- [135] S. Ukai, N. Oono, K. Sakamoto, T. Torimaru, T. Kaito, A. Kimura and S.

- Hayashi, Proceedings of ICAPP, April 24-28, 2017, Fukui and Kyoto (Japan).
- [136] Nuclear Data by Japan Atomic Energy Agency, https://www.ndc.jaea.go.jp/NuC/index_J.html.
- [137] M. Yamamoto, S. Ukai, S. Hayashi, T. Kaito, S. Ohtsuka., J. Nucl. Mater. 417 (2011) 237-240.
- [138] G. H. Eicherman and F. C. Hull, Trans. Am. Soc. Met. 45 (1953) 77
- [139] H. Schumann, Archiv für das Eisenhüttenwesen, 40 (1963) 1027-1037.
- [140] S. Mrowec and T. Weber, Gas corrosion of Metals, US Department of Commerce, National Technical Information Service (1978) p. 447.